Layer-by-Layer Assembly in Confined Geometries

by

JONATHAN PAUL DEROCHER

Bachelor of Chemical Engineering
Department of Chemical Engineering and Materials Science
University of Minnesota, Minneapolis, MN, 2005

Master of Science in Chemical Engineering Practice
Department of Chemical Engineering
Massachusetts Institute of Technology, Cambridge, MA, 2008

Submitted to the Department of Chemical Engineering
in partial fulfillment of the requirements for the degree of

DOCTOR OF PHILOSPHY IN CHEMICAL ENGINEERING
at the
MASSACHUSETTS INSTITUTE OF TECHNOLOGY

September, 2011

Signature of Author: ______________

Department of Chemical Engineering
August 17, 2011

Certified by: ____________________________

Robert E. Cohen
St. Laurent Professor of Chemical Engineering
Thesis Supervisor

Certified by: ____________________________

Michael F. Rubner
TDK Professor of Materials Science and Engineering
Thesis Supervisor

Accepted by: ____________________________

William M. Deen
Carbon P. Dubbs Professor of Chemical Engineering
Chairman, Committee for Graduate Students

Layer-by-Layer Assembly in Confined Geometries

by

Jonathan Paul DeRocher

Submitted to the Department of Chemical Engineering
on August 17, 2011 in Partial Fulfillment of the
Requirements for the Degree of Doctor of Philosophy in
Chemical Engineering

ABSTRACT

The fundamental nature of layer-by-layer (LbL) assembly in confined geometries was investigated for a number of different chemical systems. The first part of this thesis concerns the modification of microfluidic and nanofluidic devices which hold great potential as a platform for manipulation and analysis of small sample volumes. The high throughput and high surface area possible with these devices suggests applications in biomolecule or chemical detection, selective separation, and heterogeneous catalysis. To realize some of this potential, the surfaces of these devices can be modified to impart functionality to the device. Polyelectrolyte multilayers can be used to impart a broad array of novel functionalities to a surface including stimuli-responsiveness, reversible switching of the gap thickness, manipulation of the sign and/or the density of the surface charge, chemical functionality and wettability of a surface.

Polymer/polymer, polymer/nanoparticle, and nanoparticle/nanoparticle multilayers have all been deposited in confined channels. In all cases, conformal uniform multilayers were observed throughout the high aspect ratio channel. LbL assembly within submicron channels does, however, reveal a number of interesting departures from what is seen for LbL growth on infinite planar surfaces and we explain this effect by surface charge-induced depletion of the adsorbing species in the confined channel at each stage of the assembly process. At sufficiently low ionic strengths, this exclusion prevents further deposition on confined surfaces while adjacent unconfined surfaces continue to be coated. Nanoparticle/nanoparticle deposition results in systematic bridging of the nanochannels with a nanoporous multilayer.

This fundamental knowledge was applied to the systematic narrowing of nanochannels embedded in a hybrid micro/nanofluidic device using LbL assembly of polyelectrolytes. The narrowing of these channels was monitored using conductance experiments and showed that the channel thickness could be controlled down to 11 nm. Understanding of exclusion was used to modify track etched polycarbonate membranes in an attempt to build composite membranes which exhibited high salt rejection and high water permeance. These membranes were compared with theoretical models and with commercially available reverse osmosis membranes.

Thesis Supervisors: Robert E. Cohen, St. Laurent Professor of Chemical Engineering
Michael F. Rubner, TDK Professor of Materials Science and Engineering

Acknowledgements

So many people have helped me during my years at MIT and throughout my academic career that I could not possibly properly acknowledge all of them. I would like first of all to thank my advisors, Professor Cohen and Professor Rubner. I have truly enjoyed being co-advised by them and have benefited greatly both professionally and personally from their contrasting styles and perspectives. Professor Cohen has been a constant source of encouragement and support as well as great questions and novel ideas. I also had the privilege of serving as a teaching assistant in a number of his classes and learned a lot about being an educator through these experiences and his example. Professor Rubner has also been very encouraging, especially when things were not going well and an encyclopedic resource for all things LbL. I have learned a lot about making good, accessible presentations from watching him teach undergraduates and give talks designed for non-specialists. Both were very enthusiastic about my work and kept me energized through failed experiments and disappointing results. I feel privileged to have worked with not only two of the best scientists, but also two of the best advisors at MIT.

Professor Patrick Doyle and Professor Jongyoon Han made up the rest of my thesis committee and made very helpful suggestions during our meetings. Both provided much-needed expertise in microfluidics and Professor Han in particular provided many of the substrates we used in this work.

Dr. Pan Mao from the Han Lab and Dr. Jun Young Kim, a postdoctoral researcher from Samsung, were very helpful to me in carrying out this work; I quite literally could not have completed this thesis without them. Pan fabricated the various nanofluidic devices that we used as substrates and showed me how to prepare the devices for use and characterize them using conductance measurements. Jun Young was a meticulous researcher who took some interesting polymer/nanoparticle preliminary results and turned them into a complete and very interesting story.

I would also like to thank Professor Ed Cussler, my undergraduate research advisor at the University of Minnesota. He gave me the opportunity to work in his lab for essentially my entire undergraduate career and really took a personal interest in me. He encouraged me to apply for the Gates Scholarship which led to an unforgettable year at Cambridge University and gave me the confidence that I could succeed at the top graduate schools in the country. His inspiring teaching and accessible presentation style have also greatly influenced me.

One of the greatest benefits of being in the Cohen and Rubner groups was the many talented researchers with whom I interacted daily. I would like to thank Prof. Daeyeon Lee, Prof. Adam Nolte, Dr. Ryan Bennett, Dr. Ben Wang, Dr. Sharon Soong, Dr. Andy Miller, Dr. Jenny Lichter, Dr. Ayse Asatekin, Dr. Al Swiston, Dr. Nathan Lovell, Mr. Erik Williamson, Dr. Zekeriyya Gemici, Dr. Gary Chia, Dr. Wui Siew Tan, Mr. Shreerang Chhatre, Mr. Hyomin Lee, Mr. Siddharth Srinivasan, Mr. Jonathan Gilbert, Mr. Justin Kleingartner, Mr. Ji Sam Wong, Dr. Grinia Nogueira, Prof. Anish Tuteja, Dr. Hiroomi Shimomura, Dr. Nurxat Nuraje, Dr. Pinar Kurt, Dr. Koushik Mukherjee, and Mr. Girma Endale. In particular, I am indebted to Daeyeon Lee for carrying out the preliminary experiments which led to this thesis and to Zekeriyya Gemici for showing me the ropes when I first joined the lab. Andy Miller also was a great resource during the early part of my studies. Gary Chia, Grinia Nogueira, and Wui Siew Tan were very helpful to me in the work on membrane modification and have become good friends. Erik Williamson was a very caring coworker who would drop everything to help others and also happened to be a great addition to our intramural hockey team. Shreerang Chhatre, who had the misfortune of sitting next to me, was always willing to listen and always had helpful suggestions and a fresh perspective on matters both scientific and otherwise. He was always happy to go for lunch or for a cup of tea and helped to make the lab a very pleasant place to be. I would also like to thank Adam Meuler, a postdoctoral researcher and fellow Minnesota alumnus, who was always friendly and was particularly helpful in maintaining the lab.

I am also thankful for the many friends and classmates who made life at MIT so much more enjoyable and interesting. I have particularly enjoyed the many nights out, ski trips, movies, trivia nights, dim sum brunches, and sporting events we enjoyed together. I have also greatly enjoyed participating in ChemE intramural sports at MIT. From our first year soccer team for which I displayed much more enthusiasm than talent to our hockey teams which I loved playing on and eventually captaining to our championship-winning summer softball and octathon teams, the camaraderie and enthusiasm of my teammates has made these games a welcome respite from research. I particularly want to thank my roommate, Arvind Prabhakar, who has been a great friend over the past five years.

I would like to acknowledge Suzanne Maguire, Mary Wesolowski, Katie Lewis, Christine Preston, Carrie Casado, and Andre Puca for administrative support and for making sure that all the deadlines were met and all the correct forms were filled out. I would also like to thank Yong Zhang from the Center for Materials Science and Engineering SEM facility who helped me wrestle decent images out of the high resolution SEM. Both the CMSE and the Institute for Soldier Nanotechnologies allowed me to used characterization equipment which was indispensable in obtaining the results I needed. Finally I would like to thank my funding sources, the National Science Foundation Graduate Research Fellowship Program and the CMSE.

I would especially like to thank Yi Du for her love and support over the past few years. She has been incredibly patient and understanding and has always treated me far better than I deserve. I would not have made it to this point without her optimism and timely advice.

Last, but certainly not least, I would like to thank my family for all the love and support they have given me throughout my life and especially over the last five years. My parents, Paul and Linda DeRocher have been an incredible example to me and have encouraged me to excel without placing undue pressure on me. My grandparents, Jack and Lillian Boman and Bob and Phyllis DeRocher have also been very supportive and have always shown interest in my work. I thank my siblings, Mary, Mark, and Karen, for their support and for putting up with me for so many years.

Table of Contents

List of Figures

List of Tables

Chapter 1 Introduction

1.1 Motivation and Background

One of the most important concerns when developing products of almost any sort is managing the way in which they interact with their environment. Consequently, tailoring the surface properties of a product is an important problem in materials science. One need only look at the dizzying array of coatings available in a local hardware store to see this fact. We buy sealants for our decks, paint for our walls, lacquer for ornamental woodwork, and wax for our cars. Common consumer items also include engineered surface coatings which enhance the value of the product. Our smartphones come with oleophobic screens which resist smudging, our pots and pans have non-stick coatings which make them easier to clean, and our computer and TV screens have anti-glare coatings that increase picture quality. These coatings add value by decoupling the bulk properties of a material and its surface properties. For example, a metal frying pan is desirable because of its high heat conductivity, but metals inherently have high surface energy values and therefore adhere relatively strongly to whatever you are frying. Teflon has a much lower surface energy and cleans easily, but has poor conductance and mechanical properties. By combining these two materials, one can optimize both the bulk and surface properties to fit the desired application.

Past and current work in the Cohen and Rubner groups is largely focused on the engineering of surfaces to impart desirable properties. In particular, thin film coatings which exhibit antireflection,[1-4] antibacterial,[1-4] cytophilic,[5-7] superhydrophobic,[8-10] oleophobic,[11-16] superhydrophilic,[17-19] antifogging,[18,20] pH-responsive,[21-24] temperature-responsive,[25] magnetic,[2,26] and structural color[19,27,28] properties have been fabricated and characterized. This wide variety of surface functionalities serves as an excellent toolbox which we can use to design appropriate coatings for new applications. Sensibly, these films have largely been applied to planar macroscopic substrates or on surfaces where the features are much larger than the entities which make up the coatings themselves. Assembling multifunctional coatings on microscopic surfaces with intricate topological features and large surface area per volume will open up many new and exciting applications for this technology.

The advent of the computer age, which created the need for rapid and cheap production of smaller and smaller transistors, has led to very powerful modern microfabrication techniques. These techniques allow for the construction of very well-defined features with length scales on the order of a few microns over hundreds of square centimeters. This has inspired interest in fluid flow in channels fabricated using these methods, spawning the field of microfluidics. Researchers have taken advantage of the unique behavior of fluids at such small length scales along with high surface area to volume ratios to make a wide variety of novel devices. Of particular interest are so-called “lab on a chip” devices which are designed to allow a range of diagnostic tests to be accomplished in parallel within a single device using microliter scale sample volumes. To make this possible, one has to perform reactions and achieve very sensitive quantitative detection of analytes within these small channels. Microfluidic and nanofluidic channels are well suited to these tasks due to their high surface area to volume ratios and correspondingly short diffusion lengths, but since the materials suitable for microfluidic device fabrication are fairly limited, coatings must be developed to obtain the desired surface properties. This thesis focuses on the deposition of coatings within confined geometries, allowing us to extend our surface modification processes to this new class of substrates.

In this chapter we will focus on the behavior of polyelectrolytes in solution and as they adsorb onto a solid surface and how both of these phenomena are dependent on the pH and ionic strength of the solution. We will then introduce layer-by-layer (LbL) assembly and discuss in detail how this general processing technique can be used to fabricate functional coatings from a wide range of starting materials.

1.2 Adsorption of Polyelectrolytes from Aqueous Solution

Polyelectrolytes are a class of polymers whose constituent monomers include a charged moiety. These charged groups can either be stable as in the case of a sulfonate ion or labile like a carboxylic acid group. Polymers with fully dissociated ions are termed strong polyelectrolytes, while those where partial ionization is possible are known as weak polyelectrolytes. As the following sections will discuss in detail, the presence of charged groups along the polymer backbone has profound consequences on the conformation of a polymer chain and its adsorption behavior.

1.2.1 Polyelectrolyte Basics and the Effect of Molecular Weight

The configuration which a neutral polymer chain assumes in solution is a result of the balancing of enthalpic and entropic driving forces. Consider the simplest polymer, polyethylene. Since each carbon is tetrahedral, the projection along the C-C bond shows that each carbon has three bonds radiating from it at 120° from each other: two to hydrogen and one to carbon. These three bonds on the two neighboring carbons can either be eclipsed or staggered since the C-C bond rotates freely. Clearly, the staggered conformation is lower in energy due to steric hindrance between opposing groups in the eclipsed state. Furthermore, since the backbone runs through the carbon atoms, the staggered conformation with the lowest enthalpy is the one with carbons on the opposite side of the C-C bond *i.e.* an all-trans or fully extended configuration. This is only half the story though; clearly there is only one all-trans configuration and it therefore has extremely low entropy. Entropy favors a chain defined by a random walk, otherwise known as a freely jointed or Gaussian chain, which has a much more compact conformation.

The parameter we will use to represent the chain configuration is the root mean square (RMS) end-to-end distance $\sqrt{\bar{r}^2}$ which gives us a rough idea of the size of the polymer coil. This parameter is conceptually convenient, and is easily converted to the experimentally accessible radius of gyration by dividing by a factor of $\sqrt{6}$. For a fully extended chain the RMS end-to-end distance is simply:

$$\sqrt{\bar{r}^2} = ln_b \sin\frac{\theta}{2} \tag{1.1}$$

where l is the length of each bond, n_b is the number of bonds, and θ is the bond angle. For a freely jointed chain, the analogous expression is:

$$\sqrt{\bar{r}^2} = l\sqrt{n_b} \tag{1.2}$$

The expression for a real chain falls between these two extremes and is given by:[29]

$$\sqrt{\bar{r}^2} = \alpha l\sqrt{C_\infty n_b} \tag{1.3}$$

where α is the coil expansion factor and C_∞ is the characteristic ratio. The coil expansion factor accounts for long-range intramolecular interactions and interactions between the polymer chain and surrounding solvent molecules. The characteristic ratio on the other hand accounts for short-range interactions such as restrictions on the allowed bond angles and rotational angles. Most polymers have characteristic ratios between five and ten; for polyethylene, this quantity is around seven. It is clear that if we remove the bond angle and long-range interaction constraints, both of these quantities are equal to one and our formula collapses to Equation (1.2) for a freely jointed chain. We can also see that the size of the polymer coil scales as the square root of molecular weight.

For polyelectrolytes, the situation is more complex. Electrostatic interactions between charged groups along the chain and with the surrounding solvent contribute to coil expansion through the α term in Equation (1.3). One way to visualize this is to imagine the ionizable groups within the polymer chain as they are dissolved in a solvent. These groups will ionize, losing their counterion and therefore the chain will have uncompensated charges of the same sign throughout its backbone. It makes intuitive sense that these fixed charges will repel each other and will tend to expand the coil significantly. An equivalent way of thinking about this is to think of the polymer coil as a globular gel with a membrane surrounding it.[29] Since the charged groups on the polymer chain are fixed, counterions cannot diffuse away due to electroneutrality requirements and the hypothetical membrane therefore acts like a semipermeable membrane. If this ion-rich gel is exposed to pure solvent, the solvent will pass through the hypothetical membrane and swell the polymer coil to lower the concentration of ionic species within it. These equivalent constructs both result in the same conclusion, namely that the coil expands significantly when fixed charges are added to the polymer backbone. A schematic of these two conceptualizations is given in Figure 1-1.

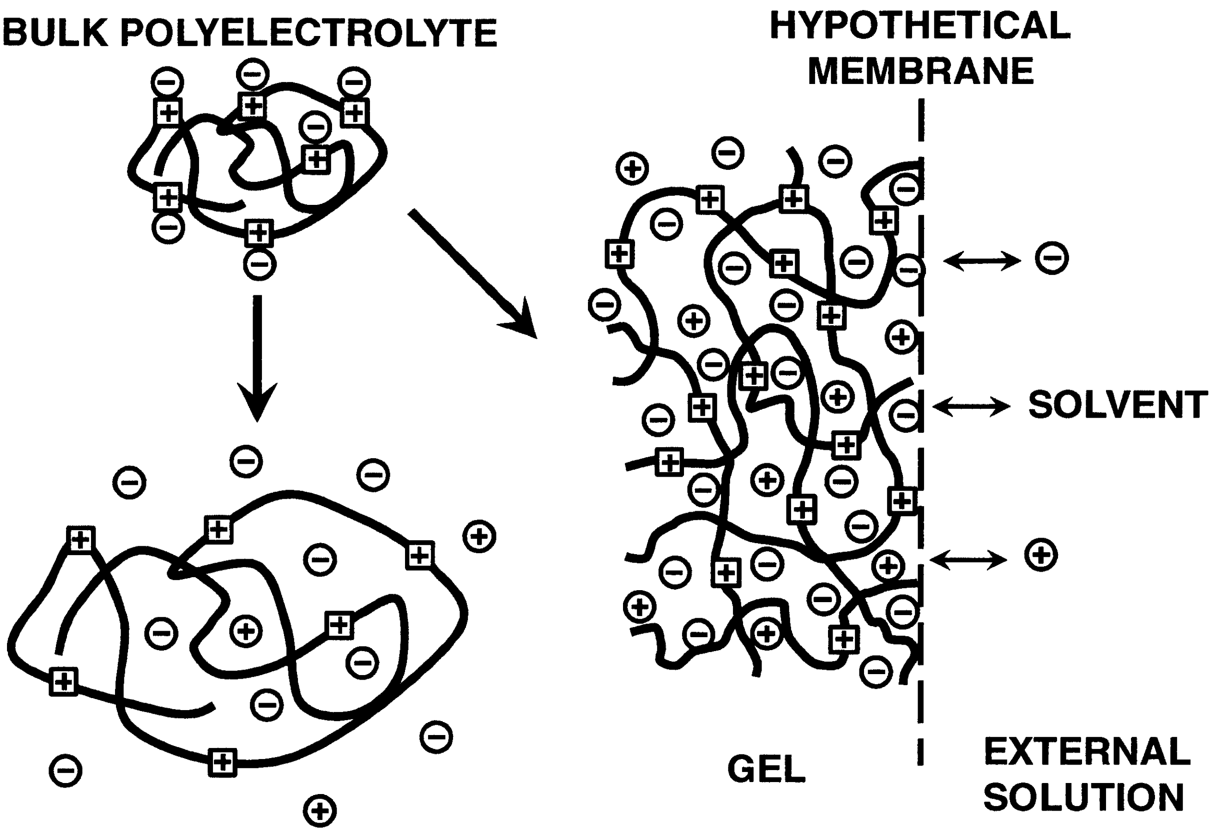

Figure 1-1 Schematic illustration of the swelling of a polyelectrolyte coil in solution. Squares represent fixed charges and circles represent mobile ions. At the lower left we see that uncompensated fixed moieties repel each other, expanding the coil. On the right hand side we see a polyelectrolyte gel into which solvent diffuses to lower the ionic strength within the gel, swelling the polymer coils. Adapted from Flory.[29]

The presence of charged groups also has profound effects on the way in which polyelectrolytes adsorb onto a solid surface. Since polymer chains are flexible and can sample a range of conformations, they tend to adsorb to surfaces much more strongly than a small molecule or a rigid colloidal particle would. One can imagine that as a charged group within the polyelectrolyte pairs with a complementary charge on the surface, the rest of the polymer molecule is held in close proximity to the surface and as the coil samples the surface nearby, other charged groups will find charged sites on the surface to bind with. Although each particular binding event might be prone to desorption, the connectivity of the polymer and the number of binding sites which it occupies discourage desorption of the entire molecule. In contrast, a small molecule normally has one or at best a few binding sites and therefore desorbs more easily. A rigid, charged colloidal particle on the other hand has many binding sites, but because it cannot deform it can only make contact with the surface at one point and therefore desorbs much more easily.

The conformation which a polyelectrolyte takes up in solution will also determine to some extent how it adsorbs onto a surface. A highly-charged, expanded coil will explore a relatively large area of the surface, binding in many places and taking up a flat, spread out conformation. A coil which has lower charge density or takes up a more compact conformation will sample less of the surface surrounding the initial binding site and therefore have fewer bonds to the surface and a more globular conformation. This phenomenon leads to the somewhat counterintuitive result that expanded coils which have greater mean square end-to-end distance actually produce a thinner adsorbed layer than coils with a more compact conformation. This also sheds light on the effect of molecular weight on the thickness of the adsorbed layer. For expanded coils which can sample large areas of the surface, the molecular weight has little effect on the adsorbed layer thickness since a larger coil will simply sample a greater area, but will still exhibit a relatively flat conformation. On the other hand, the adsorption of compact coils with differing molecular weights shows that the thickness of the adsorbed layer does depend on molecular weight, again because the coil retains its globular conformation after adsorption.[30]

1.2.2 The Effect of pH

As mentioned before, a number of important polyelectrolytes contain weak acid or base functional groups whose ionization is pH-dependent. As a result, the charge density along these polyelectrolyte chains can be manipulated simply by changing the pH of the solution in which they are dissolved. Since the charge density directly affects the conformation of a polyelectrolyte molecule in solution and the way in which it adsorbs onto a surface, this gives us an important lever by which we can control the structure of an adsorbed polymer layer.

Most weak polyelectrolytes are either polycarboxylic acids or polyamines. Just like its corresponding monomer, a polycarboxylic acid is largely protonated at low pH (*i.e.* acidic conditions). As the pH rises, individual acid groups are steadily deprotonated until the chain is essentially fully ionized at sufficiently high pH. The pH at which exactly half of the carboxylic acid groups are protonated is known as the pK_a of the polyelectrolyte. Obviously for a polyamine, the situation is reversed. At low pH, the amine groups are fully protonated and thus fully ionized. As the pH rises, the chain is deprotonated and at sufficiently high pH is essentially neutral. This transition has been studied in great detail for two of the most common polyelectrolytes: poly(acrylic acid) (PAA) and poly(allylamine hydrochloride) (PAH). Choi and Rubner measured the ionization states of these two polyelectrolytes using Fourier transform infrared (FTIR) spectroscopy of dried films and compared them with titration data obtained by others.[31] As depicted in Figure 1-2, PAA changes from neutral to negatively charged as the pH rises from 2.0 to 10.0 with a pK_a of about 6.5 and PAH changes from neutral to positively charged as the pH rises from 2.0 to 12.0 with a pK_a of about 8.8.

It is clear from these figures that one can continuously tune the ionization of a weak polyelectrolyte chain from neutral to fully charged. Consequently, one can also tune the conformation of the polyelectrolyte chain from an essentially neutral chain which takes up a compact coil configuration to a highly charged chain whose dimensions are on the order of the contour length. To extend the discussion of the previous section, as ionization increases there are more charged groups along the polymer backbone which are therefore closer to each other and repel each other more strongly, resulting in expansion of the chain. Equivalently, one can imagine that as the ionization of the chain increases, the ionic strength within the polymer coil increases, resulting in a greater osmotic driving force across the hypothetical membrane surrounding the coil. This driving force results in diffusion of solvent into the molecule and a swelling of the chain.

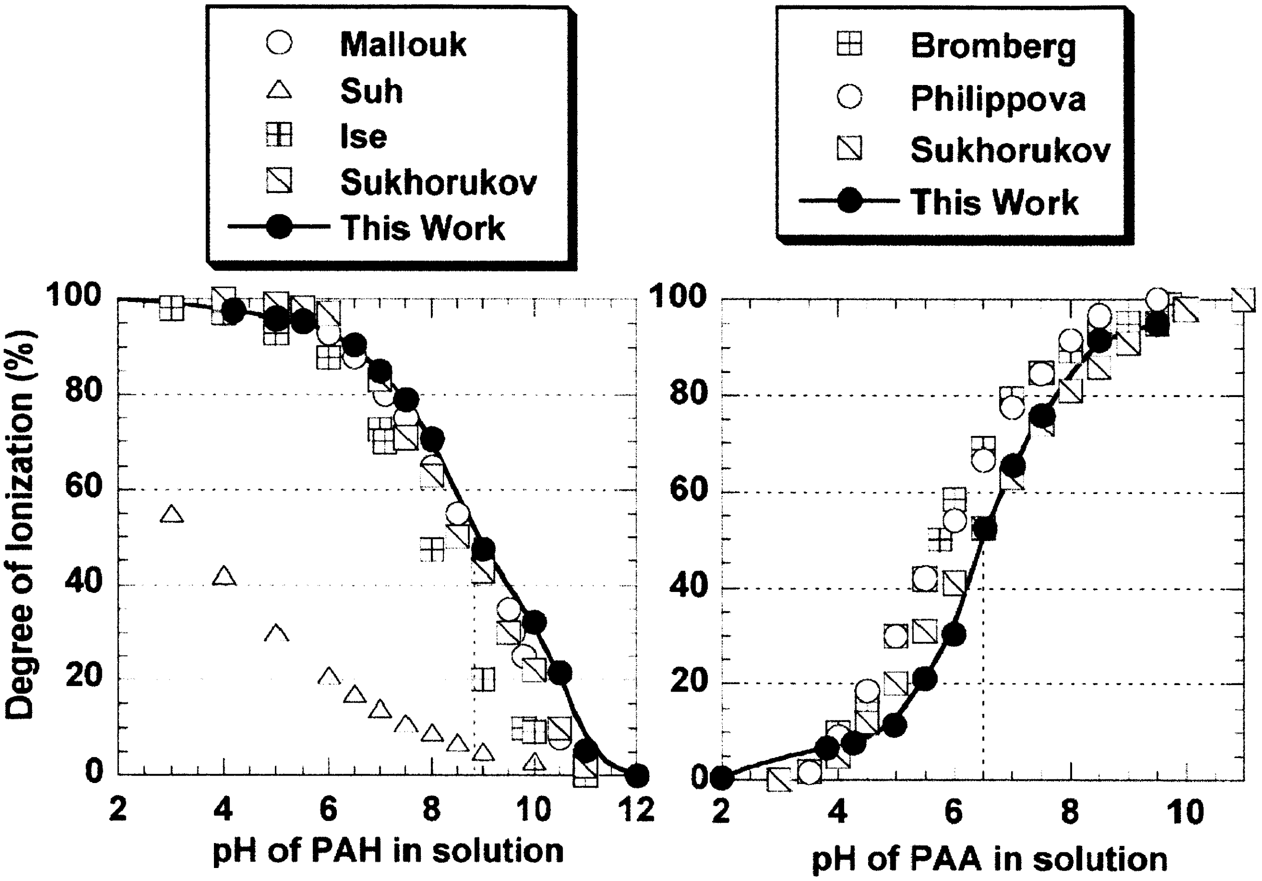

Figure 1-2 The degree of ionization of PAA and PAH in solution as a function of pH. These data were obtained via FTIR analysis and are compared with data obtained by other groups using titration. Reproduced with permission from Choi, J.; Rubner, M. F. *Macromolecules* **2004**, *38*, 116-124. Copyright 2004 American Chemical Society.[31]

As discussed above, the conformation of a polymer in solution directly affects the manner in which it adsorbs to a surface. A slightly ionized chain like PAA at pH 4.0 will take up a fairly compact configuration and will have relatively few charged groups which will bind to charged sites on the surface. As a result, this molecule will not spread out on the surface, the thickness of the adsorbed polymer layer will be dependent on molecular weight, and its adhesion will be somewhat weaker than a more highly charged molecule. On the other hand since most of its functional groups remain as carboxylic acids and not carboxylate ions, this layer is useful as a platform for further modification. The carboxylic acid groups are sensitive to changes in pH and are able to participate in reactions that would allow the attachment of other entities to the adsorbed film. If PAA is adsorbed onto a surface from a pH 9.0 solution in which it takes up a much more expanded configuration, it will spread out and bind to the surface at many points. As a result, the thickness of the adsorbed layer will be independent of molecular weight, its adhesion will be stronger, and it will have far fewer carboxylic acid groups accessible for chemical modification. Obviously, analogous arguments can be made for a polycation, such as PAH.

Strong polyelectrolytes, which often contain sulfonate or quaternary amine functional groups, are essentially fully dissociated at all pH values and do not display this strong dependence on solution pH. They therefore take up expanded coil conformations and occupy relatively large areas of the surface in flat conformations. To modify the conformations of this class of polyelectrolytes we need another lever, namely ionic strength.

1.2.3 The Effect of Ionic Strength

The ionic strength of the solution in which a polyelectrolyte is dissolved serves as another parameter which can be tuned to change its conformation in solution and on the surface. Adjusting the ionic strength does not change the charge density along the polymer chain, but instead changes the effectiveness of the repulsion due to charged groups of the same sign in close proximity. Raising the concentration of mobile ions raises the dielectric constant of the solution, screening the charged groups along the chain from each other and decreasing the distance over which they can repel each other. Essentially the distance over which two charged groups can “feel” or “see” each other is diminished as the ionic strength of the solution is increased. If we again imagine a polyelectrolyte molecule as a swellable gel with a hypothetical membrane surrounding it, we can see that as we increase the ionic strength of the external solution, the osmotic driving force across the membrane is reduced as the ion concentration outside the molecule approaches that of the charged functional groups and counterions within the molecule. As a result, less solvent must diffuse across the membrane to equilibrate the ionic strength on either side of the membrane and therefore the molecule will swell to a smaller extent. Both explanations lead to the same result, that the conformation of a polyelectrolyte becomes more compact as the ionic strength increases. Schematics of this effect and the effect of pH are shown schematically in Figure 1-3 for PAH and poly(styrene sulfonate) (PSS).

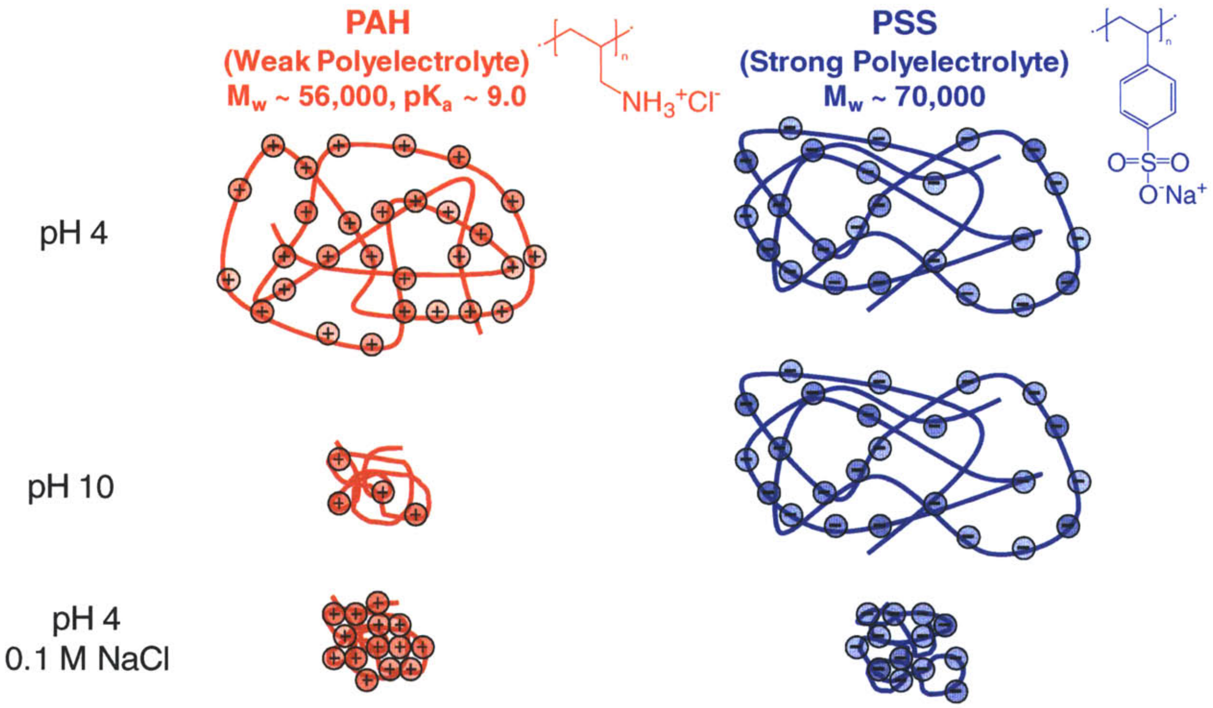

Figure 1-3 Schematic representations of the conformations of both a strong and a weak polyelectrolyte as a function of pH and ionic strength.

The ability to use both pH and ionic strength to influence the conformation of weak polyelectrolytes allows us to independently control the size of the molecule and its chemical functionality. If a highly charged, expanded conformation is required, we simply adjust the pH to obtain a relatively high degree of ionization and add no additional salt as shown for pH 4 PAH in Figure 1-3. If a compact but highly charged conformation is desired on the other hand, we can add sufficient salt to drive the molecule into a collapsed configuration as in the bottom left of Figure 1-3. If chemical functionality is desired one can simply lower the degree of ionization via pH adjustment and then decrease the polyelectrolyte coil size as desired by the addition of salt. It should be noted that these two phenomena are not entirely independent; clearly either very high or very low levels of pH by definition entail higher ionic strengths. That said, it is clear from Figure 1-2 that for PAA, degrees of ionization between 10 and 90% can be realized within a pH range of 4.5–8.5 for which the ionic strength is always less than $4 \cdot 10^{-5}$ M. The same range of ionization can be achieved within a pH 6.5–11.0 range for PAH meaning the ionic strength is no more than 10^{-3} M. In both cases, the ionic strength due to pH adjustment is relatively low. Additionally the high pH bound for PAH is a mostly uncharged, relatively compact coil so that the effect of ionic strength on conformation is muted. Thus, with only minor limitations, one can independently adjust the size and chemical nature of a polyelectrolyte molecule using careful manipulation of the solution pH and ionic strength.

1.3 Layer-by-Layer Assembly

Layer-by-layer assembly is a completely general processing technique by which materials with complimentary functionality are sequentially adsorbed onto a solid surface. Traditionally this is accomplished by taking advantage of electrostatic interactions although hydrogen bonding[32-34] and specific biological interactions such as antibody/antigen[35] and avidin/biotin[36] couplings have also been demonstrated successfully. In principle, any complimentary interaction can be used to assemble multilayers via sequential adsorption, making this method very powerful and widely applicable. The LbL technique is a type of directed assembly whereby the constituents of the film are incorporated into the growing multilayer one at a time in order to achieve the properties desired. This is in contrast to self assembly in which all the constituents of the film are present from the start and spontaneously assemble into a particular ordered structure.

LbL assembly of polyelectrolytes was popularized by the work of Gero Decher beginning in the early 1990s.[37] He described a simple process in which sequential deposition of polyanionic and polycationic species leads to charge reversal after every step and hence sustained growth of a layered film. This procedure is depicted schematically in Figure 1-4. The process starts with a substrate which has native surface charge or can be treated to induce charged sites on the surface. For the purposes of this discussion, let us assume that the initial surface charge is negative. This substrate is then dipped into a dilute polycation solution, for example PAH. The polyelectrolyte diffuses to the surface and adsorbs as described above. Since each polymer molecule has many charged groups, not all of them will associate with charged sites on the surface and therefore after most or all of the surface sites are occupied, the net charge will have switched from negative to positive. In addition to this, there will also be excess adsorption due to physisorption of polymer molecules. To remove these weakly bound polycation chains and to avoid complex formation in solution due to mixing of the polyelectrolyte solutions, the substrate is dipped into a solution of pure solvent between deposition steps.

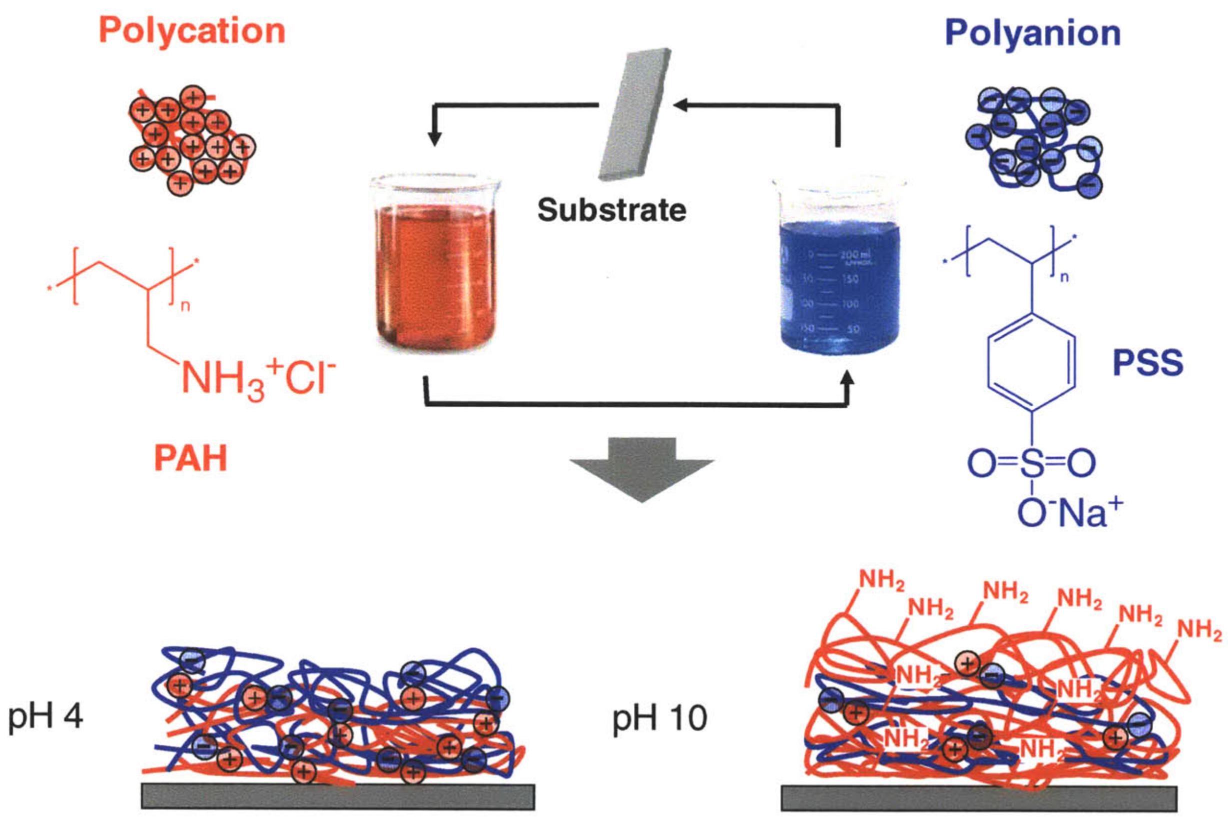

Figure 1-4 Schematic of LbL assembly of polyelectrolytes. An initially charged substrate is sequentially immersed in dilute solutions of polyelectrolyte to obtain multilayer films. Deposition of PAH and PSS at pH 4 yields a film which has many ionic cross-links while deposition of the same species at pH 10 yields a film enriched in PAH which contains many amine functional groups.

After rinsing, the substrate is then dipped into the dilute polyanion solution, PSS in Figure 1-4. The PSS molecules diffuse to the surface and their charged groups compensate the unpaired charged groups of PAH left over from the previous layer. Once again, since PSS has many charges on a single chain, not all of them will be paired and the net charge once again reverses, becoming negative. The surface is again rinsed via immersion in pure solvent to remove entrained solution and weakly adsorbed species. One cycle of this process in which a positively charged layer and a negatively charged layer are adsorbed is known as one bilayer. Since the surface charge continues to reverse after every deposition step, this process can be carried out indefinitely to obtain a film which is as thick as required for the desired application. The use of the term bilayer is not to insinuate that the polymers form discrete strata, but instead a description of the process by which they are formed. Indeed studies have shown that oppositely charged polyelectrolytes copiously interpenetrate such that two consecutive deuterated polyanion layers (with a polycation layer between) cannot be resolved by neutron reflectivity. A separation of at least four layers is required to prevent overlap of the labeled polyanion molecules.[38,39]

This process description highlights a number of the advantages of using LbL assembly for surface modification. First, the simplicity of this method makes it very attractive. The only specialized equipment required is an automated dipping machine. Additionally, the materials used are often water soluble, and therefore one usually builds up these multilayers from dilute aqueous solutions. Compared to other popular deposition techniques such as chemical vapor deposition (CVD), the equipment costs and the hazardous chemical handling considerations are drastically reduced. Second, deposition takes place in a controlled manner in which growth at each step is self-limited. Since the surface charge reverses after the deposition of each layer, the amount of material that can be adsorbed at each step is intrinsically limited by electrostatic repulsion of the adsorbing species. This leads to assembled films which are very uniform and completely conformal meaning they coat all exposed surfaces of a textured substrate homogenously. As a result, nontraditional substrates such as colloidal particles[40-42] and porous templates[21,24,26,43] can be functionalized using LbL. Lastly, the self-limited growth mechanism also leads to predictable, linear film growth for most systems with the exception of the first few bilayers which sometimes deviate from steady state behavior due to surface effects. Another important exception is the exponential growth seen in deposition of multilayers which allow diffusion of the depositing species within the film.[44]

As discussed in the previous section, the configuration and charge density of an adsorbing polyelectrolyte molecule profoundly affects how it adsorbs. We can extend these ideas to predict how these molecules will act within an assembled film. Take for example the deposition of PAH and PSS at pH 4 in the absence of added salt. At this pH, both molecules take on expanded configurations and have high charge density as seen in Figure 1-3. When they adsorb, they will spread out on the surface, binding in many places. Sequential deposition leads to a fairly stoichiometric mix of PAH and PSS due to their similar charge densities and low bilayer thicknesses due to their expanded conformations. Since nearly every group on both chains is charged, there will be few free amine groups and few unbound charged groups. Due to the high density of ionic bonds between the polymer chains which act like weak cross-links, the film will not swell dramatically with solvent. A drawing showing this film schematically is included in Figure 1-4.

Now let us consider the assembly of PAH and PSS at pH 10 in the absence of salt. As shown in Figure 1-3 the PAH chain now has a much lower charge density and therefore a more compact configuration whereas the PSS chain remains expanded and highly charged. In this case, the multilayer will not be stoichiometric since it takes many more PAH chains with their low charge density to pair with the fully ionized PSS chains. Since PAH chains are more compact, they will also resist spreading out on the surface, resulting in thicker bilayers. There will also be a large number of amine functional groups within the film which can be used to perform further chemistry or to use as a handle for further manipulation. The ionic crosslink density will be significantly lower, leading to more dramatic swelling in solvent, particularly if the remaining amine groups are ionized after assembly. These are just two examples of the wide variety of film properties that are accessible by carefully controlling the conditions at which LbL assembly takes place. A more comprehensive introduction to this topic can be found in the work of Shiratori and Rubner who looked in detail at the way in which bilayer thickness depends on assembly conditions for two weak polyelectrolytes, PAH and PAA.[30]

Although the recent boom in LbL assembly has largely focused on polymers, this technique was actually first described by Ralph Iler who fabricated multilayers composed of colloidal silica and boehmite particles in the mid 1960s.[45] More recently a number of researchers have demonstrated the assembly of charged inorganic nanoparticles paired with polyelectrolytes or with oppositely charged nanoparticles.[10,17,27,40,46-54] This emphasizes that LbL assembly is not limited to polymers or biomacromolecules, but is also compatible with inorganic colloidal particles. Schematics showing polyelectrolyte assembly, polymer/nanoparticle assembly, and nanoparticle assembly are included in Figure 1-5.

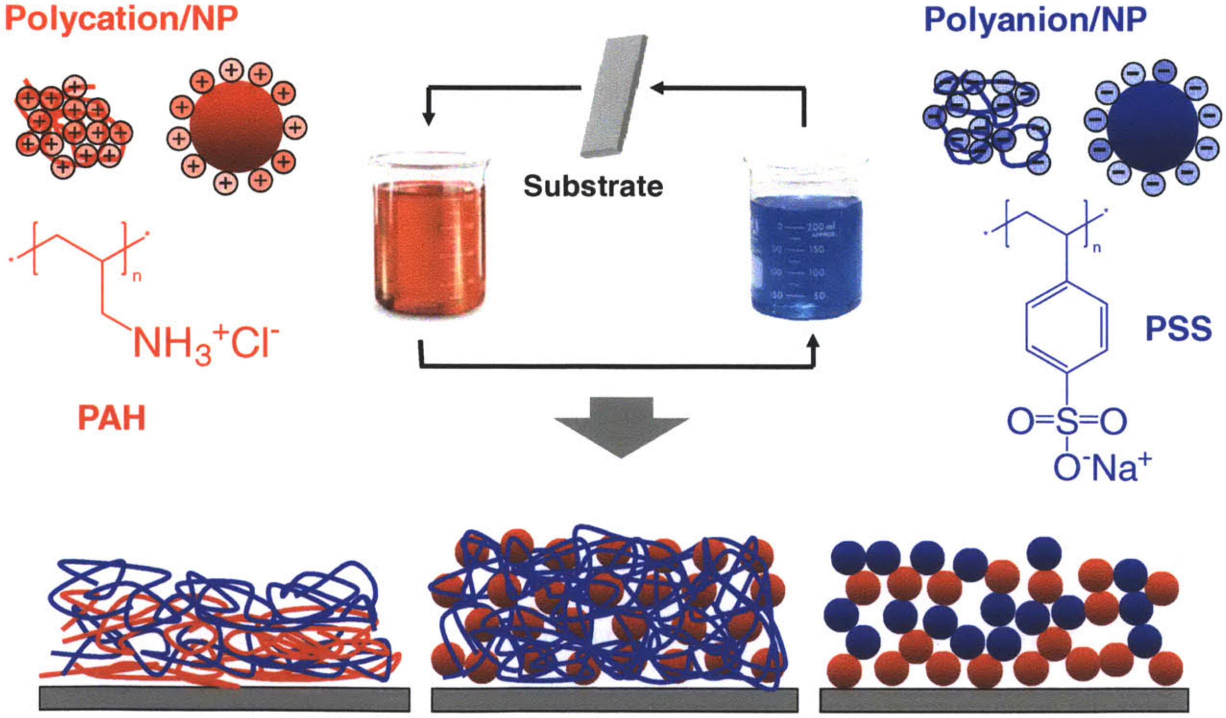

Figure 1-5 Schematic of LbL assembly of polyelectrolytes and charged nanoparticles. Polyelectrolytes can be paired with each other or with nanoparticles and nanoparticles can be assembled without the need for a polymer counterpart.

There are many advantages to being able to incorporate inorganic nanoparticles into a surface coating. One is to extend the range of chemistries which one can perform upon a multilayer after assembly. With polyelectrolytes, we are normally limited to organic functional groups such as amines, hydroxyl groups, carboxylic acids, etc. By incorporating nanoparticles one can take advantage of inorganic chemistry, especially the rich field of silica chemistry. In addition, nanoparticles are more tolerant of harsh chemical or physical conditions. One example of this is the calcination of nanoparticle-containing multilayers to partially fuse the nanoparticles and to selectively remove the polymer.[17,19] In another example, hydrothermal treatment was used to partially dissolve and fuse silica particles in order to drastically increase the mechanical robustness of a multilayer hard coat on polycarbonate.[51] Nanoparticle coatings also exhibit porosity with pore sizes on the order of the nanoparticle diameter due to the packing of the particles. This fact has been used to manipulate the optical properties of multilayer films to make antireflection coatings[46,47,55] and films which exhibit structural color.[19,27,28] This porosity has also been used to construct superhydrophilic coatings in which water wicks into the nanoporous coating almost instantaneously.[18]

Like polyelectrolytes, nanoparticles are sensitive to the conditions at which they adsorb. The nanoparticle surface charge changes with pH, affecting the ability of the nanoparticles to form multilayers as well as their stability in solution. In particular, if the zeta potential, a measure of the particle surface charge, is not high enough nanoparticles will not repel each other and will therefore begin to aggregate. In addition, the screening effect of increased ionic strength decreases the distance over which this repelling force can act, encouraging the aggregation of nanoparticles. Generally this is less of a problem for polyelectrolyte/nanoparticle assembly due to the flexibility and polyionic nature of the polymer coil. Essentially as long as the nanoparticle suspension itself is stable, it is fairly straightforward to deposit nanoparticles in concert with an appropriate polyelectrolyte. On the other hand, nanoparticle/nanoparticle assembly occurs appreciably over a relatively small range of conditions. This is because in addition to ensuring that both nanoparticle suspensions are stable, one also has to ensure that the zeta potentials of the two nanoparticle species are comparable in magnitude so that charge reversal can occur. Without this careful balancing, very thin layers (thinner than the nanoparticle diameter) are deposited with each step, indicating partial coverage due to incomplete charge reversal. Lee *et al.* undertook a detailed study of these effects for deposition of titania and silica nanoparticles and found that the bilayer thickness was especially sensitive to the pH of the silica nanoparticle suspension. In particular, significant assembly was only possible over a narrow pH range from 3 to 4.[48] On the other hand, titania nanoparticles were prone to aggregation above pH 4, leading to opaque films. The narrow window over which significant multilayer growth did occur is shown in Figure 1-6.

Nanoparticles introduce other complications as well. As mentioned previously, polyelectrolytes essentially irreversibly adsorb to a surface due to their flexibility which allows them to sample the surface and bind at multiple points. Although each of these ionic associations may not be that strong in and of itself, the fact that there are so many ensures that desorption is quite rare. Nanoparticles on the other hand are rigid and therefore are limited in the number of ionic bonds they can make with the surface to which they adsorb. Obviously if they are adsorbed in concert with a polyelectrolyte, the polymer takes care of this problem my sampling the surface of the nanoparticle and binding it tightly to the film. When oppositely charged nanoparticles are assembled, however, this limitation is quite important and greatly increases the chance of nanoparticle desorption and aggregation of oppositely charged nanoparticles.

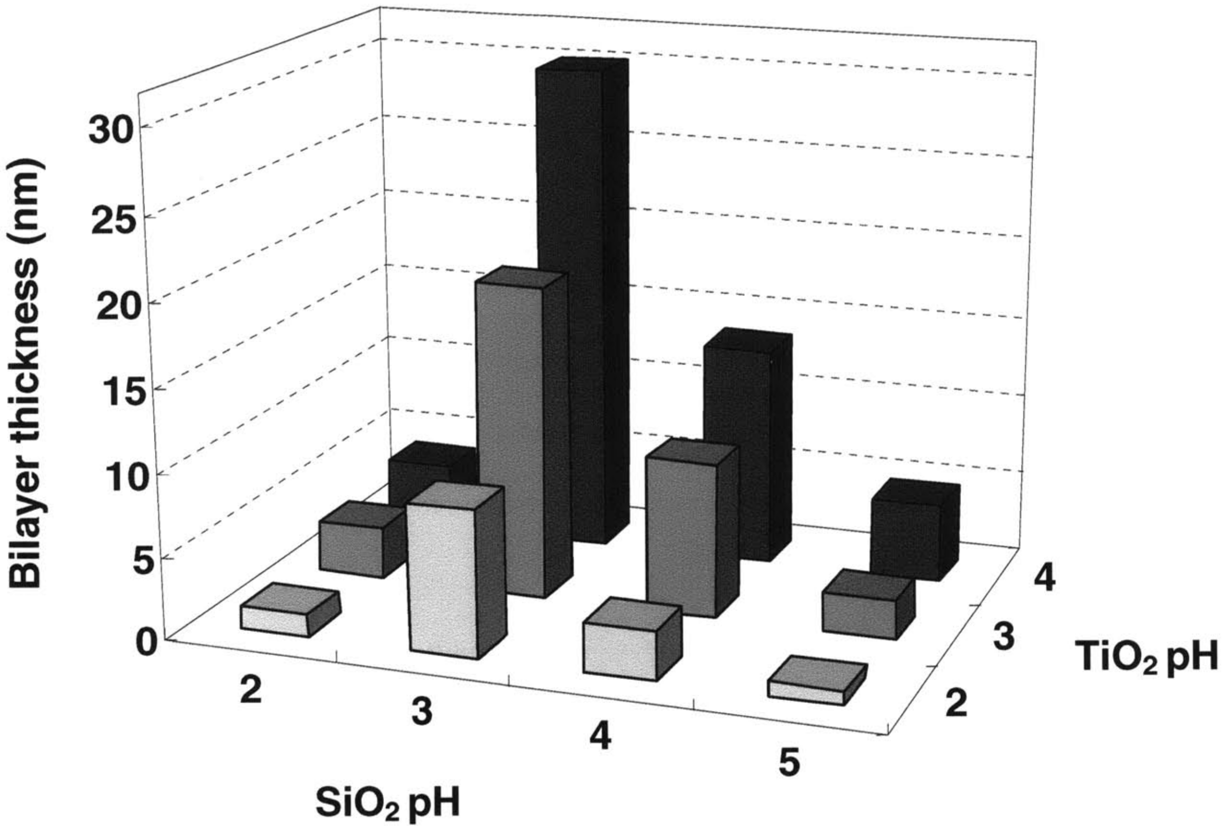

Figure 1-6 Silica/titania multilayer thickness as a function of the pH of the nanoparticle suspensions used to construct it. Reproduced with permission from Lee, D.; Omolade, D.; Cohen, R. E.; Rubner, M. F. *Chem. Mater.* **2007**, *19*, 1427-1433. Copyright 2007 American Chemical Society.[48]

In the following chapter we will introduce the second theme of this thesis, namely confined geometries. The methods by which they are manufactured as well as the special considerations which they raise will be discussed. The following three chapters will explore the LbL assembly of various polymer and nanoparticle pairs and the specific ways in which their assembly is affected by the unique substrates on which we deposit them. Chapter 6 will explore an effort to use the unique properties of these multilayers to form semipermeable membranes and in Chapter 7, the results will be summarized and future work building on this thesis will be discussed.

Chapter 2 Confined Geometries

Reproduced in part with permission from DeRocher, J. P.; Mao, P.; Han, J.; Rubner, M. F.; Cohen, R. E. Layer-by-Layer Assembly of Polyelectrolytes in Nanofluidic Devices. *Macromolecules* **2010**, *43*, 2430-2437. Copyright 2010 American Chemical Society.

Confined geometries are substrates whose dimensions are on the same order of magnitude as the phenomena of interest. At these tiny length scales, the continuum equations for mass transport and fluid flow no longer necessarily apply. Although devices with such small dimensions have enormous potential in the efficient analysis of complex samples, better understanding of nanoscale transport phenomena is essential in their development and application. As discussed briefly in the previous chapter, one of the advantages of LbL assembly is its ability to conformally and uniformly coat complicated geometries. In this chapter, we will describe the fabrication of high aspect nanochannels and track etched polymer membranes. We will then discuss some of the implications of these confined dimensions on LbL deposition.

2.1 Fabrication of Nanochannel Arrays and Devices

The top-down manufacture of microfluidic channels borrows from the incredible advances in silicon microfabrication technology and has the potential to pack a wide range of analytical techniques into a small, inexpensive device. As with transistor manufacture, the drive is always towards smaller feature sizes to allow a greater density of channels and therefore more functionality on a smaller chip. One relatively simple way to create extremely narrow nanochannels is to pattern a large area using photolithography and to then use chemical etching to form the third, confined dimension.[56] There are two major problems with this approach. First, covering this shallow channel is a significant challenge due to the relatively large width and extremely small depth of the nanochannel. This leads to problems with sagging of the cover material which then bonds to the floor of the channel, occluding most of its area. Second, even if channels are successfully formed and covered, they take up a fairly large area on the surface of the wafer and therefore devices with high nanochannel density and consequently high throughput cannot be made.

The obvious solution to this problem is to orient the channels in the other direction so that the channels are deep and thin rather than shallow and wide. The problem in this case is that patterning of these very small features is beyond the reach of conventional photolithography and instead requires specialized nanolithography techniques. Although features on the order of 50 nm can be patterned using electron beam lithography or focused ion beam lithography,[57,58] both of these processes are quite expensive and time consuming. To circumvent this problem, larger 1–2 μm channels can first be patterned using conventional lithography and then thermally treated to adjust the channel width to the desired value.[59] We have collaborated with the lab of Jongyoon Han of the Research Laboratory of Electronics at MIT who pioneered the manufacture of these high-aspect-ratio nanochannels. His student, Dr. Pan Mao, kindly produced many substrates containing nanochannel arrays and functional devices on which we performed LbL assembly. The methods by which he produced these unique and interesting features are described in detail below.[59]

The production of a nanochannel array begins with the deposition of silicon nitride on a (110) silicon substrate using low-pressure chemical vapor deposition (LPCVD). This thin layer was then patterned using standard photolithography to form approximately 1 μm wide lines which are parallel to the (111) crystal plane of silicon (Figure 2-1a). This patterned silicon nitride layer then served as a mask for anisotropic etching using KOH, taking advantage of the fact that KOH etches the (111) plane over one hundred times slower than the (110) plane.[60] The result is narrow, deep trenches as shown in Figure 2-1b. After removal of the silicon nitride layer, the wafer was heated to oxidize the silicon surface. This process leads to volume expansion of more than a factor of two, narrowing the width of the trench (Figure 2-1c). By adjusting the oxidation time, one can control the thickness of the nanochannel gaps down to 55 nm. For our purposes, the gap thickness was normally 300–400 nm with an aspect ratio of about 40, but aspect ratios on the order of 500 are possible using this technique.

This open array of nanochannels is very useful for characterization of LbL assembly on these substrates but because the channels are open, it is completely useless as a nanofluidic device. As a result, a procedure which allows for the capping of the nanochannels had to be devised. It is easy to imagine bonding glass or silicon to the top of the "posts" of the nanochannel array, but ensuring that the channels are completely sealed and isolated from each other is difficult. Instead the channels were capped using non-conformal silica deposition during the fabrication process. To allow the nanochannels to be interfaced with fluid delivery systems, reservoirs and a series of microchannels were also constructed.

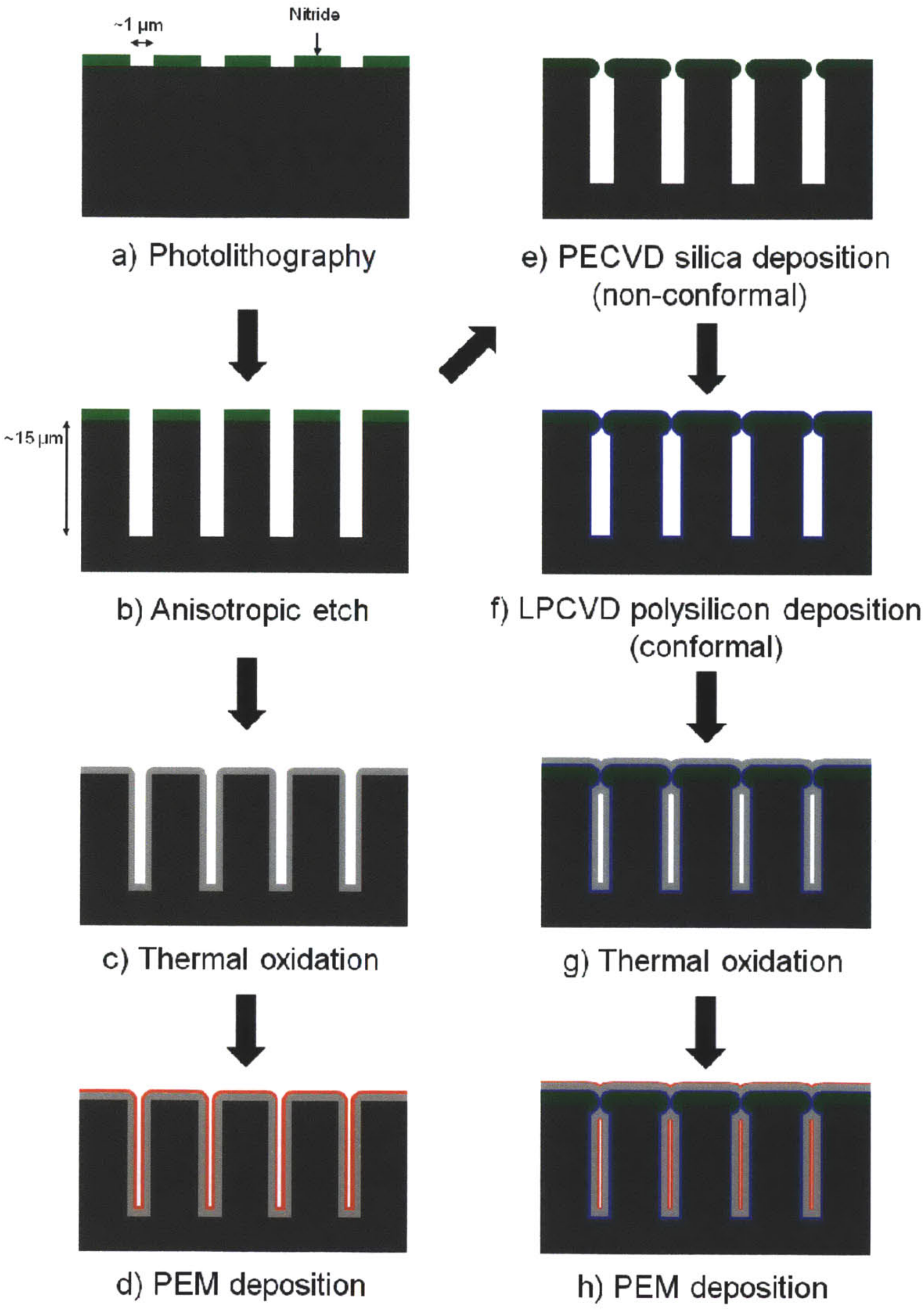

Figure 2-1 Schematic of the fabrication process used to form a sealed nanochannel array. Open arrays were formed by skipping the PECVD and LPCVD steps.

After photopatterning and KOH etching of deep trenches as above, plasma-enhanced chemical vapor deposition (PECVD) silicon oxide (Figure 2-1e) and LPCVD polysilicon (Figure 2-1f) were sequentially deposited on the trenches. The combination of the non-conformal PECVD and conformal LPCVD processes allows us to maintain a uniform gap size along the trench after deposition while sealing the trenches completely and eliminating the rounded shape resulting from oxidation of the silicon posts. After sealing the nanochannel array, microchannels were defined by standard photolithography and etched to the same depth as the nanochannel array using deep reactive ion etching (DRIE). Finally, thermal oxidation was used to narrow the gap size within the nanochannels to the desired initial value for the LbL coating experiments (Figure 2-1g). Although the nanochannels were sealed from the top, the length of the nanochannels *i.e.* the distance between microchannels was only 30 μm so that adsorbing species could still diffuse into the nanochannels from both ends. All silicon surfaces were passivated with oxide to form an insulation layer, needed for subsequent conductance measurements. The device layout and scanning electron microscopy (SEM) images of the device are shown in Figure 2-2.

The device design incorporates six reservoirs and six wedge-shaped conduits which ultimately narrow into three parallel 100 μm microchannels. These wedges contain many pillars which serve to support the device cover which is made from poly(dimethylsiloxane) (PDMS). These six channels are very wide to cut down on the resistance they offer to transport within the device. Although then nanochannels are very thin, they are also very short so that in order for their resistance to be measurable, the long microchannels must also be very wide. The three parallel microchannels are bridged by an array of ten nanochannels, each about 15 μm deep, 30 μm long, and about 240 nm wide with an aspect ratio in excess of 60. The corrugated "floor" of a microchannel along with the nanochannels which comprise its wall are shown in Figure 2-2. The corrugation seen on the bottom of the microchannel is due to overetch when the microchannel was etched into the wafer which already included a nanochannel array.

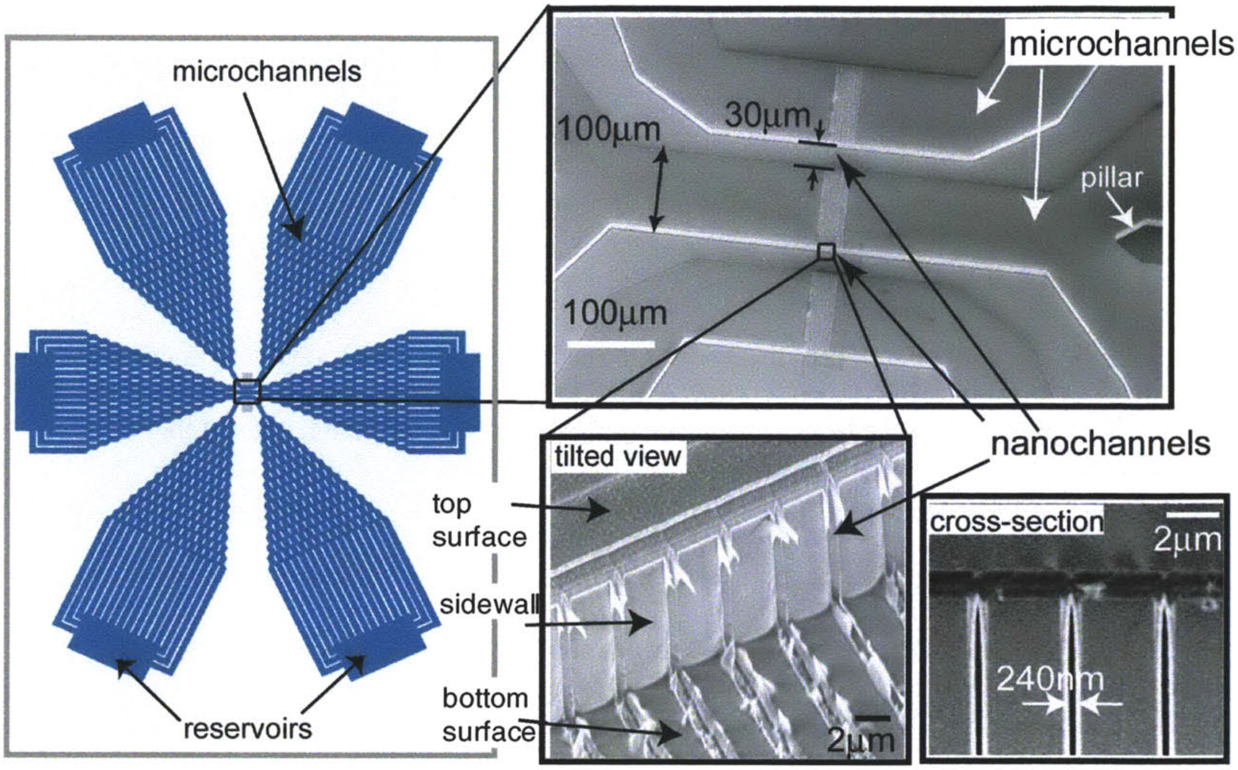

Figure 2-2 Schematic and SEM images of the device used for the DC conductance measurements. The device consists of a nanochannel array which bridges a series of microchannels. The pyramid-shaped microchannels are used to ensure low resistance relative to the nanochannels and the pillars are required to prevent the channels from collapsing. The interface between the nanochannels and microchannels is shown in tilted-view and cross-sectional SEM images. The nanochannel is 30 µm long and 240 nm wide. The width of the microchannels is 100 µm. All channels have a depth of 15 µm. The trenches in the bottom surface near the nanochannel array are due to the overetching of the nanochannel array pattern during subsequent etching of the microchannels. Courtesy of Dr. Pan Mao.

In order to form closed microchannels, a bonding protocol was developed to cap the channels after polyelectrolyte multilayer (PEM) deposition. As reported previously, O_2 plasma can be used to selectively etch a PEM film from an exterior surface, while leaving the same coating intact within small pores.[26] We removed the exposed PEM, which was covering the bonding surface, while leaving the coating inside the nanochannels intact. We found that 30 s of O_2 plasma etching (100 mTorr, 100 W) per bilayer of PAH/PSS deposited is sufficient to remove the PEM film on the top surface while leaving the film inside the nanochannels intact (see Figure 2-3). A slab of PDMS (with pre-punched holes corresponding to the device reservoirs) and the plasma-cleaned device were subjected to O_2 plasma for 1 min, and then aligned and brought into contact. The bonded device was then placed on a hotplate at ~90 °C for a few hours to increase the bonding strength.

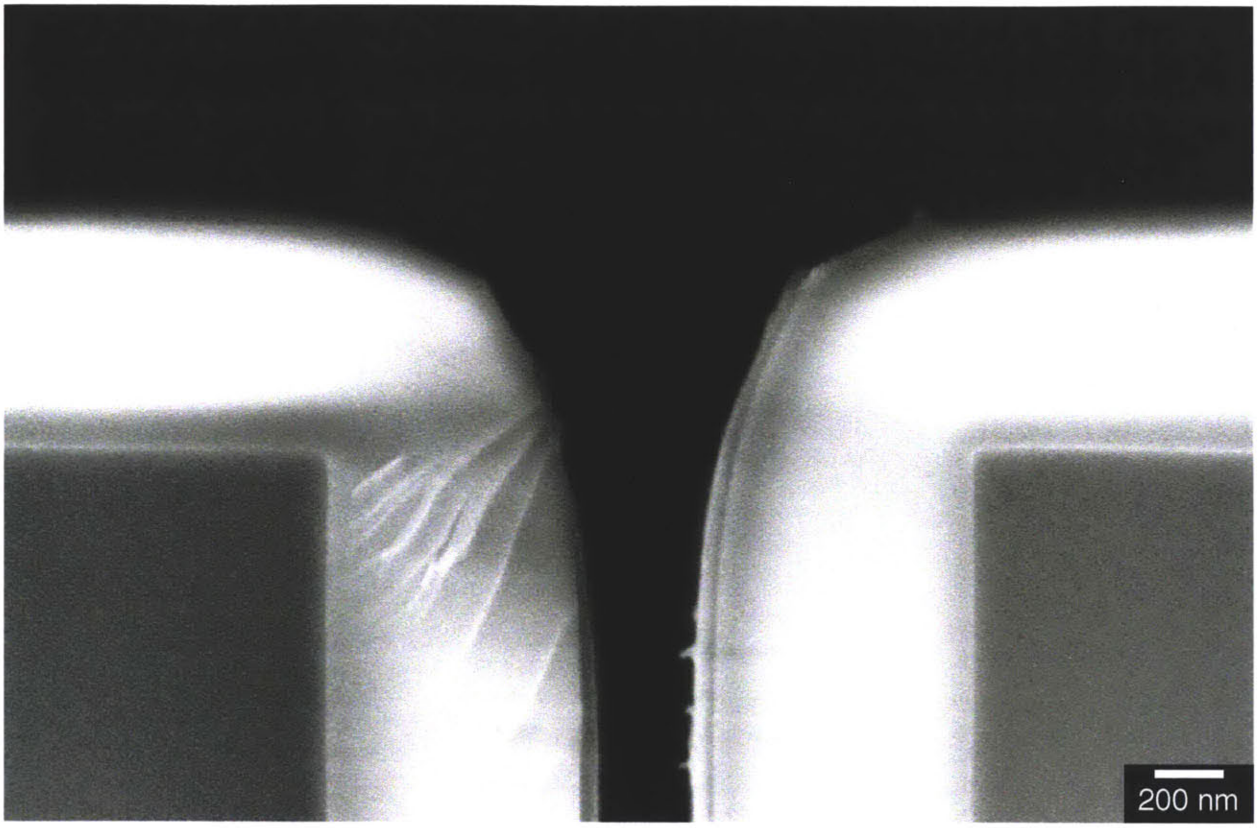

Figure 2-3 Micrograph showing selective O_2 plasma etching of a PAH/PSS multilayer from the top of the posts while the coating within the channels remains intact. Micrograph courtesy of Dr. Pan Mao.

2.2 Track Etched Polycarbonate Membranes

Silicon-based microfabrication offers an excellent platform for proof-of-concept studies, however it is not the only way to make substrates with well-defined features on the nanoscale. In the early 1960s, researchers found that bombardment of minerals with heavy ions results in damaged tracks within these materials.[61,62] These tracks are completely straight and roughly circular in cross section. They also turn out to be susceptible to selective etching using appropriate reagents and thermal conditions. In this way, the damaged material can be etched away to form cylindrical pores. This approach has been extended to a wide variety of insulators including polymers such as polycarbonate and poly(ethylene terephthalate).[63,64] This technique is sometimes used to detect heavy ions and observe their tracks, but it is much more commonly used in the production of track etched membranes, which are widely commercially available. See Figure 2-4 for micrographs of commercially available track etched polycarbonate (TEPC) membranes.

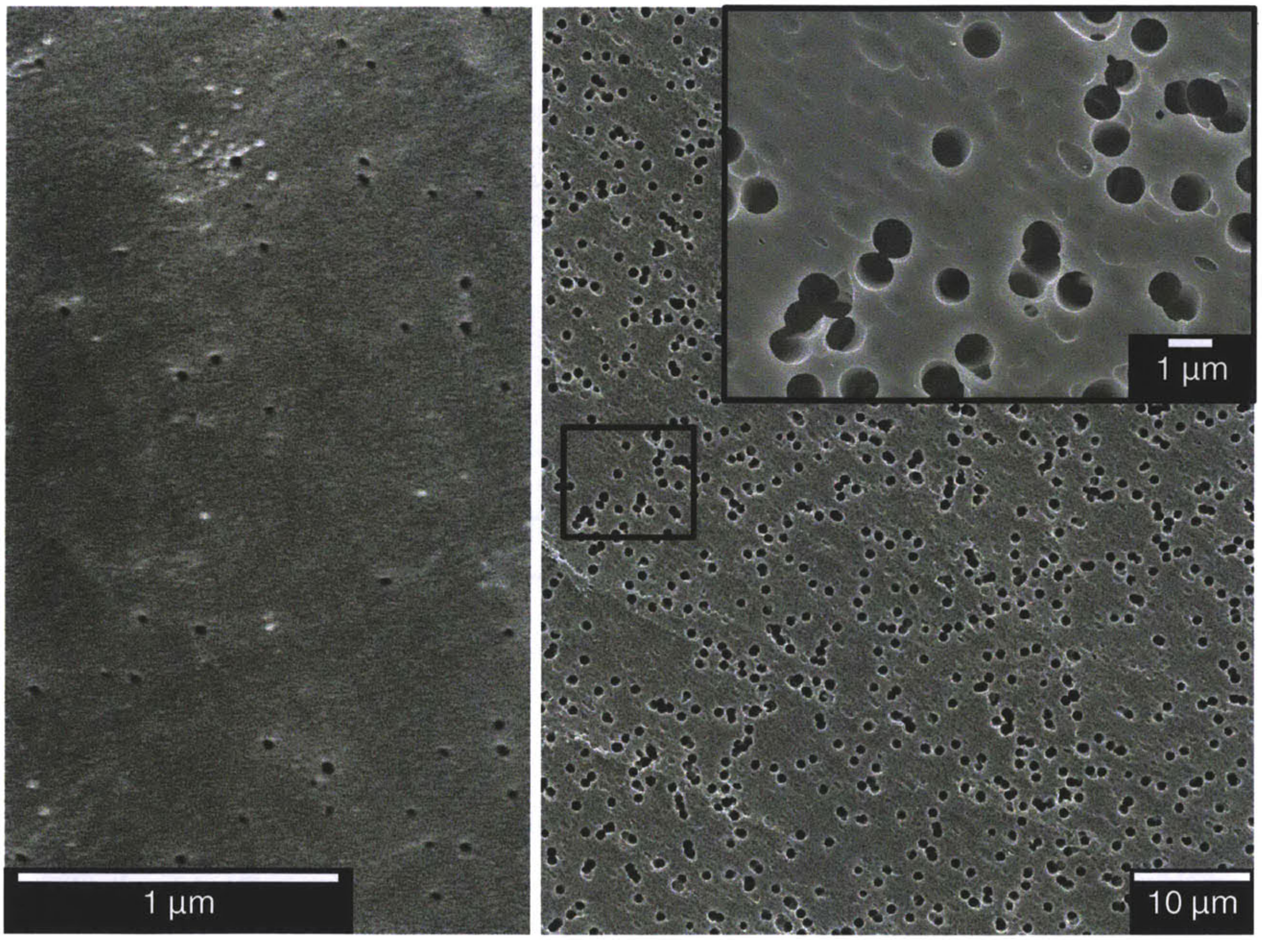

Figure 2-4 Micrographs of track etched polycarbonate membranes. The membrane on the left nominally has 10 nm pores. The membrane on the right is specified to have 1 µm pores. The inset in the upper right is a magnified view of the film with 1 µm pores and shows the cylindrical nature of the pores as well as examples of merged pores. These micrographs were obtained during work at the University of Minnesota.

To form straight, aligned pores, the incoming radiation is collimated, ensuring that the resulting tracks are mostly normal to the film. This method also allows for somewhat independent tuning of the pore diameter and pore density. The ion tracks result from completely random heavy ion bombardment, so the pore density is controlled by changing either the radiation flux or the time of exposure. The diameter of the pores on the other hand is controlled by the etching conditions which the film is exposed to after bombardment. By changing the concentration of the etchant, and the time and temperature of exposure, one can control the extent to which the damaged tracks are etched. This etching process results in quite monodisperse pores that range from a few nanometers up to many microns in diameter with aspect ratios on the order of 500 possible. Due to the random nature of the bombardment process however, there are practical limits on the pore density and monodispersity that can be achieved. If two tracks are close enough to each other that subsequent etching results in their merger, then the pore will be twice as big as it should be and selectivity will suffer. To preserve selectivity, the bombardment must be limited to minimize the probability of such "double hits."

Another prominent example of structured porous materials is the anodic oxidation of aluminum.[65] These membranes, known as anodized aluminum oxide (AAO) membranes, have well defined, often conical pores and much higher void fractions. Hexagonally-packed cylindrical pores which are ordered over large areas have also been produced.[66] These materials are also widely commercially available, but are much more difficult to work with due to the fairly brittle nature of alumina. Track etched polycarbonate membranes are quite flexible and therefore much easier to work with in practice for the experiments we are interested in.

2.3 Electrostatic Interactions in Confined Geometries

One of the prime reasons from the intense interest in nanofluidic devices is the fact that their dimensions are on the same order as the Debye length, meaning that electrostatic effects which are normally ignored in macroscopic systems become important or even dominant. The interface between a charged solid and a liquid has a special electrostatic environment due to the fact that surface charges are fixed both in their strength and position. To compensate for these charges and satisfy electroneutrality, charged counterions accumulate near the surface. This phenomenon results from a balance between electrostatic forces which drive ions to the wall and the concentration gradient which would tend to drive them away. The excess concentration of counterions near the surface (or equivalently the electrostatic potential) decays exponentially as one moves away from the surface. The characteristic length over which this decay occurs is known as the Debye length:

$$\lambda_D = \sqrt{\frac{\varepsilon_0 \varepsilon_r RT}{F^2 \sum_i c_i z_i}} \tag{2.1}$$

where ε_0 and ε_r are the permittivity of free space and the relative permittivity of the medium *i.e.* the dielectric constant, R is the gas constant, T is temperature, F is Faraday's constant, and c_i and z_i are the concentration and charge on ion i in solution. For a monovalent electrolyte, this quantity ranges from 3 Å at 1 M to nearly 1 μm for pure pH 7 water. Clearly the nanofluidic channels described above have dimensions comparable to the Debye length at moderate ionic strengths. A schematic representation of an electrical double layer is given in Figure 2-5.

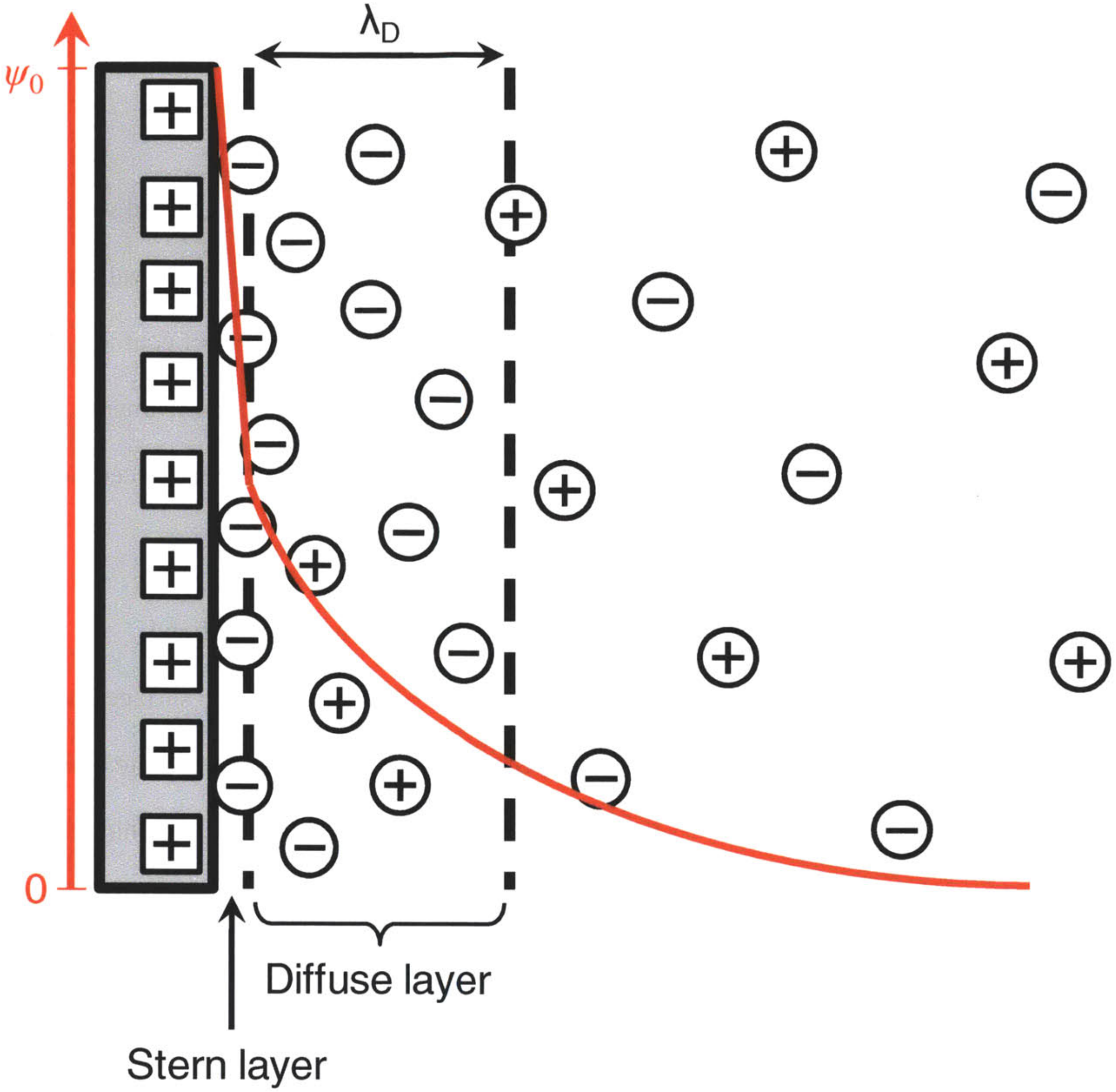

Figure 2-5 Schematic of an electrical double layer resulting from a positively-charged surface in contact with an electrolyte solution. The counterions and co-ions are depicted as circles with negative and positive signs respectively. The immobile charged surface groups are represented by squares. The electrical potential is represented by the red curve. Adapted from Hiemenz and Rajagopalan.[67]

In this figure we can see that the surface is assumed to be positively charged resulting in adsorbed counterions at the surface. In this layer, known as the Stern layer, the ions cannot be accurately represented as point charges and the potential is assumed to be linear. The Gouy-Chapman theory, which predicts an exponential decline in the potential with a decay constant of

λ_D is then applied to the diffuse, or double layer. The diffuse layer is enriched in negative counterions near the edge of the Stern layer and gradually approaches the bulk conditions in which counterions and co-ions have equal concentrations.

In a confined nanochannel, which has two closely-spaced surfaces, each charged wall induces an electrical double layer in the solution with which it is in contact. If the walls are close enough together, these double layers will overlap, resulting in a large number of counterions and very few co-ions within the channel, a phenomenon known as the exclusion-enrichment effect.[68] In essence, an electrostatic barrier has been set up which lowers the equilibrium concentration of co-ions within the channel.

Analogous arguments can be made for polyelectrolytes diffusing into confined nanochannels. In conventional polyelectrolyte adsorption on a planar, charged surface, the diffusing polyelectrolyte molecule does not encounter the double layer until it is quite close to the surface. It may be driven away by the double layer or it might adsorb, strengthening the surface charge reversal and therefore increasing the strength of the double layer. This along with the finite number of electrostatic binding sites available is what leads to the self limiting nature of polyelectrolyte adsorption. In contrast, a polyelectrolyte molecule attempting to diffuse into a nanochannel encounters the double layers from each side of the channel right away and must diffuse across this electrostatic barrier. The result is a much lower equilibrium concentration of polyelectrolyte throughout the channel due to the exclusion-enrichment effect.

Theoretical work by Böhmer *et al.* has shown that this effect is important for adsorption of strong polyelectrolytes within confined nanochannels. Their self-consistent field simulations show that for low gap sizes and low ionic strengths *i.e.* when the Debye length is large relative to the channel width, significant depletion of polyelectrolyte within the channel is predicted.[69] As the following chapters will show, these considerations result in interesting differences between LbL assembly on planar surfaces and in confined geometries. This raises concerns which must be taken into account when using LbL assembly to functionalize confined surfaces, but shows that functionalization with a number of different materials is possible, opening up new possibilities for devices which require surface coating of features with such small dimensions. In particular, one can manipulate the conditions at which deposition takes place and the materials which are deposited in order to selectively coat or seal off certain parts of a device based on their level of confinement.

Chapter 3 Layer-by-Layer Deposition of Polyelectrolytes in Confined Geometries

Reproduced in part with permission from DeRocher, J. P.; Mao, P.; Han, J.; Rubner, M. F.; Cohen, R. E. Layer-by-Layer Assembly of Polyelectrolytes in Nanofluidic Devices. *Macromolecules* **2010**, *43*, 2430-2437. Copyright 2010 American Chemical Society.

3.1 Introduction

LbL assembly has shown great utility in surface modification and functionalization, serving as a general method for assembling nanocomposite thin films made up of polyelectrolytes, nanoparticles, and biomacromolecules on a wide variety of substrates and geometries.[70] These films have been used to manipulate the optical[17,19,46,71,72] and wetting[8-10,17-19] properties of a surface and to impart antibacterial,[1-3,73-75] cytophilic,[5-7] magnetic,[2,26] and antifog,[18,20,76] properties. Multilayers have also been used to achieve chemical or biological recognition and to control flow in microfluidic devices.[77]

Lithography provides a robust means of mass-producing devices with micro- and nanoscale features. Although this technique had its birth in the semiconductor industry, its utility has been well-demonstrated in the top-down fabrication of micro- and nanofluidic devices. These devices hold great potential in performing chemical and biological analyses on a very small scale, as the analytical equipment and the required sample and reagent volumes can be minimized. These devices have been utilized in technologies such as biosensing,[78,79] biomolecule separation,[59,80-84] and sample preconcentration.[85] Many current and potential applications depend on functionalization of the surfaces of these devices. LbL assembly provides the conformal coating necessary for surface functionalization, even for high aspect ratio nanoscale geometries, due to the self-limiting adsorption intrinsic in the process. Our aim is to combine these two robust technologies, LbL and nanofluidics, to create hybrid devices which might allow a wide range of new applications. LbL coating within nanofluidic devices provides a method of further "narrowing" nanochannels controllably, potentially down to tens of nanometers, without involving complicated fabrication methods. In addition, a wide variety of chemical functionalities available from LbL technology can be employed, while maintaining tight control of structural parameters such as pore size.

LbL assembly in confined geometries has been studied previously with two main goals: the coating of microporous or nanoporous sacrificial templates for the formation of structured materials[24,26,86-88] and deposition within microporous and nanoporous materials as well as microfluidic devices to impart novel functions.[21,41,43,77,89-94] Though the utility of multilayer deposition in confined geometries is significant, there is a lack of consensus on how confined LbL assembly differs from standard, flat substrate deposition. In particular, others have noticed discrepancies between confined and unconfined bilayer thicknesses. Although bilayer thickness can be affected by many factors such as assembly conditions and substrate or polymer chemistry, in these studies efforts were made to compare confined and unconfined deposition under the same conditions.

One example, by Lee *et al.*, concerns the deposition of PEMs on porous TEPC membranes using PAH and PSS.[21] In that work, PAH/PSS multilayers were successfully assembled within the 400 and 800 nm cylindrical pores. Bilayer thicknesses within the pores were about 20% larger than on a flat substrate, a result that was attributed to incomplete drainage of solution from the pores during the assembly process. Lee *et al.* also reported that as the multilayers swell within the pores, they fail to completely close the cylindrical pores; stress caused by the shrinking annular opening and electrostatic repulsion were offered as possible explanations for this observation.

Similar PEM deposition experiments on nanoporous substrates were carried out by Alem *et al.* using poly(vinylbenzylammonium chloride) and PSS.[95] The substrates used were TEPC membranes with pore diameters ranging from 57–845 nm. They reported bilayer thicknesses within the pores that were forty times higher than those on a flat substrate and attributed this result to the formation of a dense gel within the pores due to higher local polymer concentrations.

Another example of LbL polymer deposition in confinement is the tuning of photonic crystals using PAH and PSS as well as organometallic polyelectrolytes as reported by Arsenault *et al.*[43] The substrate used was a photonic crystal made up of close-packed, 270 nm colloidal silica microspheres. Arsenault reported five times smaller bilayer thicknesses within the crystal than on the surface of the crystal and attributed this result to exclusion, hindered diffusion, and bridging of polyelectrolyte molecules due to extreme confinement near the contact points of the colloidal particles.

Wang *et al.* have also reported LbL deposition of PAH and PAA in mesoporous silica particles with 3–40 nm pores to form nanoporous polymer spheres after selective dissolution of the silica template.[42,96] Thermal cross-linking of the multilayer after each deposition step was used to stabilize the polymer structure. Experiments showed that stable nanoporous polymer spheres could not be formed using porous silica particles with 2–3 nm pores, suggesting that these pores were too small to allow polyelectrolyte infiltration.

These conflicting reports comparing the bilayer thickness in confined geometries to that on flat geometries provide further motivation for systematic study of LbL deposition in structures such as micro/nanochannels. In this work we employ planar, essentially monodisperse rectangular channels with lateral dimensions ranging from 200–500 nm and depths of 10–15 μm, resulting in aspect ratios of 20–75. These channels have been developed for use in biomolecule separations and sample preconcentration[59] and provide a model experimental platform to study LbL deposition in confinement. The high throughput and high surface area in these integrated micro/nanofluidic devices combined with the ability to manipulate the chemical functionality of the device surface via LbL suggests further applications in biomolecule or chemical detection, selective separation, and heterogeneous chemical or biochemical reactions. These and other technologies will benefit from a detailed understanding of how multilayer growth within confined nanochannels compares to the well-studied case of deposition on planar surfaces.

PEMs can be used to impart a broad set of novel functionalities to a nanochannel device including stimuli-responsiveness, reversible switching of the channel gap thickness,[21] manipulation of the sign and/or the density of the surface charge, chemical functionality and wettability of the channel walls. For instance, LbL assembly has been applied to microfluidic devices as a means of controlling the surface charge of the channel walls.[77,90] Barker *et al.* reported that PAH/PSS multilayers could be used to create complicated electroosmotic flow patterns including flow in opposite directions in the same channel.[77] Sui and Schlenoff showed that multilayers made from PSS and a mixture of poly(diallyldimethylammonium chloride) (PDAC) and PDAC-co-PAA could be used to switch the direction of electroosmotic flow using a pH swing.[90] LbL assembly can also be used to incorporate functional nanoparticles and biomacromolecules within a surface coating, serving as a simple and general method for surface functionalization within the confined geometry of the nanochannels. Liu *et al.* reported LbL assembly of PDAC and gold nanoparticles as a biocompatible, high surface area multilayer for adsorption of enzymes.[92] They coated poly(ethylene terephthalate) microchannels with this polymer/nanoparticle multilayer and immobilized trypsin on it. This catalytic microfluidic channel was found to be an efficient protein digestion device.

In this work, we use the well-studied PAH/PSS polyelectrolyte pair[97] deposited at pH 4 and different ionic strengths. PSS is a strong polyanion which is essentially fully ionized at any pH. In contrast, PAH is a weak polycation whose degree of ionization is sensitive to pH. At pH 4, PAH is essentially fully ionized, yielding multilayers that are relatively smooth and uniform and also fairly resistant to swelling in aqueous solution. These qualities make this system a favorable one for the systematic tuning of the gap thickness in high aspect ratio channels.

3.2 Experimental Section

Materials

PAH (M_w = 56,000) and PSS (M_w = 70,000) were purchased from Sigma-Aldrich. NaCl was purchased from Mallinckrodt. Silicon wafers were obtained from WaferNet Inc. and glass slides were purchased from VWR. PDMS was made using the Sylgard 184 kit from Dow Corning. The polymer mixture was cured under vacuum at 65 °C overnight. (110) silicon wafers for nanochannel fabrication were obtained from EL-CAT Inc. Ag/AgCl electrodes were purchased from A-M Systems, Inc. and the conductivity probe and meter were obtained from VWR. Nanochannel arrays and hybrid micro/nanofluidic devices were fabricated as described in Section 2.1 The layout of the device and an equivalent circuit diagram are shown in Figure 3-1.

PEM Deposition

For experimental convenience, silicon devices were mounted on glass slides by bonding the unpatterned side of the device with the glass substrate using double-sided tape (468MP, 3M). Polyelectrolyte solutions consisting of 10 mM polyelectrolyte (on a repeat unit basis) and salt concentrations ranging from 0 to 1 M were prepared using deionized (DI) water (18 MΩ·cm, Millipore) and adjusted to pH 4.0 using 1.0 M HCl (Sigma-Aldrich). The pH of the rinse water was also adjusted to match that of the polyelectrolyte solutions in order to avoid pH drift over the course of an experiment. Both polymer and rinse solutions were filtered using 0.2 μm polyether sulfone filtration membranes (VWR). The samples were dipped into baths containing either polyelectrolyte or rinse solutions using a programmable slide stainer (Zeiss, Inc.). The substrates were first dipped into the polycation (PAH) solution, followed by dipping into three rinse baths. The substrate was then dipped into the polyanion (PSS) solution followed by three rinses. This process, which constitutes the assembly of one bilayer, was then repeated to form the PEM. The dip times for the polycation/polyanion and three rinse baths were 40, 10, 10, and 10 min respectively. After deposition, the samples were immediately dried with compressed air.

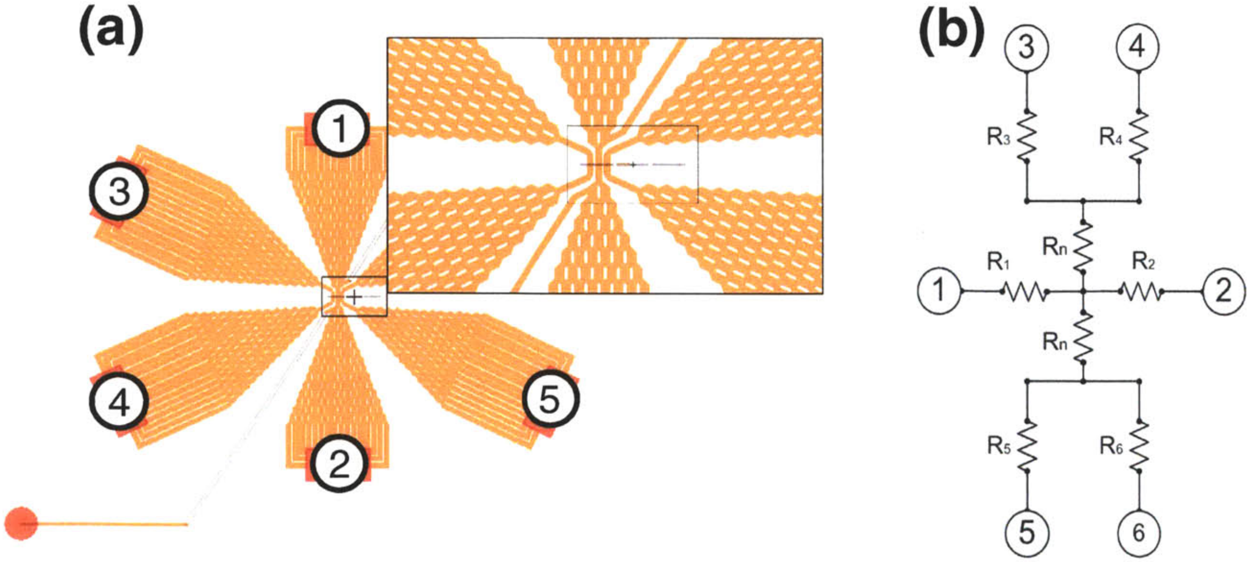

Figure 3-1 Schematic showing the nanofluidic device used in this work. (a) Layout of the device employing wide microchannels which funnel down to three parallel microchannels bridged by nanochannels. The inset shows a magnified view of the microchannel/nanochannel junction. (b) Equivalent circuit diagram with the resistances of each microchannel and nanochannel noted. Courtesy of Dr. Pan Mao.

Characterization

The thickness and conformality of PEM films assembled within the nanochannels were determined using SEM (JEOL 6320, Zeiss Supra-40). The SEM samples were prepared by fracture of the coated silicon substrates using a diamond scorer. The dry film thicknesses of PEMs coating the open nanochannel geometry were measured using image analysis tools built into the SEM software. The micrographs were also used to qualitatively evaluate the roughness and conformality of the polymer coating.

The thickness of a PEM on a flat silicon substrate in equilibrium with a particular aqueous solution was determined using *in situ* spectroscopic ellipsometry (XLS-100, J.A. Woollam Co., Inc.). In these experiments, the sample was placed in a custom-made quartz cell[17] which was filled with the solution of interest. The resulting data were fit to a Cauchy model to determine the wet state film thickness.[97] Spectroscopic ellipsometry was also used to determine the dry PEM thickness on flat silicon substrates. Profilometry (P-16+, KLA-Tencor) was also performed on a number of flat substrate samples in the dry state. The dry state thickness values obtained from profilometry were systematically lower than those for ellipsometry, but were generally within 2% of the ellipsometry results. The wet state (1 M KCl) thicknesses on flat substrates were about 26% larger than the corresponding dry state values (see Figure 3-2).

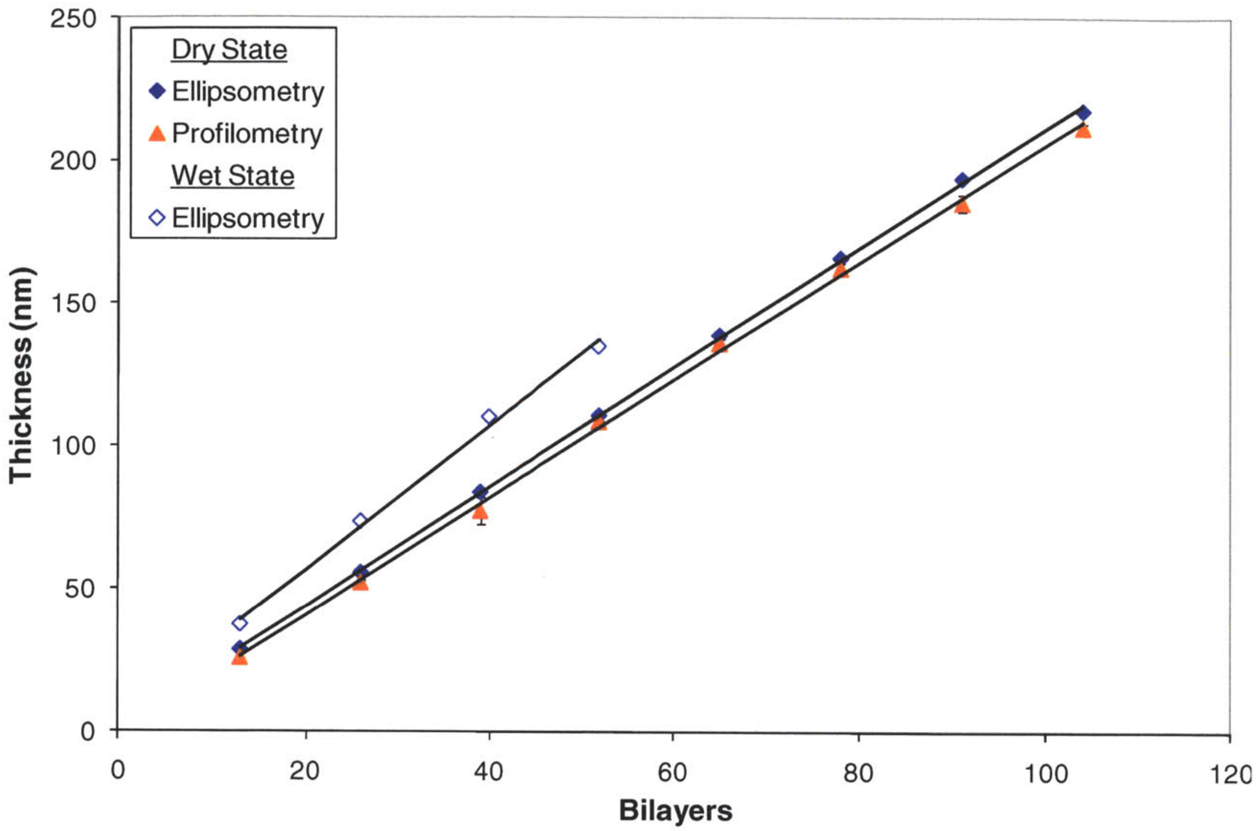

Figure 3-2 Comparison of dry-state PEM thickness measurements obtained by ellipsometry (blue diamonds) and profilometry (orange triangles) with wet-state (1 M KCl) thickness values (open diamonds). The PEM consists of PAH and PSS assembled at pH 4.0 on a silicon wafer. The best fit slopes for the dry-state ellipsometry and profilometry data are 2.09 and 2.06 respectively and have R^2 values of 0.999. The best fit slope for the wet-state ellipsometry data is 2.52 and the R^2 value is 0.996.

DC Conductance Measurement

The DC conductance measurements were used to determine the ionic flux through the channels, from which estimates of the gap thickness could be made. These experiments were performed using a Keithley 236 source/measurement unit. Before measuring the electrical conductance of a device, it was first soaked in a solution of 1M KCl overnight. The device was flushed with fresh KCl solution and allowed to stand for a few minutes to allow the liquid level in each reservoir to equilibrate. This was done to prevent convection from affecting the conductance measurements. The device was connected to the voltage source by two Ag/AgCl electrodes placed into two specified reservoirs. Ag/AgCl electrodes were used to prevent overpotential during the measurement. A low voltage sweep from -0.5 V to +0.5 V was performed at a rate of 0.01 V/s. The Keithley 236 was controlled using a custom-made LabView 7.0 program. The DC conductances of channels were determined by fitting the slope of the ionic current as a function of the applied voltage (*I*-*V* plot). These plots always showed very linear behavior, with R^2 values of at least 0.99, confirming that we have an ohmic system (see Figure 3-3 for a representative plot).

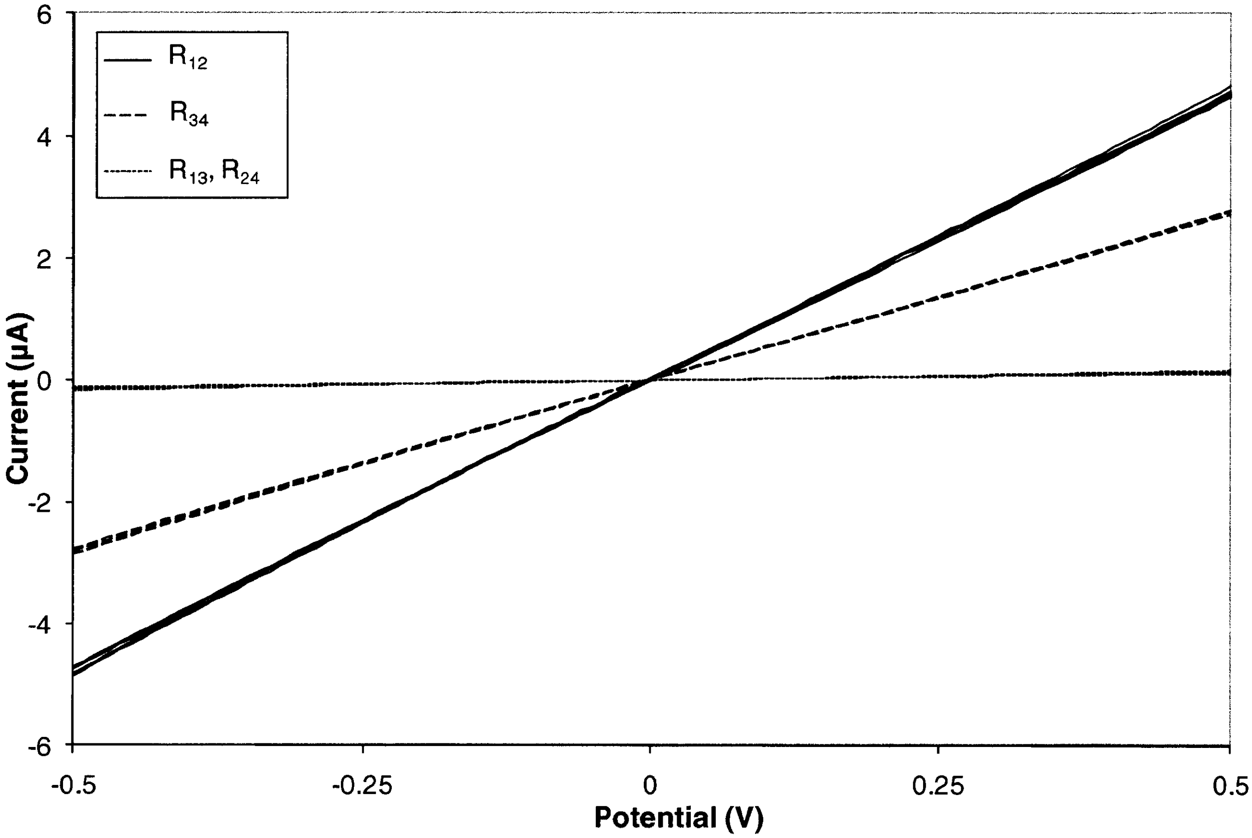

Figure 3-3 Representative *I*-*V* plots obtained by performing a voltage sweep and measuring the current between two reservoirs. The solid lines represent the resistance between reservoirs 1 and 2 in Figure 3-1, the large dashed lines represent the resistance between reservoirs 3 and 4 in Figure 3-1, and the short dashed lines represent the resistances between reservoirs 1 and 3 and between reservoirs 2 and 4 in Figure 3-1. In this case, the device was coated with 60 bilayers of PAH/PSS and the electrolyte used was 1 M KCl. The linear nature of these data confirms that the experiment was carried out in the ohmic regime.

The nanochannel conductance S_n can be written as:[68]

$$S_n = \frac{1}{R_n} = (\mu_{K^+} + \mu_{Cl^-})\left(c_{KCl} e \frac{W_n H_n}{L_n} + \sigma_s \frac{H_n}{L_n} \right) \tag{3.1}$$

where R_n is the resistance, μ_i is the mobility of species i, c_{KCl} is the concentration of KCl, e is the elementary charge, σ_s is the surface charge density, and W_n, H_n, and L_n are the dimensions of the nanochannel (see Figure 3-4). At high salt concentrations (for example 1 M KCl), where $W_n >> \lambda_D$ (Debye length) and $|\sigma_s| << ec_{KCl}W_n$ we can ignore the second term, which is governed by surface charge, and assume idealized, inert channel behavior, modeled as ideal resistors.[98] The equivalent channel circuit of the device is shown in Figure 3-1b.

To determine the conductance of the nanochannels, one must first account for the resistance of the microchannels which connect the reservoirs to the nanochannel array. For the circuits between the reservoirs (1) and (2) we know that:

$$R_{12} = R_1 + R_2 \tag{3.2}$$

where R_{ij} is the resistance between reservoirs i and j. Similarly, between (3) and (4), we have

$$R_{34} = R_3 + R_4 \tag{3.3}$$

For the circuits which include the nanochannels we have:

$$R_{13} = R_1 + R_3 + R_n \tag{3.4}$$

$$R_{24} = R_2 + R_4 + R_n \tag{3.5}$$

where R_n is the resistance of the nanochannel array. Solving for R_n we can write:

$$R_n = \frac{R_{13} + R_{24} - R_{12} - R_{34}}{2} \tag{3.6}$$

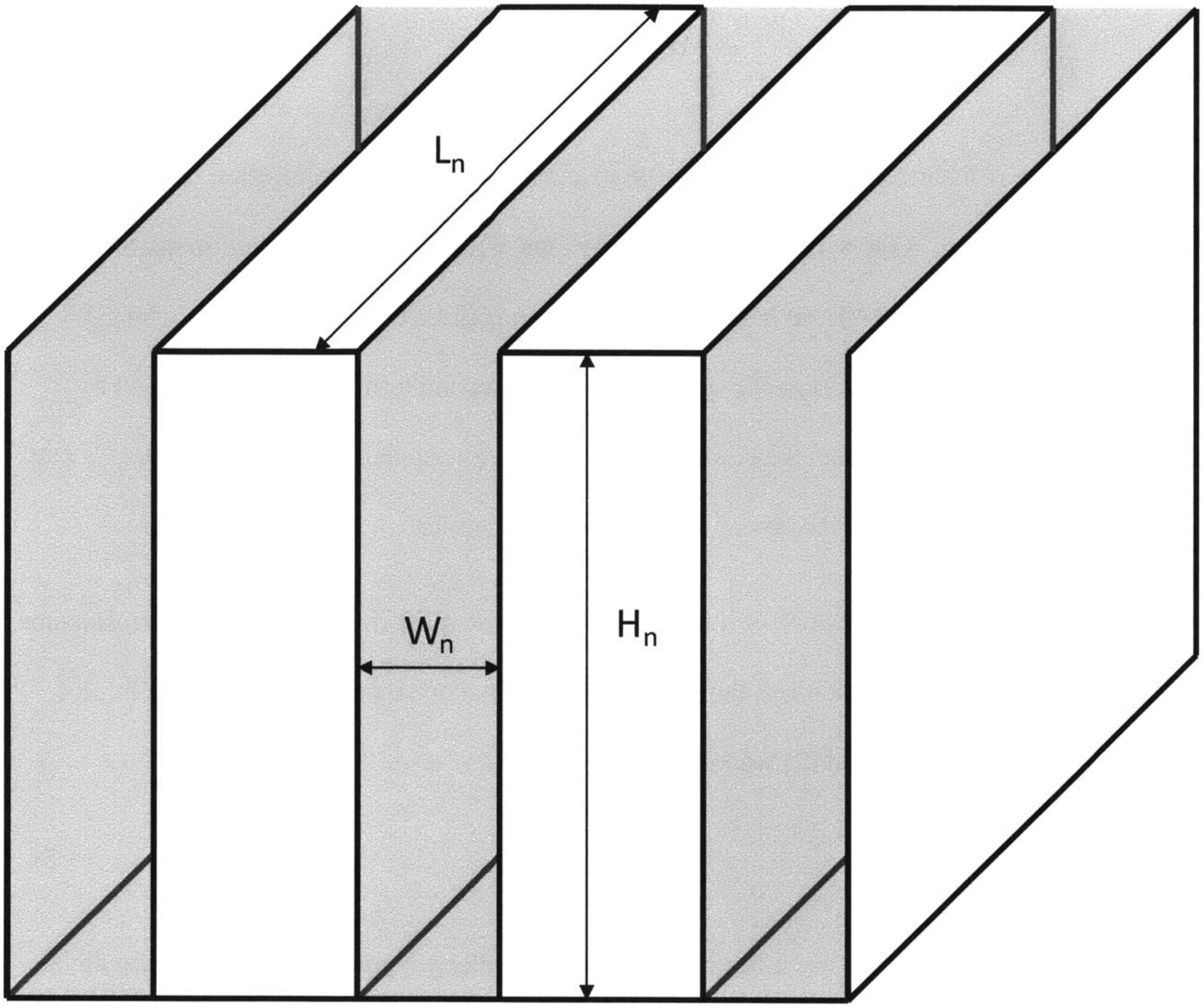

Figure 3-4 Schematic of three parallel nanochannels showing the convention used in defining the length (*L*), width (*W*), and height (*H*) of a nanochannel.

The resistance of an array of cuboid nanochannels is given by:

$$R_n = \frac{\rho L_n}{N H_n W_n} \tag{3.7}$$

where ρ is the resistivity of the electrolyte (KCl) solution and N is the number of nanochannels in the array. Solving for the channel width (W_n) gives:

$$W_n = \frac{2\rho L_n}{N H_n \left(R_{13} + R_{24} - R_{12} - R_{34}\right)} \tag{3.8}$$

Here R_{13}, R_{24}, R_{12}, and R_{34} are experimentally determined from the inverse of the slope of the *I-V* plot for each case. For the devices used in this work, $N = 10$, $L_n = 30$ μm, and $H_n = 15$ μm. The conductivities ($1/\rho$) of 200 mM, 1 M, and 3 M KCl solutions were measured using a conductivity probe (VWR) and found to be 25.01, 113.8, and 290.1 mS/cm, respectively. From the gap size (width, W_n) of a nanochannel, we can obtain the film thickness (k) inside the nanochannel, which is:

$$k = (W_0 - W_n)/2 \tag{3.9}$$

where W_0 is the gap size of the nanochannel before PEM coating. Here we assume that the ionic transport inside the hydrated multilayer is negligible compared to the ionic flux through the open portion of the nanochannel. This assumption is justified[99] since hydrated PEMs have conductivities of order 10^{-9} S/cm while our KCl electrolyte solutions have significantly higher conductivities of order 10^{-1} S/cm.

3.3 Results and Discussion

Polymer Coil Dimensions

An important consideration for deposition of polymer molecules within a nanofluidic channel is the size of the polymer coil in solution. One means of characterizing coil dimensions is the root mean square end-to-end distance, given in Equation (1.3). The upper bound for this quantity is the contour length, given in Equation (1.1), which is 150 nm for PAH and 85 nm for PSS. In contrast, the lower bound for this quantity is the unperturbed chain length for which $\alpha = 1$ (theta conditions). Using a characteristic ratio of 7.8[100] for PSS, the unperturbed RMS end-to-end distance is about 11 nm. Using a characteristic ratio of 6.6 from poly(1-butene)[101] for PAH, the unperturbed dimensions are 14 nm. For polyelectrolytes, the charged nature of the backbone leads to coil expansion due to long range electrostatic repulsion. The ionic strength therefore affects coil dimensions by screening these repulsive interactions. Borochov and Eisenberg measured the radius of gyration of 10^6 g/mol PSS at different salt concentrations and found that the radius of gyration was 51 nm at 0.1 M NaCl and 108 nm at 10^{-3} M NaCl.[102] These values correspond to RMS end-to-end distances of 33 nm at 0.1 M and 70 nm at 10^{-3} M for our lower molecular weight PSS. If we use the coil expansion factors implied by these values to estimate the dimensions for PAH coils, we find that the RMS end-to-end distances are approximately 40 nm at 0.1 M and 85 nm at 10^{-3} M.

Polyelectrolyte Multilayer Growth in Nanochannels

The assembly of PAH/PSS multilayers in open nanochannel arrays was investigated using SEM. Figure 3-5 is a cross-sectional view of a nanochannel array that was successfully coated with 40 bilayers of PAH/PSS at pH 4.0 and 0.1 M NaCl. The SEM image shows that good coating uniformity was achieved along the length of multiple channels. We found the quality of the coating to be sensitive to the deposition conditions. Optimal coatings were obtained when depositions were performed with pH-adjusted rinse solutions and the sample was not allowed to dry until deposition was complete. We also have evidence that surface treatment may play a part in improving the uniformity of the coating. In particular, we have found that pre-assembly sonication of the nanochannel array in surfactant (3% Micro-90, International Products Corp.) and acid solutions (1 M HCl) tends to give more uniform films.

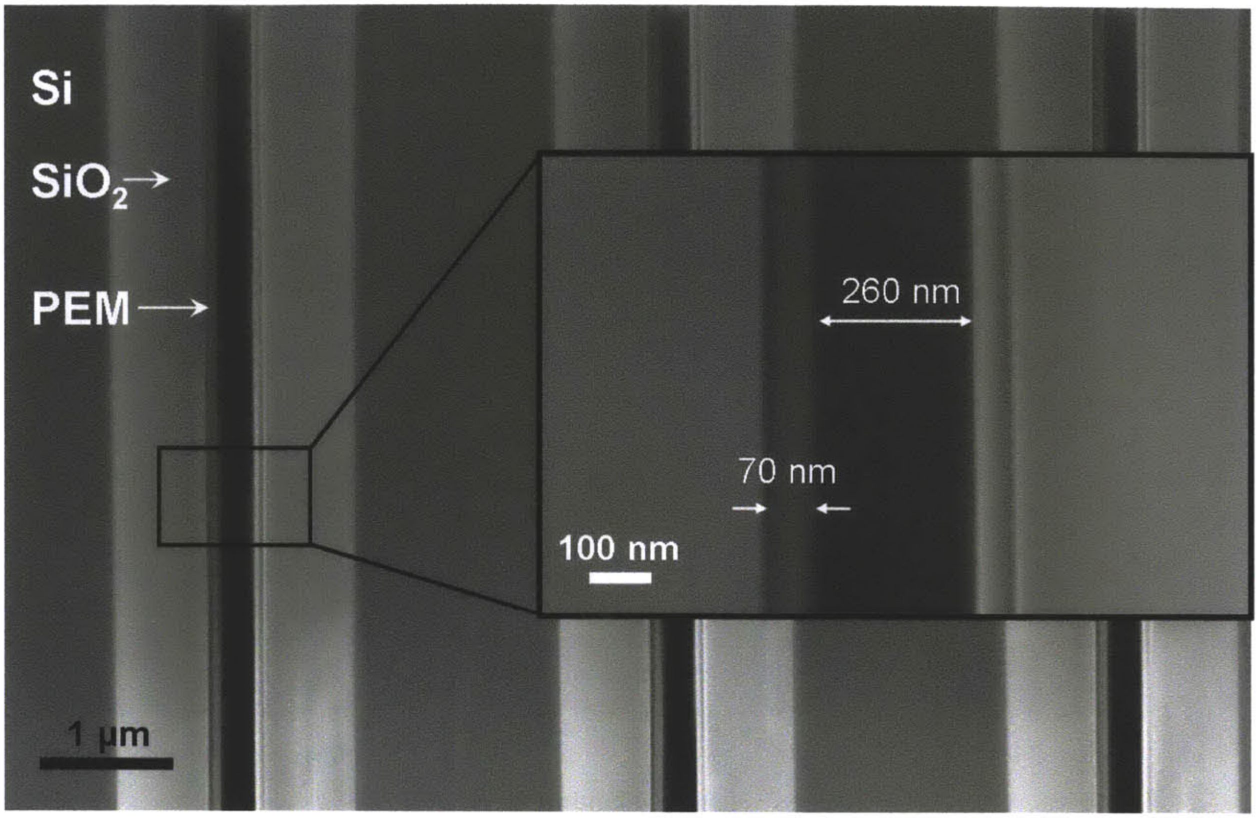

Figure 3-5 Scanning electron micrographs depicting conformal coating of an open nanochannel array with a 40 bilayer PEM of PAH/PSS deposited at pH 4.0 with 0.1 M added NaCl. The silicon, thermally-grown oxide layer, and PEM are clearly visible. The inset shows that the 400 nm channels have been reduced to a gap size of 260 nm by the LbL deposition of a 70 nm thick PEM.

To further quantify the coating uniformity, SEM micrographs of various regions of coated nanochannel arrays were analyzed to determine the PEM thickness. Samples coated with various numbers of bilayers of PAH/PSS assembled at pH 4.0 and 0.1 M NaCl were used to perform this analysis. The results are summarized in Figure 3-6. The data show that there is no systematic variation in the bilayer thickness with depth into the nanochannel, suggesting that deposition under these conditions is not limited by diffusion of the polyelectrolytes within the nanochannels.

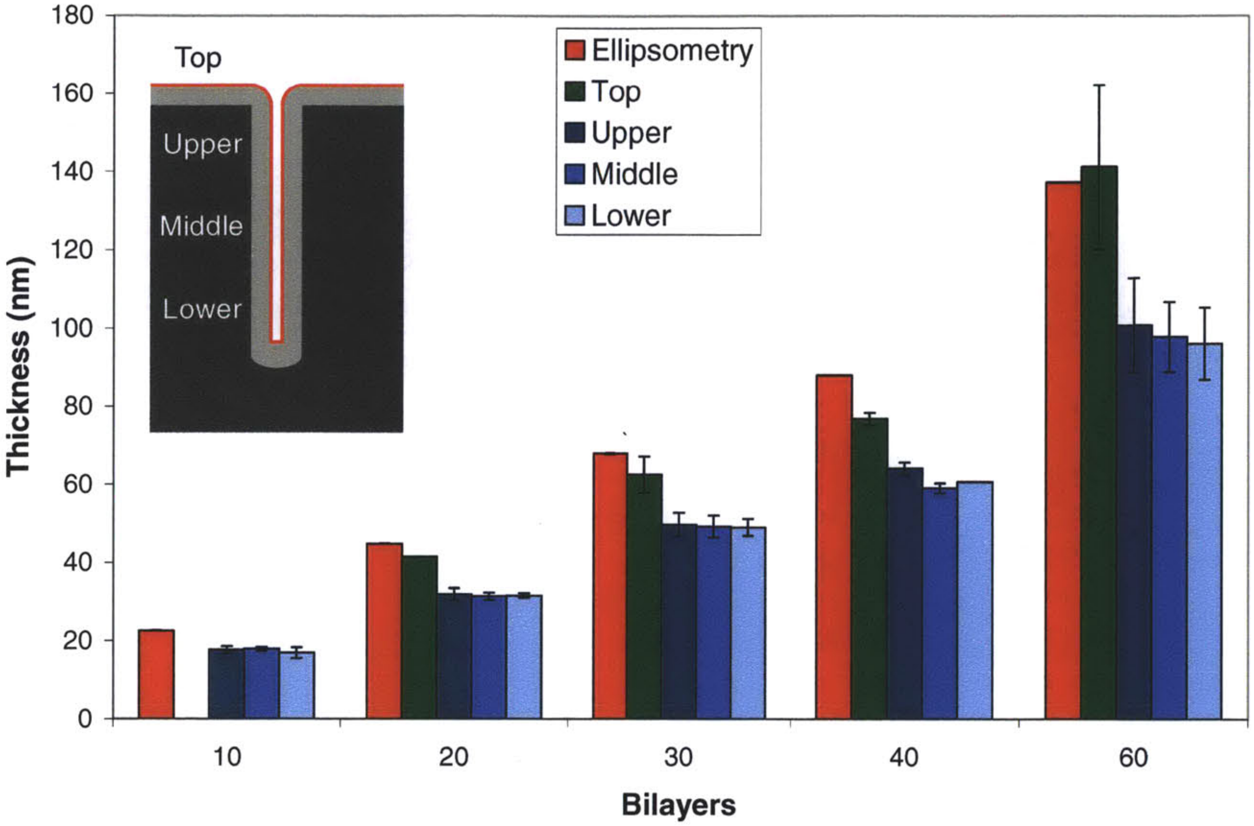

Figure 3-6 Comparison of dry state PEM thickness outside of and within a nanochannel for PAH/PSS multilayers deposited at pH 4.0 with 0.1 M added NaCl. The nanochannels had an initial gap size of 415 ± 41 nm. The red bars ("Ellipsometry") correspond to ellipsometry measurements on a flat silicon wafer. The green bars ("Top") correspond to SEM measurements of the unconfined PEM thickness on the top of the posts. The various blue bars ("Upper," "Middle," and "Lower") correspond to SEM measurements of the confined PEM thickness along the height of the nanochannel.

On the contrary, the data in Figure 3-6 do indicate a measurable difference between the multilayer thickness inside (upper, middle, lower) and outside (top) the nanochannel. The SEM measurements on the outside of the channels agree with ellipsometric characterization of dry PEMs on flat silicon control substrates which were coated using LbL under the same conditions as the nanochannel arrays. Various salt concentrations were also used in an attempt to determine how the bilayer thickness changes with increasing ionic strength in the polymer solutions used in the LbL assembly process. The data for 0.1 M and 0.25 M NaCl for both nanochannels and flat substrates are shown in Figure 3-7. The fitted slopes of these growth curves, which represent the bilayer thickness, are presented along with additional results for 0.5 M, 1 M NaCl, and for no added salt in Table 3-1. These data raise a few interesting points. First, both nanochannel and flat surface substrates show linear growth with all best fit lines going nearly through the origin. Second, the bilayer thickness in all cases is proportional to the square root of the ionic strength and is therefore inversely proportional to the Debye length (see plotted data in Figure 3-8) as observed by others.[69,103,104] Lastly, the data show that deposition within the nanochannels results in bilayer thicknesses similar to, but clearly lower than those obtained on flat surfaces. This result is contrary to previous reports where significantly larger[21,95] or significantly smaller[43] deposition thicknesses per cycle of processing were reported within confined geometries.

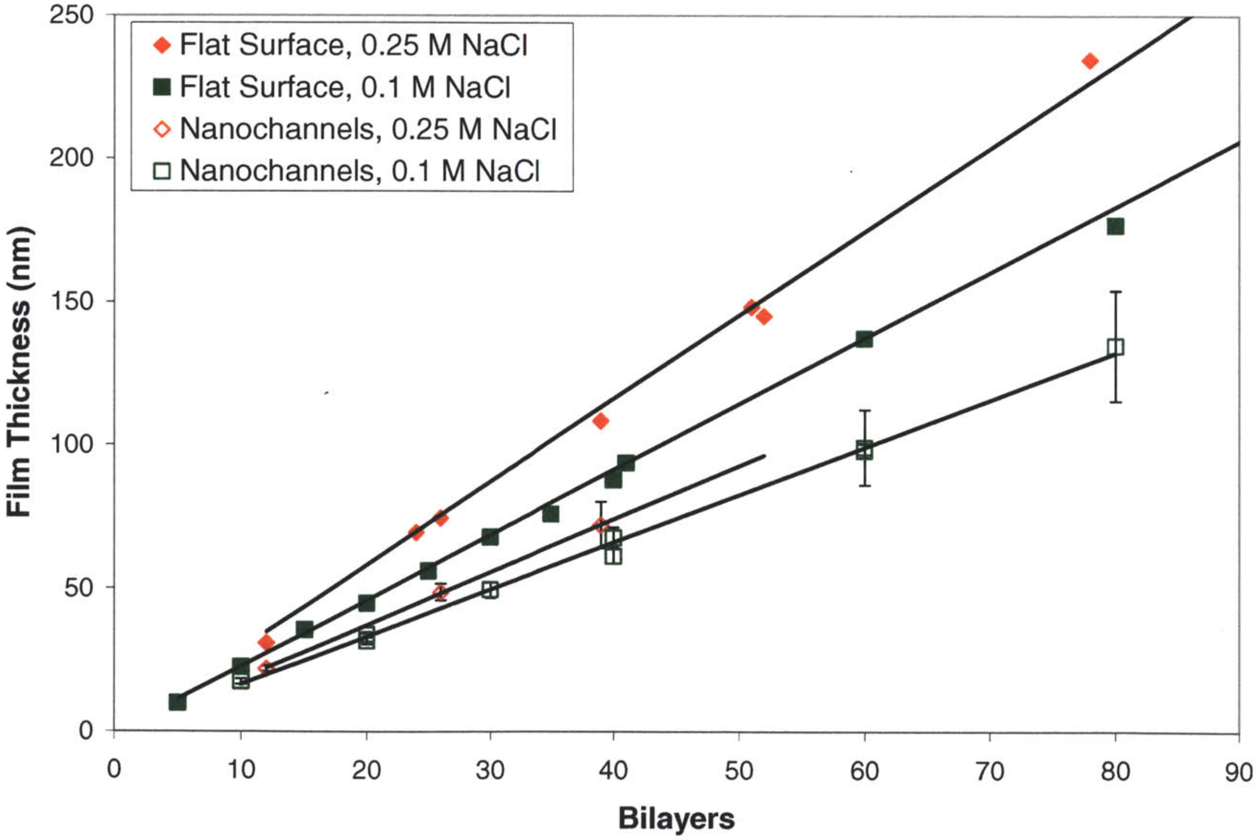

Figure 3-7 Comparison of dry state PEM thickness in channels and on a flat surface at different ionic strengths for PAH/PSS multilayers deposited at pH 4.0. The red diamonds and green squares represent ellipsometry measurements of film thickness on a flat surface for 0.25 M and 0.1 M respectively. The open diamonds and open squares are the corresponding SEM measurements of film thickness within the channels.

Table 3-1 Dry state bilayer thicknesses obtained by LbL assembly of PAH and PSS at various salt concentrations. The flat silicon substrate data are from spectroscopic ellipsometry measurements and the nanochannel data were obtained using SEM. The nanochannel bilayer thickness at 1.0 M NaCl is not included since these PEMs showed extreme roughness and poor film uniformity.

Salt Concentration (M)	Flat Surface Bilayer Thickness (nm)	Nanochannel Bilayer Thickness (nm)	Flat Surface to Nanochannel Thickness Ratio
0	0.576	0.313	1.84
0.1	2.31	1.69	1.38
0.25	2.94	1.86	1.58
0.5	3.78	2.76	1.37
1.0	5.14	-	-

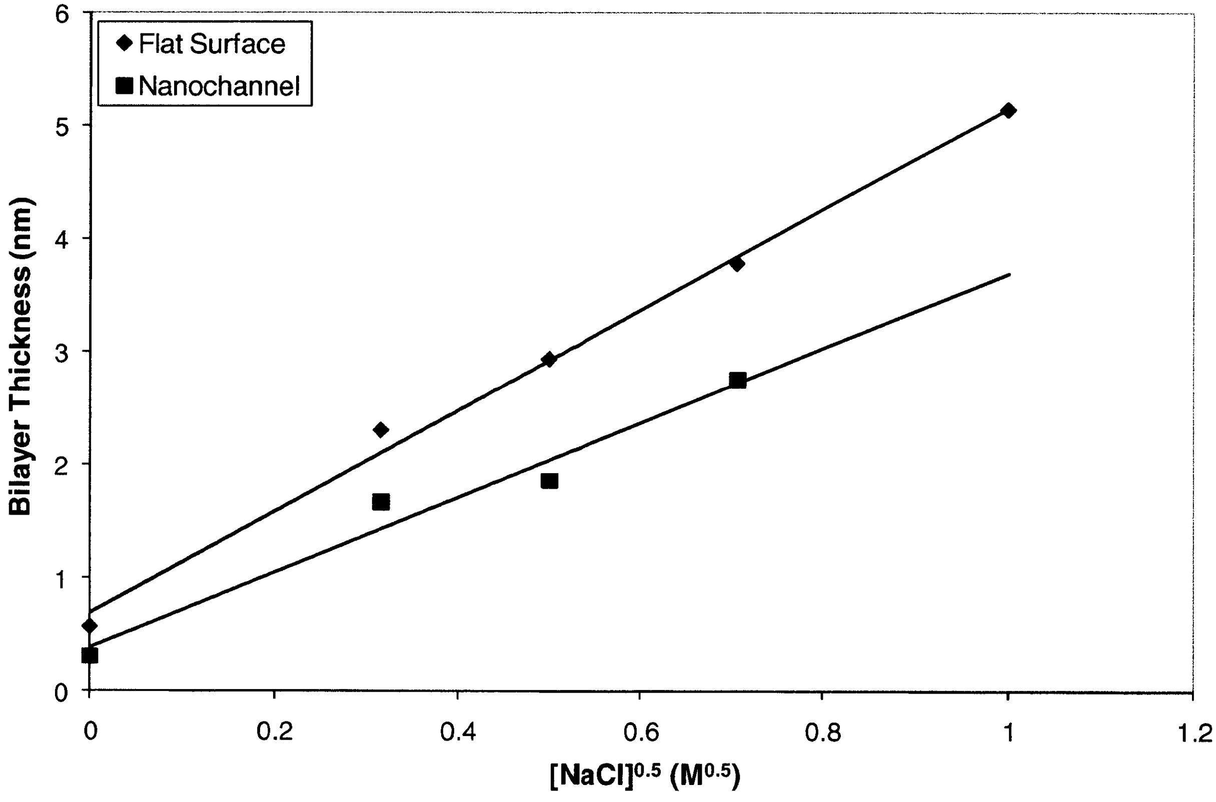

Figure 3-8 Plot of dry-state bilayer thickness measurements of a PAH/PSS multilayer assembled at pH 4 and varying salt concentrations on a silicon wafer (diamonds) and in a nanochannel (squares). The thickness varies with the square root of ionic strength as expected.

One explanation for the somewhat lower than expected bilayer thickness in the nanochannels is the depletion of unadsorbed polyelectrolyte within the channel. Depletion of polyelectrolytes confined between two charged surfaces has been predicted by Böhmer *et al.* using self consistent field simulations.[69] Suppose that we start with a negatively charged surface which is dipped into a polycation solution. In the planar case, the positively charged polymer molecules are readily adsorbed at the surface creating a concentration gradient and a resultant driving force which causes a higher flux of polycation molecules towards the surface. This continues until the surface charge reverses and increases to a point at which further adsorption is impossible due to electrostatic repulsion. In the nanochannel case, an additional step is added, namely diffusion of polymer molecules from the bulk into the confined channel. According to Böhmer *et al.*, for small gaps at low salt concentrations, which result in low charge screening, the adsorption of polyanions onto an initially positively charged surface results in a negative potential throughout the channel. This potential reduces the flux of polyanions into the channel, lowering the polyanion concentration within the channel thereby hindering further adsorption.[69] In contrast to the planar case, adsorption in this case is limited by transport into the channel, explaining our observation of somewhat thin, but uniform multilayers along the length of the channel. This surface charge-induced depletion effect is attenuated by the presence of ions in the solution due to electrostatic screening; thus at the elevated ionic strengths we have employed (the gap is about 250 times larger than the Debye length), we see fairly similar, though slightly lower bilayer thicknesses due to confinement. In the absence of added salt, we would expect to observe a more dramatic effect. In fact we observe that for PAH/PSS deposited at pH 4 without additional salt where the gap is only 8 times larger than the Debye length, the PEM thickness after 50 bilayers is only about 16 nm in a 230 nm channel. In contrast we measured a film thickness of

33 nm on a flat silicon surface. At these conditions, Böhmer *et al.* do predict significant depletion throughout the channel. Though not conclusive, due to the fact that the very low multilayer thicknesses involved make these measurements more sensitive to error, this result indicates that the discrepancy between confined and unconfined LbL assembly is more pronounced at lower salt concentrations as shown in the last column of Table 3-1. Additionally, Figure 3-6 also shows increasing discrepancy between film thickness outside and within the channel as the film thickness increases and the gap thickness decreases in agreement with this hypothesis.

It should be noted that the polyelectrolytes used in this study are polydisperse; similar polyelectrolytes have a polydispersity index of over 6.[105] As a result, coils significantly larger than the averages quoted above are involved and this could account for lower bilayer thicknesses within the channel. It has been established that although polyelectrolytes in extended configurations result in a film whose bilayer thickness is molecular weight-independent, those in coiled, loopy conformations such as we would expect in a solution of moderate ionic strength do show molecular weight-dependent bilayer thicknesses.[30] Thus if the top surface is in equilibrium with a higher average molecular weight ensemble than the confined surface due to the physical exclusion of high molecular weight polyelectrolytes, this may account for the thickness discrepancy. This effect may also be due to steric hindrance which starts to affect diffusion rates even for polymers whose radius of gyration is well below the size of a pore or channel.[82] In LbL, our aim is to approach equilibrium and the fact that we see uniform thickness along the channel wall suggests that deposition cycles are sufficiently long for polymer to diffuse into the channel. The effect of steric hindrance may also be mitigated by the fact that, as Deen pointed out, the dynamic nature of a polymer coil can result in diffusion through pores which are much smaller than the radius of gyration.[106]

The uniformity and conformality of the PEM coating allows us not only to functionalize the surface of the nanochannels, but also to tune the nanochannel gap size, reducing it uniformly and systematically to a desired value, which is crucial for nanofluidic applications. An important metric for this technique is how small and uniform a gap size can be obtained by assembling multilayers in the nanochannels. We have been able to reduce the gap size (open width of nanochannel) from 222 nm to 11 nm after deposition of 50 bilayers of PAH/PSS at pH 4.0. Protrusions and occasional bridging of polymer between the sidewalls of the nanochannel were sometimes observed when the dry state gap size (measured via SEM) was below 150 nm and when no salt was added. The frequency of observation of these defects increases as the gap size becomes smaller (see Figure 3-9). When these defects are present, most of the channel is unaffected so that the performance of a nanochannel device would be largely unaltered. We believe that this effect may be caused by incomplete rinsing or by contamination and that possible remedies include performing LbL assembly using a high-flow filtration process[87] instead of the diffusion-dependent dipping method.

Wet-State Film Thickness Measurement by DC Conductance

The DC conductance measurement was used to determine the wet-state thickness of a PEM film in a nanochannel as described in the experimental section. The high-aspect-ratio nanochannels have the advantage of high throughput (large open volume), but as a result the electrical resistance of the nanochannels is comparable to or even significantly smaller than that of the microchannels, especially for nanochannels with large gap sizes. This fact raises the potential for significant errors in calculating the nanochannel gap size using Equation (3.6). In order to improve the measurement resolution, we significantly reduced the resistance of the microchannels by employing large, pyramid-shaped microchannels, as shown in Figure 3-1a. The DC conductances of channel circuits (S_{13}, S_{24}, S_{12}, and S_{34}) were determined by fitting the slopes of the *I-V* curves. Figure 3-10 shows the swollen thickness of hydrated PAH/PSS multilayers deposited at pH 4.0 and a NaCl concentration of 0.1 M in nanochannels, calculated from conductance measurements using Equation (3.8), and on a flat surface measured by *in situ* ellipsometry as a function of the number of bilayers.

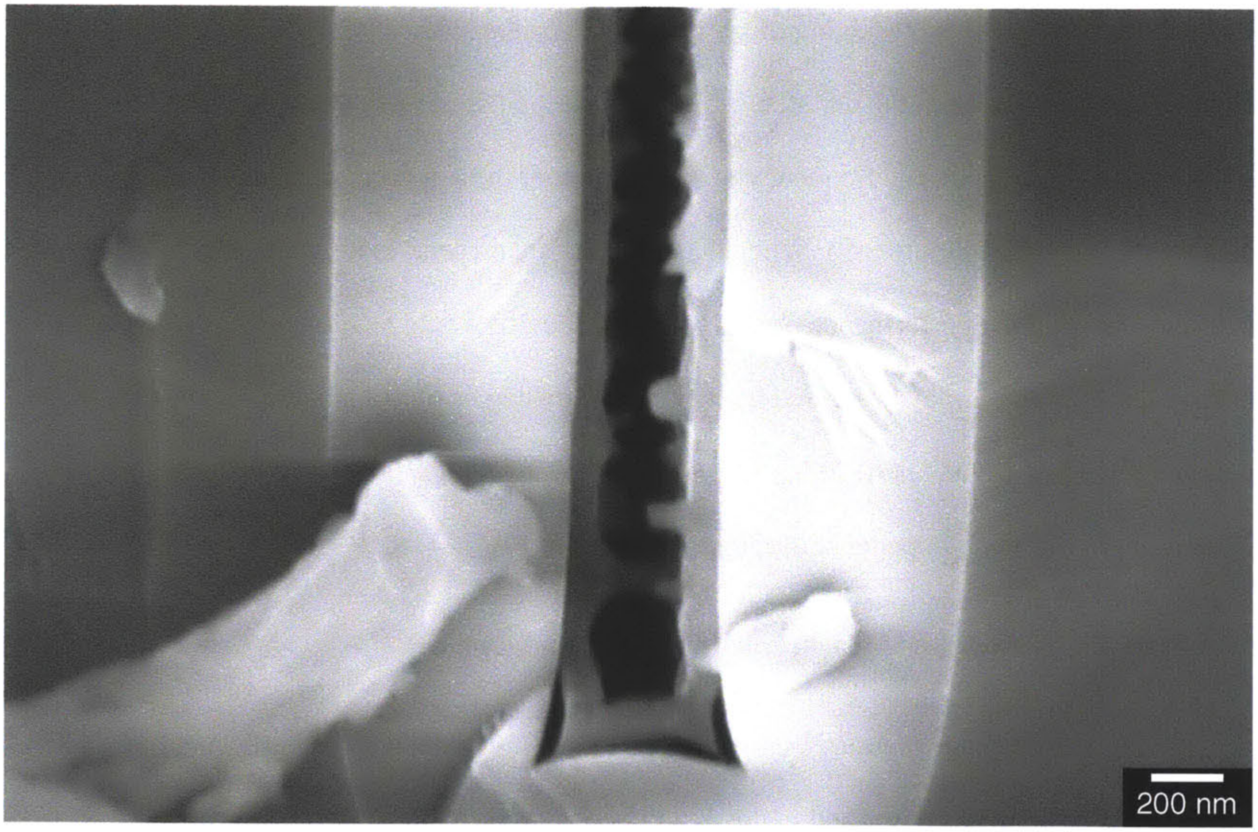

Figure 3-9 Scanning electron micrographs depicting the bridging effect observed in an open nanochannel array coated with a 70 bilayer PEM of PAH/PSS assembled at pH 4 and a salt concentration of 0.1 M NaCl.

First, we see that the DC conductance measurements were performed with 0.2 M, 1 M, and 3 M KCl. These experiments were used to further verify our assumption of bulk behavior and negligible surface charge effects on nanochannel conductance. Stein and coworkers studied surface-charge-governed transport in nanofluidic channels[98] and reported that at low salt concentrations, the electrical conductances of nanochannels saturated, becoming independent of both concentration and channel height. For 70 nm deep planar nanochannels, this transition occurred around 0.01 M;[98] therefore more concentrated electrolyte solutions were used in our experiments. As expected, the nanochannel conductance varied linearly with salt concentration in all cases (data not shown) and no significant differences were observed for the swollen thicknesses calculated from the measurements using the three different electrolyte solutions. These observations confirm the validity of our treatment of the PEM-coated nanochannels as idealized, inert channels at the high salt concentrations used here.

Second, it has been well-established that some polyelectrolyte multilayers can swell significantly when immersed in salt solution[23,107,108] (see Figure 3-2). Thus the wet-state thickness of a PEM film, which is measured by DC conductance, can vary significantly from its dry-state thickness, which is measured by SEM or ellipsometry. We used ellipsometry to measure both the dry state and wet state thicknesses of a PEM film on a flat silicon wafer. The percent (%) swelling of the multilayers deposited on a flat substrate, defined as (wet thickness - dry thickness) / dry thickness × 100%, was about 26%. This value agrees well with the value of 22% for PAH/PSS reported previously.[108]

Third, at high numbers of bilayer processing steps, the wet-state thickness of the LbL films on the nanochannel walls asymptotes to a constant value of about 105 nm at which point the gap size of the nanochannels is only about 11 nm. In Figure 3-11 we recast these data to show the dependence of the gap size on the number of deposited bilayers and compare them with our results for SEM (see Figure 3-12 for more complete SEM data). We can see that in both cases we observe a deviation from linearity at low gap size, at about 11 nm for the conductance measurement and at about 34 nm for SEM. It should be noted that since DC conductance is a measure of the wet state thickness and SEM is a measure of the dry state thickness, we would expect the SEM data to asymptote at a higher value. These values are on the same length scale as the radius of gyration of the polyelectrolytes, and thus we would expect to see size-based exclusion of the polymer molecules, resulting in a failure to sustain LbL assembly within the channels.

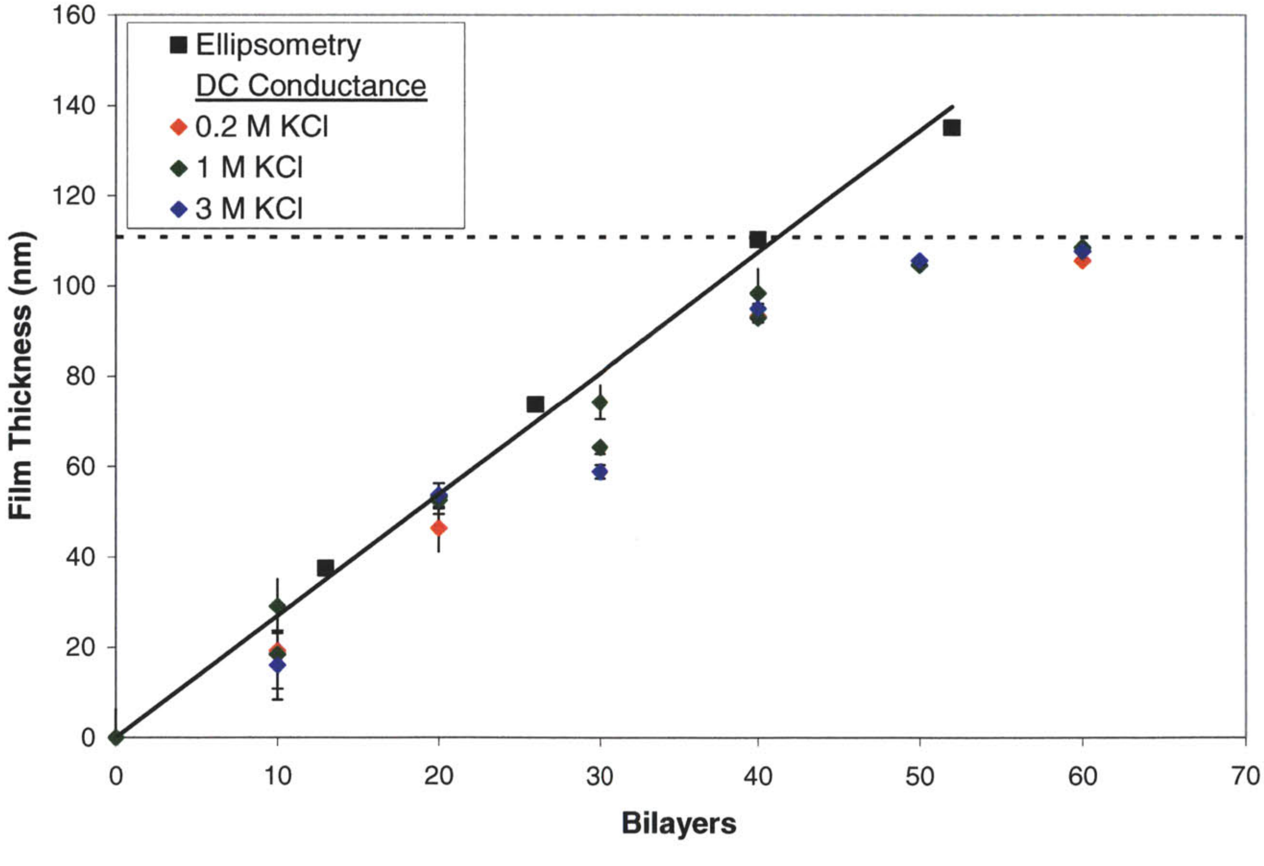

Figure 3-10 Comparison of wet state PAH/PSS (pH 4.0, 0.1 M NaCl) multilayer thickness measurements obtained by two different methods: measured on a flat silicon surface under 1 M KCl using ellipsometry (black squares) and calculated from DC conductance measurements using 0.2 M KCl (red diamonds), 1 M KCl (green diamonds), and 3 M KCl (blue diamonds) as the electrolyte. The dashed line represents the maximum possible film thickness within the nanochannel.

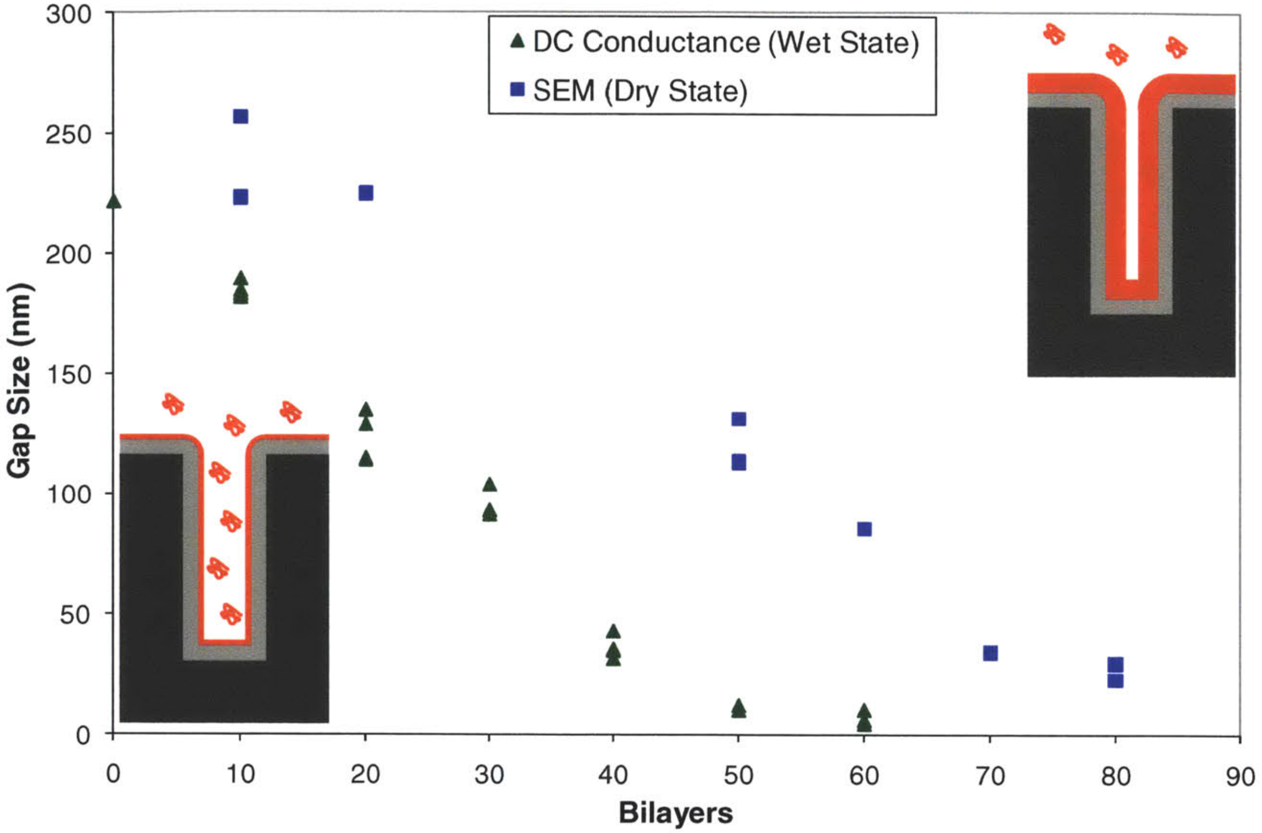

Figure 3-11 Nanochannel gap size as a function of the amount of PAH/PSS deposited at pH 4.0 and 0.1 M NaCl measured using two different methods: DC conductance (green triangles) and SEM (blue squares). Note that DC conductance is a measure of wet state thickness while SEM is a measure of dry state thickness. The initial gap thickness for the DC conductance device was about 220 nm while the open arrays used for SEM had initial gap thicknesses ranging from 300 to 325 nm.

The more complete gap thickness data set plotted in Figure 3-12 shows that for most of our SEM experiments we observed linear growth because our initial gap thickness was large enough that the deposited PEM never narrowed the channel enough to result in size-based exclusion of polyelectrolyte chains. As a result, we have a family of curves with similar slopes, but different intercepts. The exception is the smallest (300-325 nm) channels which do show a plateau in the narrowing of the gap size at a dry state gap size of around 34 nm.

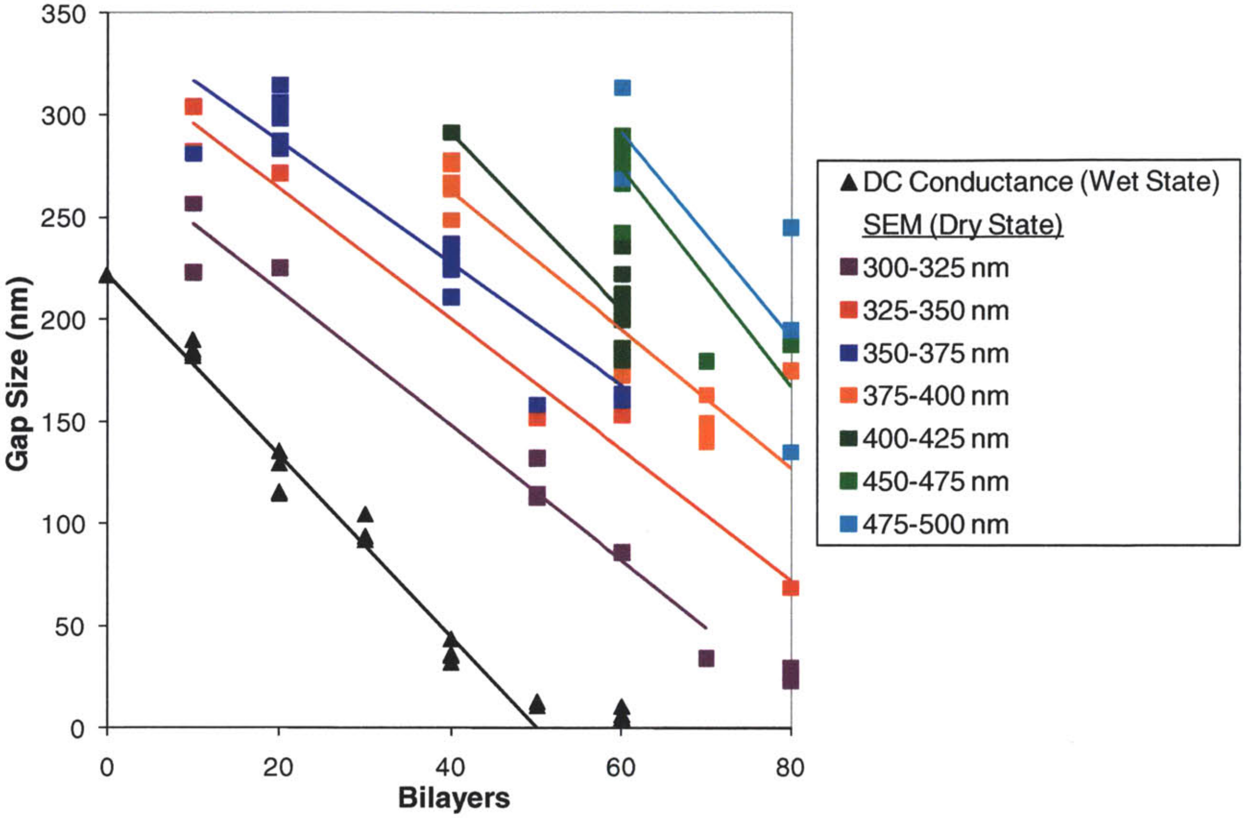

Figure 3-12 Plot showing nanochannel gap size as a function of the amount of PAH/PSS deposited at pH 4.0 and 0.1 M NaCl measured using two different methods: DC conductance (black triangles) and SEM (colored squares). The different colors correspond to different initial gap thicknesses as indicated in the legend.

Lastly, we can see that the DC conductance-derived data in Figure 3-10 compare favorably with the *in situ* ellipsometry measurements performed with 1 M KCl and, like the SEM data, show slightly lower bilayer thicknesses. The data were not directly compared with the SEM data due to the fact that SEM data were always taken in the dry state while conductance data were always taken in the wet state. The wet state results show that electrical resistance measurements are an efficient, nondestructive alternative for measuring the channel gap thickness in PEM-coated nanochannel arrays.

To directly compare the wet state DC conductance results with the dry state SEM observations and to allow for the fact that a range of channel widths were used, the data were normalized. This was done so that the y-axis represents the film thickness divided by the film thickness which results in a completely filled nanochannel and the x-axis represents the number of bilayers divided by the number of bilayers required to completely fill the channel. The y-axis is given by:

$$k^* = \frac{2k}{W_0} \tag{3.10}$$

where k^* is the normalized film thickness, k is the film thickness, and W_0 is the width of the uncoated nanochannel. The x-axis is given by:

$$b^* = \frac{2bm}{W_0} \tag{3.11}$$

where b^* is the normalized number of bilayers, b is the number of bilayers, and m is the bilayer thickness *i.e.* the slope of the growth curve in Figure 3-2. The SEM data were normalized using the dry-state bilayer thickness and the DC conductance data were normalized using the wet-state bilayer thickness. Since the normalization constant comes from the slope of the growth curve determined from ellipsometry, the ellipsometry results are represented by a solid line of slope 1. Figure 3-13 shows the resulting plot. From the data we can see that both the DC conductance and SEM data sets are in rough agreement and in general, lie below the line representing the flat surface, indicating slower growth within the nanochannels. We also see that as the fraction of the channel filled increases, the thickness values deviate further from the flat surface result, indicating slower growth due to confinement. If we continue trying to assemble past the point at which the channel should already be full, the curve plateaus to a constant value less than 1 due to size-based exclusion of polymer molecules.

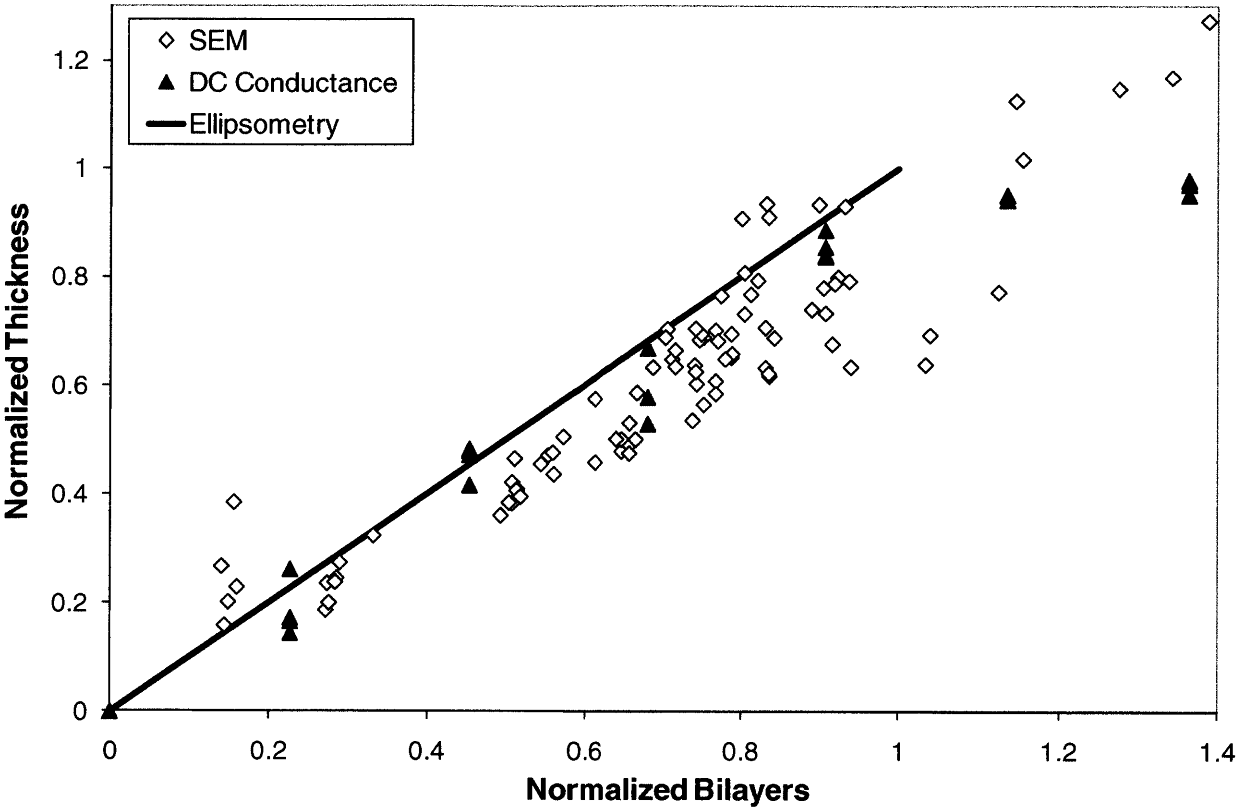

Figure 3-13 Plot showing normalized film thickness as a function of a normalized bilayer number. The solid line represents the results for a flat surface obtained via ellipsometry (wet and dry state), open diamonds represent thickness measurements observed via SEM (dry state), and filled triangles represent thickness measurements calculated from DC conductance data (wet state).

3.4 Conclusions

In this work we have conformally coated high aspect ratio nanofluidic devices using LbL assembly of PAH and PSS. This procedure has been used to systematically narrow the wet-state nanochannel gap from 222 nm down to about 11 nm, at which point further LbL processing does not lead to any appreciable narrowing of the gap for the PAH/PSS polyelectrolyte pair used in this study. The deposited film thickness in the nanochannel did not show any significant depth dependence, demonstrating that this technique is suitable for building hybrid nanofluidic systems. We have shown that prior to the onset of size-based exclusion that occurs for very small gaps, the bilayer thicknesses are lower than those obtained for a flat surface. The magnitude of this effect is more pronounced at lower salt concentrations, but is always less than a factor of two. This phenomenon was rationalized by the charge-based exclusion of polyelectrolytes between two closely spaced charged surfaces. Simple conductivity measurements were developed to calculate the gap thickness of nanochannels embedded within a microfluidic device. These conductivity measurements have been validated by comparison with SEM and ellipsometry results, and at the high ionic strengths used in this study the results are independent of the KCl electrolyte concentration.

The results obtained here point toward experiments to investigate in more detail how the confined bilayer thickness depends on the nature of the materials being deposited as well as the ionic strength of the LbL assembly solutions and the coated nanochannel gap thickness. Of particular interest is the question of whether or not charged nanoparticles can be deposited in a controlled manner using the nanochannel-confined LbL assembly process described above. A detailed study of polymer/nanoparticle and all nanoparticle systems is presented in the following chapters.

Chapter 4 Layer-by-Layer Deposition of Nanoparticle-Containing Multilayers in Confined Geometries

Reproduced in part with permission from Kim, J. Y.; DeRocher, J. P.; Mao, P.; Han, J.; Cohen, R. E.; Rubner, M. F. Formation of Nanoparticle-Containing Multilayers in Nanochannels via Layer-by-Layer Assembly. *Chem. Mater.* **2010**, *22*, 6409-6415. Copyright 2010 American Chemical Society.

4.1 Introduction

Recently, nanofluidic devices comprised of channels with at least one nanoscale dimension have attracted growing interest due to their high throughput, small volume of reactants, and fast kinetics.[83,109,110] To achieve high efficiency, good repeatability, and multiple functionality in these devices, several strategies for functionalization of the channel surfaces have be implemented including physical adsorption, dynamic coating, and permanent surface modification by covalent linkage or crosslinking.[111-115] Another promising technique is the use of LbL assembly to fabricate multilayer films by alternate deposition of oppositely charged species. LbL assembly is a simple and versatile approach for the fabrication of molecular assemblies of tailored architectures with multiple functionalities, allowing precise control of the thickness, composition, and physical/chemical properties of multilayered composite films on the nanoscale level.[37,116,117]

Previous papers from our laboratory and others have reported successful LbL assembly of charged macromolecules in confined geometries.[21,24,26,41,43,86-88,93,118,119] Conformal, ionically cross-linked, polymeric coatings with attractive features such as dimensional responsiveness to pH changes and adjustable surface charge and surface chemistry have been produced on the inner walls of templates with submicron geometric features. Successful LbL processing was achieved even when one of the characteristic dimensions of the coated template decreased to the same order of magnitude as the macromolecular coil dimensions, *i.e.* in the regime of tens of nanometers.

Here we extend these previous studies to include LbL assembly of charged nanoparticles in confined geometries. We have studied various oppositely charged polymer-nanoparticle pairs, and we report on two specific systems that demonstrate the issues and opportunities that arise in confined geometry LbL assembly: positively charged TiO_2 nanoparticles partnered with poly(vinylsulfonic acid) (PVS) and PDAC partnered with negatively charged SiO_2 nanoparticles. The latter system was first studied in detail by Lvov *et al.*[54] The selection of Si/SiO_2 nanochannel templates[59] provides the opportunity to use high-temperature calcination[18] to remove the organic material from the LbL film, leaving a nanoporous inorganic layer of adjustable thickness on the walls of the template. Such nanoporous coatings add a new dimensional element to the functionalization of nanochannel arrays and may allow the implementation of nanoscale selective permeation effects similar to those exploited in size exclusion chromatography. Figure 4-1 provides a schematic summary of this approach.

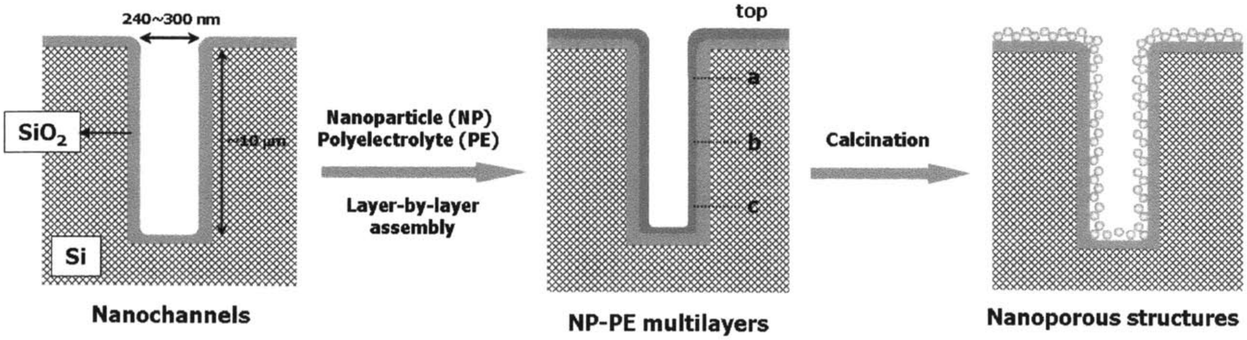

Figure 4-1 Schematic drawing of LbL assembly of nanoporous coatings within a nanochannel. Nanoparticle-containing multilayers are assembled in nanochannels via sequential deposition of charged nanoparticles and polyelectrolytes. Subsequent calcination of the precursor film results in the formation of nanoporous structures in the nanochannels. Nanoparticle-containing multilayers deposited in nanochannels show uniform thickness distribution over the (a) upper, (b) middle, and (c) lower parts of the nanochannels. Courtesy of Dr. Jun Young Kim.

4.2 Experimental Section

High aspect ratio nanochannel arrays were fabricated according to procedures described in detail in Section 2.1. The long rectangular trenches varied in initial width from about 240-300 nm, with depths of about 10 μm. Silicon wafers (WaferNet, Inc.) were used as control planar substrates. PVS (25 wt% solution in water, $M_w = 4000\text{-}5000$ g/mol), PAH ($M_w =$ 56 000 g/mol), and PDAC (35% solution in water, $M_w \approx 10\,000$ g/mol) were purchased from Sigma-Aldrich (St. Louis, MO) and used as received. TiO_2 nanoparticles (mean particle size *ca.* 6 nm) were synthesized and characterized according to procedures described elsewhere.[120] SiO_2 nanoparticles (Ludox® HS-40, average particle size *ca.* 15 nm) were purchased from Sigma-Aldrich (St. Louis, MO). Deionized water (18.2 MΩ·cm, Millipore Milli-Q) was used in all aqueous solutions and rinse baths. Each solution was adjusted to the desired pH value with nitric acid for TiO_2/PVS and with hydrochloric acid or sodium hydroxide for PDAC/SiO_2. The concentrations of nanoparticles and polyelectrolytes in the dipping solutions were 0.015 wt% and 0.01 M (repeat unit basis), respectively.

Substrates were cleaned by three 10 min sonication steps in a detergent solution (3% Micro-90R, International Products Corp.), 1 M hydrochloric acid, and deionized water. After thorough rinsing with deionized water the cleaned substrates were blow-dried with compressed air. Not adhering to these cleaning steps led to non-uniform multilayers and aggregation/blockage in the nanochannels. LbL processing was performed using a StratoSequence VI spin dipper (nanoStrata, Inc.). The dipping time in each solution was 15 min followed by three intermediate rinsing steps (3, 2 and 1 min) in pH adjusted deionized water. In all cases the substrates were spun at 120 rpm. Multilayers of PVS/TiO_2 were assembled at pH 1.5 whereas PDAC/SiO_2 multilayers were assembled at pH 9.0

Calcination was performed at 550 °C for 2 h using a Barnstead Thermolyne 47900 furnace to remove organic polymer. Upon completion of the calcination process, the furnace was shut off and the coated nanochannel arrays were allowed to cool in the oven until ambient temperature was reached. The thicknesses of nanoparticle-polymer films and of calcinated nanoparticle films on flat silicon substrates were measured using spectroscopic ellipsometry (XLS-100, J. A. Woollam Co., Inc.) according to procedures described in detail elsewhere.[17,48] High resolution SEM was used to measure the thicknesses of multilayers deposited in the nanochannels and on the unconfined top surfaces of the nanochannel arrays. SEM micrographs were obtained using a JEOL 6320 operated at an accelerating voltage of 5 kV.

4.3 Results and Discussion

The TiO_2/PVS System

Herein we describe the fabrication of nanochannels functionalized with conformal, uniform TiO_2/PVS multilayers via electrostatic LbL assembly and nanoporous titania films formed by subsequent calcination. TiO_2/PVS multilayers assembled on flat substrates exhibit uniform deposition and linear thickness growth with the number of deposited bilayers. The average bilayer thickness on flat substrates (*ca.* 3.07 nm/bilayer) was smaller than the size of TiO_2 nanoparticles used, which can be explained by isolated domain growth.[52] To compare confined and unconfined deposition, SEM was used to measure film thicknesses on the top of the "posts" and within the nanochannels. In Figure 4-2 we see a nanochannel array which has a 60 bilayer TiO_2/PVS multilayer deposited on it. This micrograph shows conformal coating of the entire channel and remarkable uniformity throughout the depth of each channel. The inset provides a magnified view of the assembled multilayer and highlights its excellent uniformity. One can also start to see a discrepancy between the thickness of the multilayer inside the channel and that on top of the "posts."

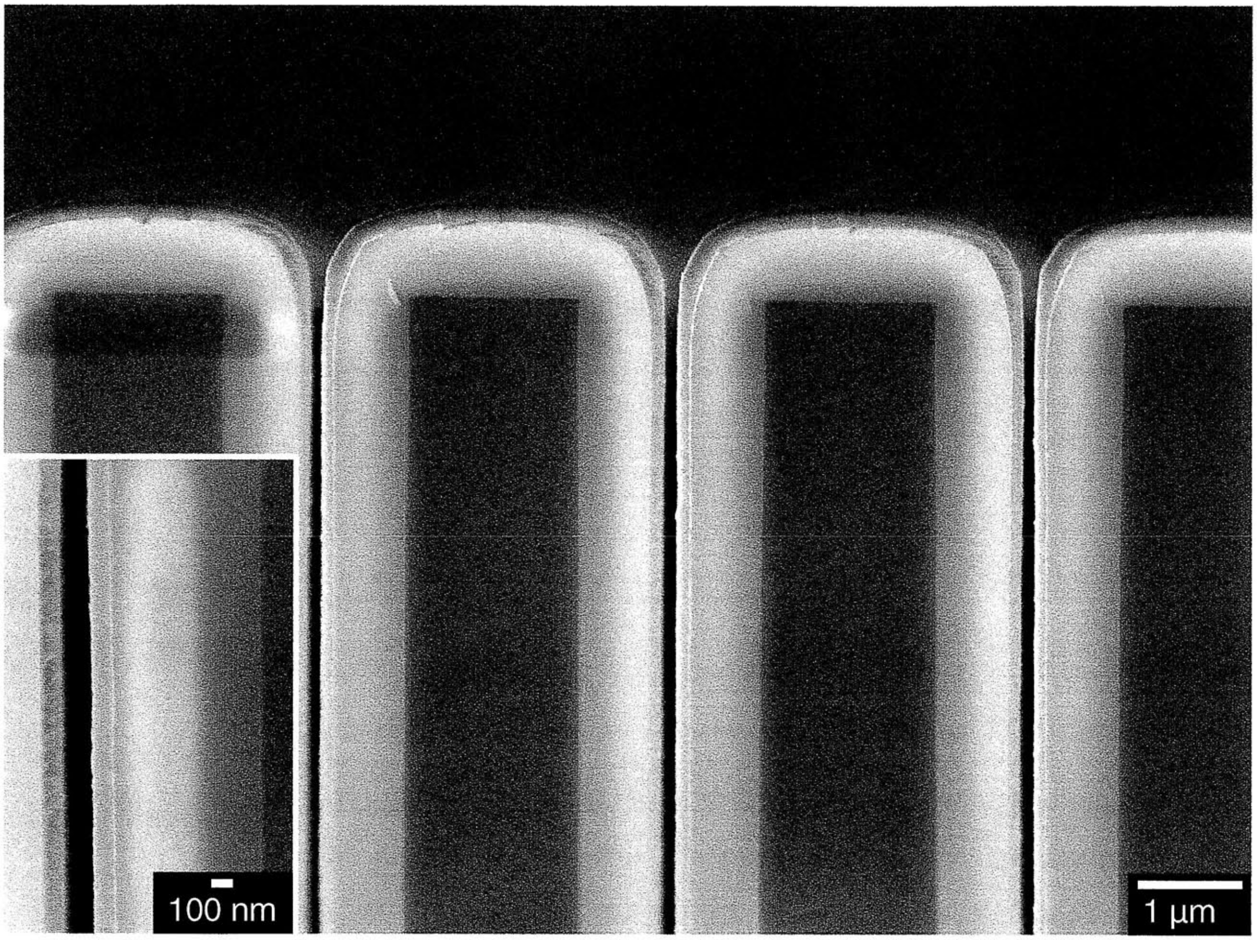

Figure 4-2 Cross-sectional SEM micrographs of the nanochannels coated with 60 bilayers of TiO_2/PVS showing uniform coating throughout the nanochannel. Courtesy of Dr. Jun Young Kim.

Further deposition magnifies this effect. In Figure 4-3 a 120 bilayer film of TiO_2/PVS has been assembled onto a nanochannel array. Once again, the film conformally coats the entire channel and is uniform throughout. Although the confined film looks fairly similar to the 60 bilayer case, the unconfined film has grown significantly, providing clear visual evidence of the difference in multilayer growth on the top and in the channels of the templates. In fact, the film on top of the "posts" is over three times thicker than that within the channels, yet no bridging or clogging of the channel is observed. The coated channel gaps remain open throughout the assembly process and the films on the channel walls are of uniform thickness from the top to the bottom of the 10 μm deep channels. These observations suggest that TiO_2 nanoparticle aggregation is not a significant problem under the conditions specified.

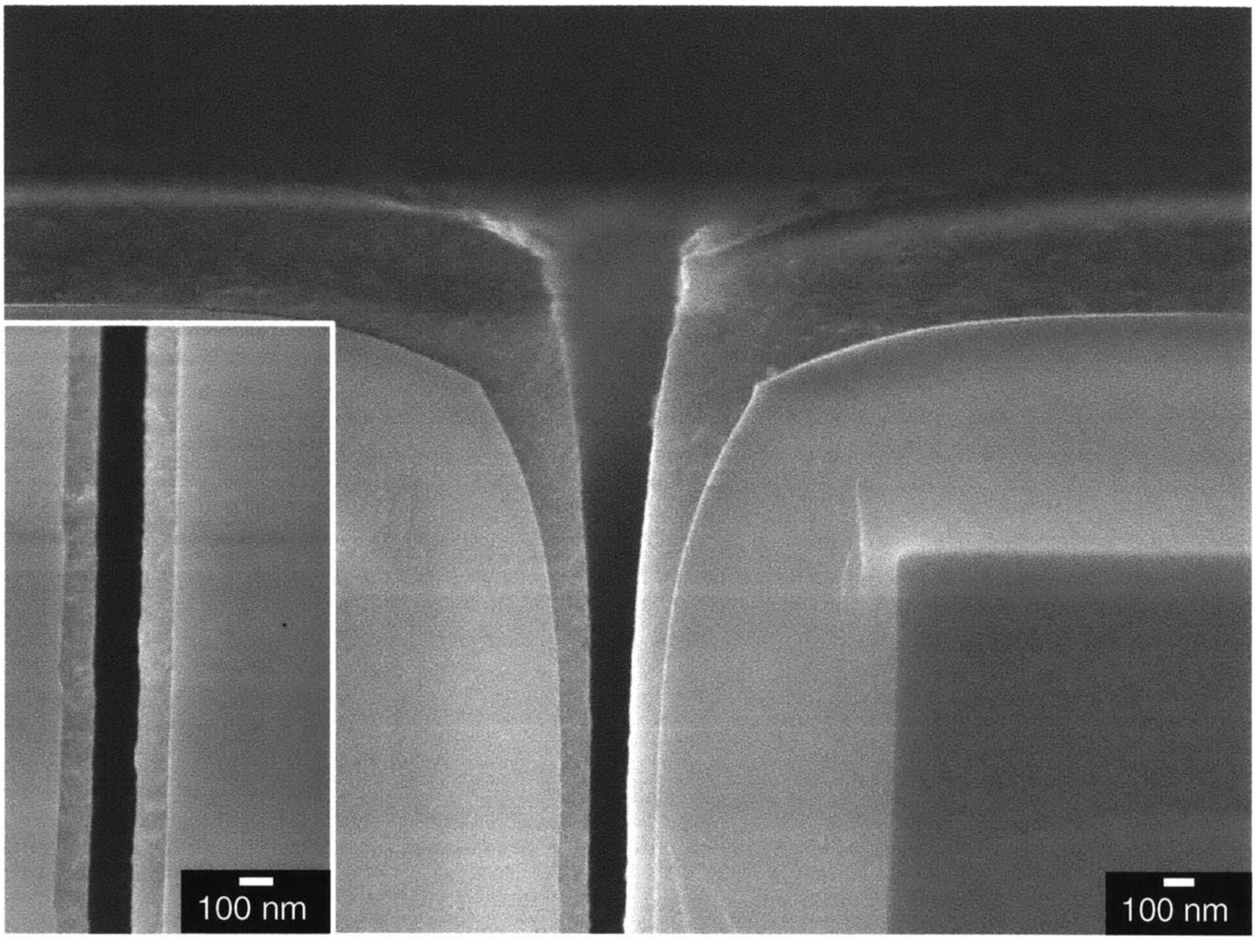

Figure 4-3 Cross-sectional view of nanochannels coated with 120 bilayers of TiO_2/PVS. The inset shows a magnified view of the uniform, conformal multilayer within the nanochannel. Courtesy of Dr. Jun Young Kim.

Some of these films were also calcinated to remove the polyelectrolyte component of the film, leaving only a nanoporous titania coating. A micrograph of a nanochannel array coated with 90 bilayers of TiO_2/PVS and calcinated for 2 h is shown in Figure 4-4. The inset shows a magnified, angled view of the surface. The roughness of the films on the channel walls is similar to what is seen for films assembled in the absence of geometric constraint. These micrographs prove that high temperature calcination leads to conformally adherent nanoporous titania coatings on the walls of the channels with no visible defects, indicating that calcination does not damage the film or the underlying template.

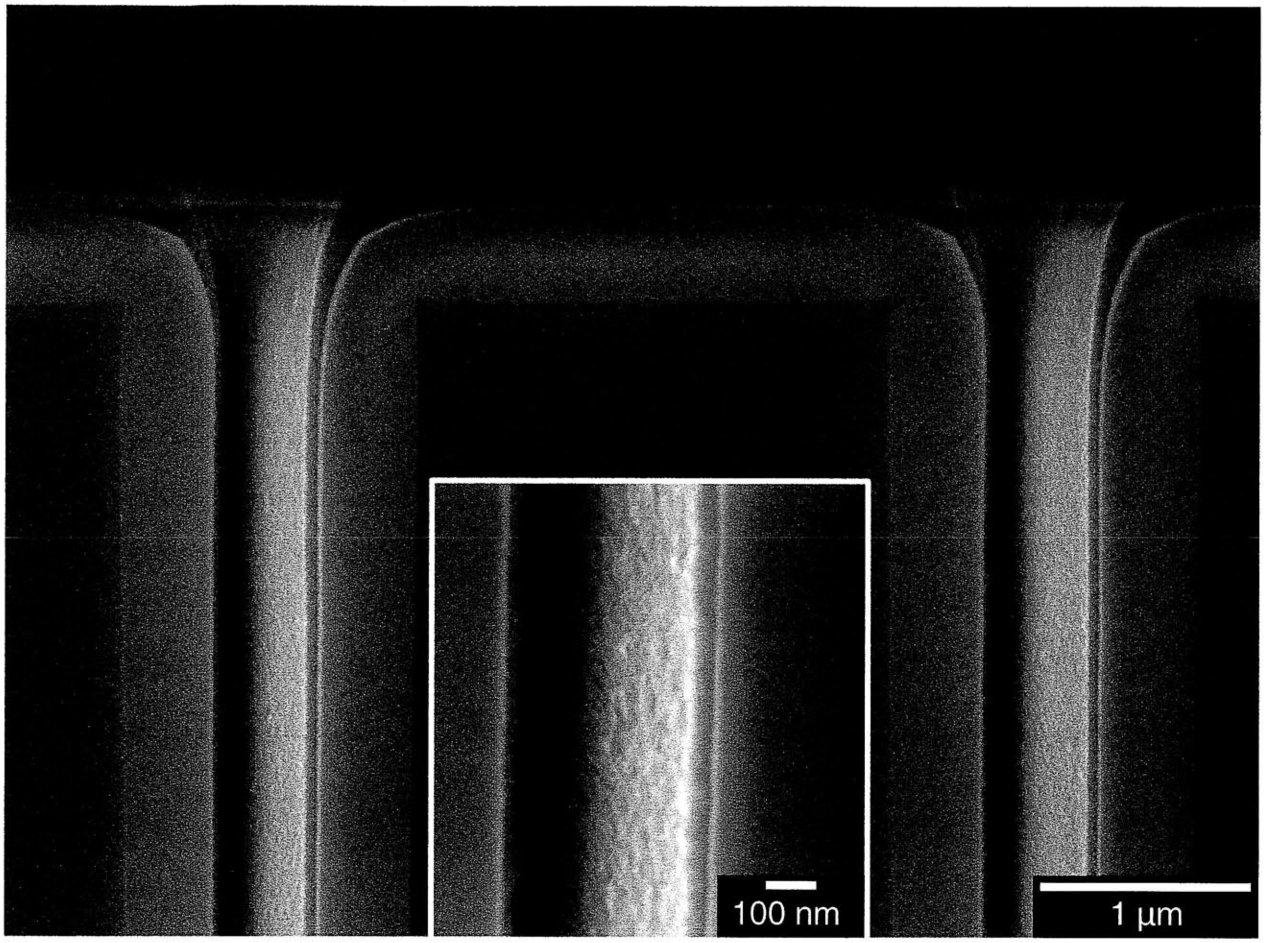

Figure 4-4 SEM micrograph of the nanochannels coated with a 90 bilayer TiO_2/PVS multilayer after calcination. Inset: highly magnified view showing a nanoporous titania film on a nanochannel wall. Courtesy of Dr. Jun Young Kim.

These micrographs and others were used to produce growth curves for both confined and unconfined TiO_2/PVS multilayers immediately after assembly and after subsequent calcination. Figure 4-5 confirms that LbL assembly of TiO_2 and PVS proceeds very differently on the top surface of the nanochannel template compared to the channels themselves. On the top surface, linear growth of the multilayer film persists up to 150 bilayers (~430 nm). The average bilayer thicknesses on the top surface are 2.66 nm/bilayer as-assembled and 2.42 nm/bilayer after calcination.

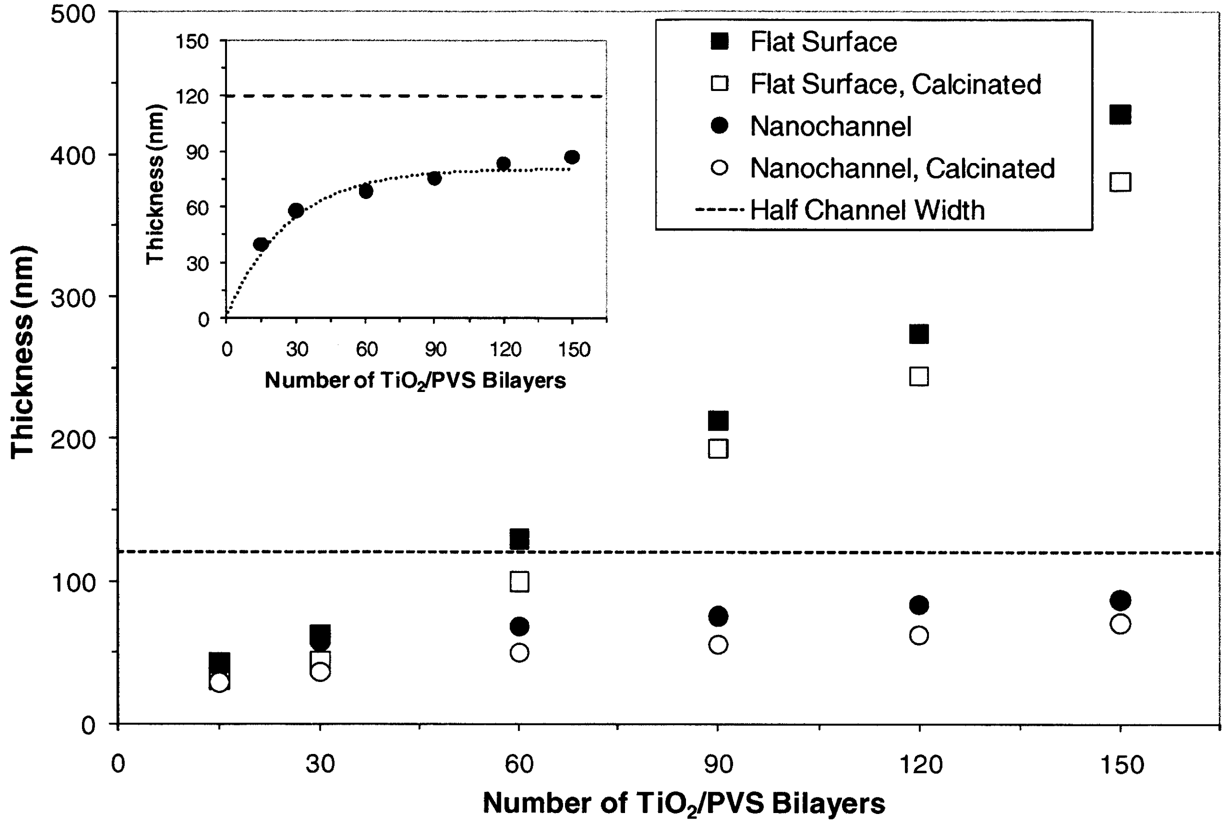

Figure 4-5 Thickness of TiO_2/PVS multilayers deposited at pH 1.5 with no added salt on the top surface (squares) and nanochannel walls (circles) as a function of the number of deposited TiO_2/PVS bilayers. Filled and open symbols represent the thickness of as-assembled and calcinated films, respectively. The inset is a magnified view of the data showing growth within the nanochannel. The dotted line is a best fit exponential decay curve, $k = k_0[1 - \exp(-b/b_0)]$. The parameters obtained from the best fit are k_0 = 80.7 nm and b_0 = 26.7 bilayers. The dashed line represents the half width of the channel and therefore the maximum film thickness.

The growth behavior of TiO_2/PVS multilayers assembled on the nanochannel walls is shown in detail in the inset of Figure 4-5. The coating thickness increased rapidly at first, and then exhibited lower thickness increments as deposition progressed. The thickness of the TiO_2/PVS multilayers on the nanochannel walls was not directly proportional to the number of deposited bilayers, indicating complex, nonlinear growth. The data can be described by an inverted exponential decay with a correlation factor of greater than 0.98 as shown in Figure 4-5. These data suggest an ultimate film thickness of 81 nm. The final gap thickness is given by $f = f_0 - 2k$

where f_0 is the initial gap thickness and k is the film thickness on each side. According to this formula, the limiting film thickness above corresponds to a final gap thickness of about 79 nm since the initial gap was approximately 240 nm. In addition, the decay constants are characteristic of the point at which nonlinear growth begins to dominate and the growth of the LbL film slows noticeably in the nanochannels compared to the behavior on the top surface. The half width of the channel is also plotted as this is the maximum thickness possible in the confined case. The distance between this line and the growth curve comprises half the gap size.

This general phenomenon, smaller bilayer thickness in the channels, was also observed in our earlier work[118] that involved all-polymer assembly, but it is much more pronounced in the present case. We have proposed two mechanisms for the lower growth rate in the channels: surface charge-induced depletion of unadsorbed polyelectrolytes in the channels and steric rejection of the highest molecular weight fraction of the polydisperse macromolecules employed in the LbL assembly. Although the kinetics of transport into the channel may also play a role, as in our earlier work we observe uniform coating thicknesses throughout the high aspect ratio channels indicating that this process is not kinetically limited. For the case of all-polyelectrolyte assemblies, the magnitude of the observed reduction in bilayer thickness in the channels depended on the concentration of any added salt in the process, varying from a factor of 1.8 in the absence of salt to 1.4 when 0.5 M NaCl was added to the dipping solutions. Figure 4-5 shows that salt-free assembly of the TiO_2/PVS system yields multilayer films on the nanochannel walls that are thinner than the corresponding films assembled free of geometric constraints on the top surfaces by nearly a factor of 5 at 150 bilayers.

A more detailed analysis of the influence of channel confinement on film growth is shown in Figure 4-6 and Figure 4-7. Figure 4-6 shows how the wall/top thickness ratio varies as LbL processing proceeds. Although assembly is always slightly slower for the confined case, above 40 bilayers, significant deviations are seen. To get a better idea of what is happening in the plateau region of Figure 4-5, the mean marginal growth rate was plotted against the inverse gap size in Figure 4-7. Interestingly, the growth rate of the films becomes an approximately linear function of the inverse gap size below dimensions of about 100 nm; extrapolation suggests that confinement at a gap dimension of about 55 nm is sufficient to effectively stop the LbL assembly process in the channels for the TiO_2/PVS system. The 6 nm diameter TiO_2 nanoparticles are significantly smaller than this critical gap size, and the length of the fully-extended configuration of a 40-unit PVS chain is only about 10 nm. It therefore seems unlikely that geometric exclusion of the constituents of the TiO_2/PVS system is responsible for the diminishing assembly rates in the channels. Thus, as suggested in our earlier study[118] of all-polymer assembly in nanochannels, it appears that the presence of surface charge on the channel walls[69] provides a sufficient level of electrostatic repulsion over the full width of the channel to deplete the supply of adsorbing species needed for LbL growth on the channel walls.

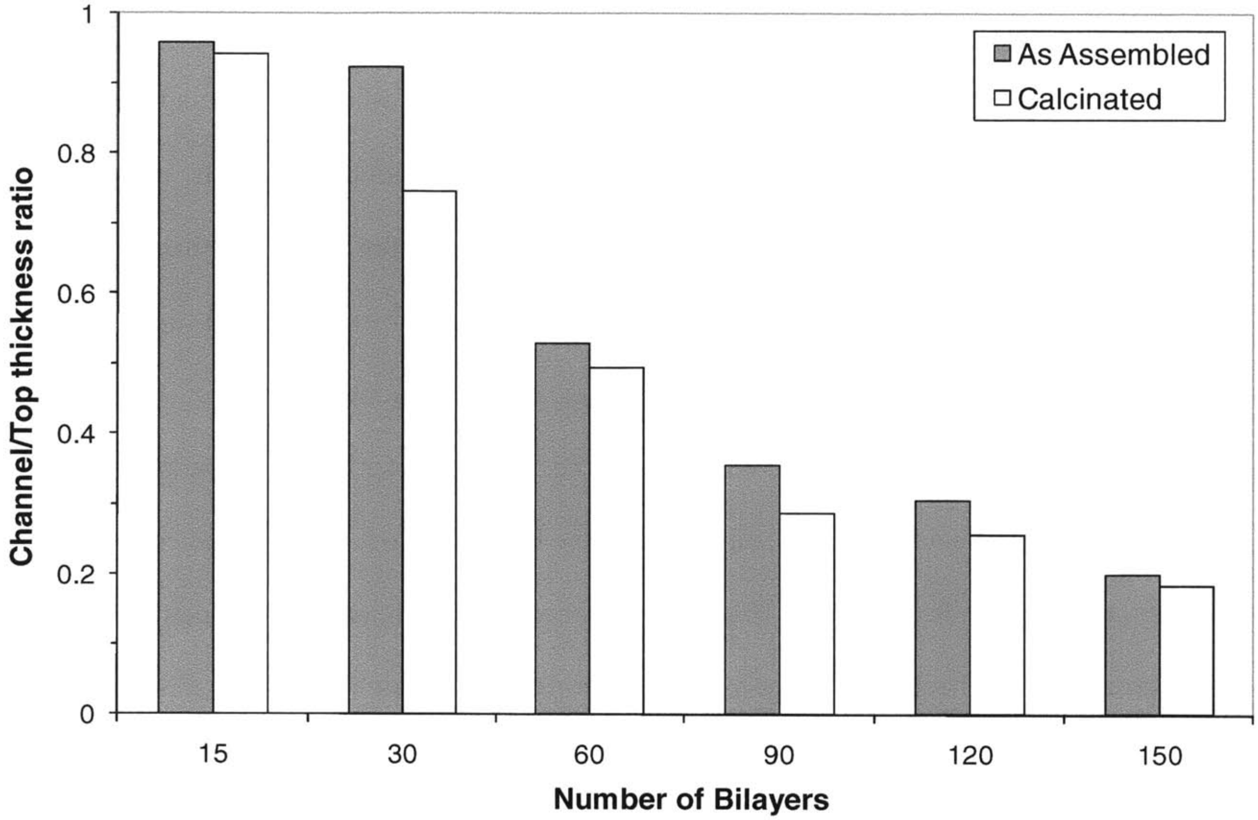

Figure 4-6 The ratio of the film thickness in the nanochannel to that on the top surface for as-assembled (filled) and calcinated (open) TiO_2/PVS multilayers as a function of the number of deposited TiO_2/PVS bilayers.

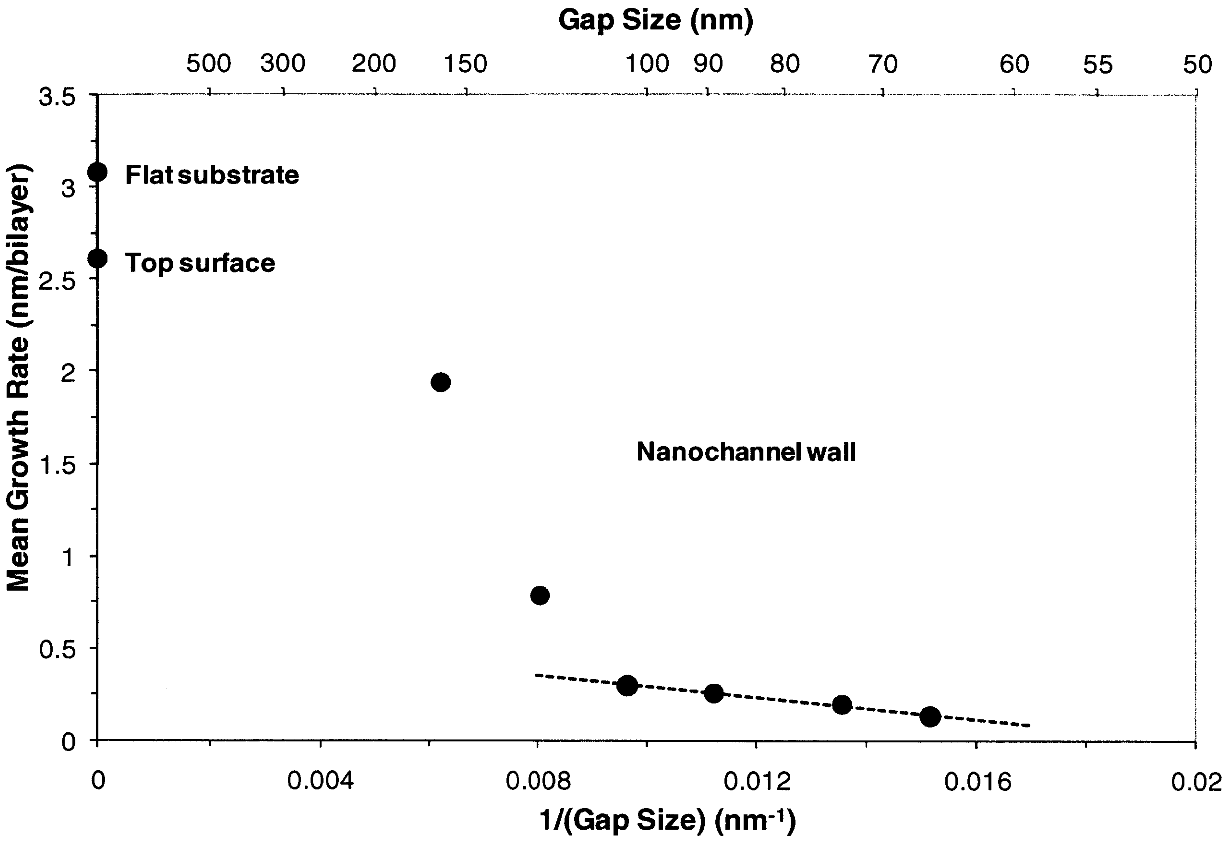

Figure 4-7 Comparison of the mean growth rate of TiO_2/PVS multilayers deposited in nanochannels and on flat substrates. The dotted line represents a linear fit of the last four data points as a function of the inverse gap size.

The PDAC/SiO_2 System

To demonstrate that the above results are generalizable, we also performed LbL assembly of PDAC/SiO_2 in nanochannels and used calcination to form conformal, nanoporous silica films. Unconfined assembly of PDAC/SiO_2 resulted in uniform deposition and thickness growth which was linear with respect to the number of deposited bilayers. As with the TiO_2/PVS multilayers, the average unconfined as-assembled bilayer thickness (*ca.* 9.89 nm/bilayer) was smaller than the diameter of the SiO_2 nanoparticles used. The refractive index and porosity of calcinated PDAC/SiO_2 multilayer films were measured using spectroscopic ellipsometry. The refractive indices of PDAC/SiO_2 films were about 1.28–1.29 independent of the number of deposited bilayers and the porosity was estimated to be ~38%. The nanoporous structure of calcinated

PDAC/SiO_2 multilayer films results from the rearrangement and close-packing of silica nanoparticles after removal of polymers.[17,19,48] Figure 4-8 shows that, similar to TiO_2/PVS, LbL assembly of the PDAC/SiO_2 multilayers within the nanochannel template differs significantly from that on an unconfined surface. On planar surfaces, linear growth persists up to 60 bilayers with average bilayer thicknesses of 9.2 nm/bilayer as-assembled and 8.7 nm/bilayer after calcination. The growth curve for confined PDAC/SiO_2 multilayers is shown in more detail in the inset of Figure 4-8. As before, the data can be described by an inverted exponential decay, with an ultimate film thickness of 84 nm. Figure 4-8 shows that salt-free assembly of PDAC and SiO_2 yields confined multilayer films that are thinner than the corresponding films assembled free of geometric constraints by more than a factor of 6 at 60 bilayers.

The SEM micrographs of Figure 4-9 clearly show the thickness contrast between multilayers deposited outside and within the nanochannels. Once again, the channel gaps remain open throughout the assembly process and the PDAC/SiO_2 multilayer films on the nanochannel walls are of uniform thickness from the top to the bottom of the channels. High temperature calcination leads to conformal nanoporous coatings with no visible defects.

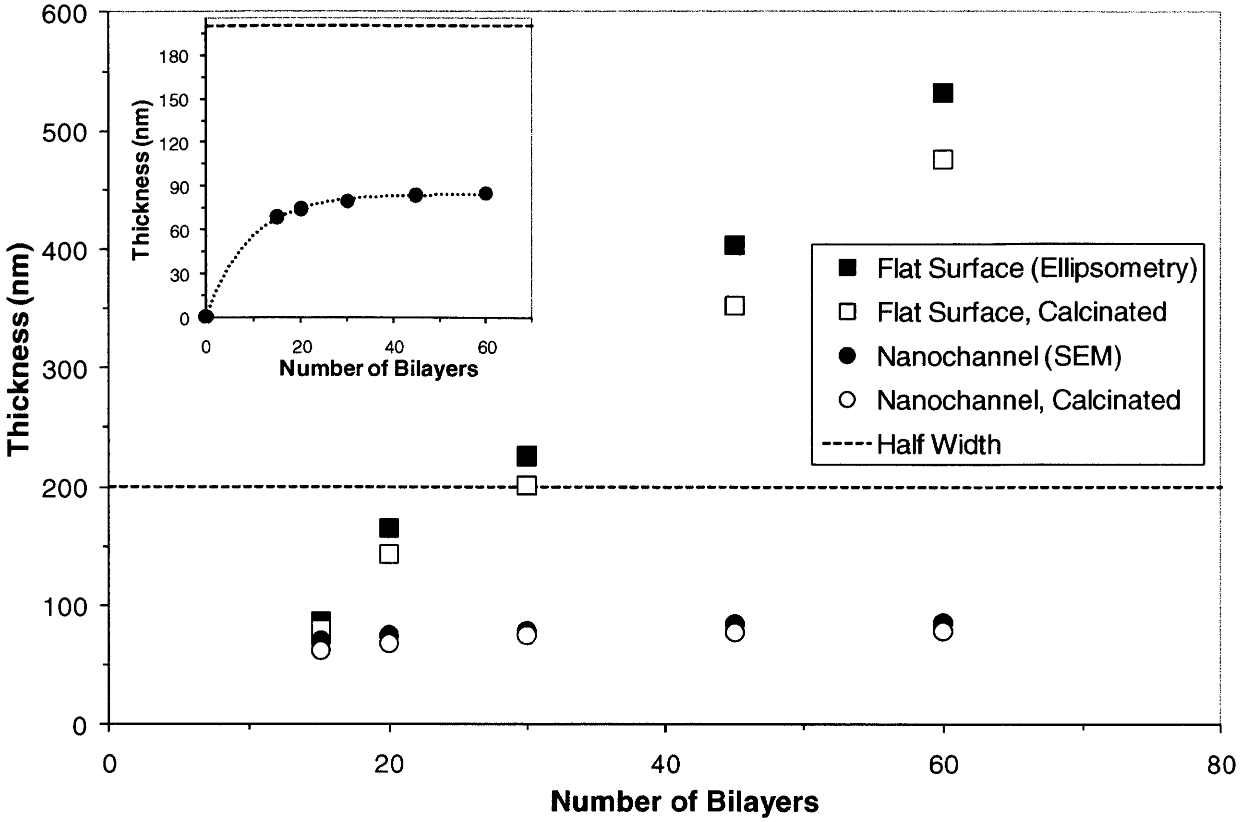

Figure 4-8 Thickness of PDAC/SiO_2 multilayers deposited at pH 9.0 with no added salt on the top surface (squares) and nanochannel wall (circles) as a function of the number of deposited bilayers. Filled and open symbols represent the thickness of as-assembled and calcinated films, respectively. Inset: growth behavior of PDAC/SiO_2 multilayers on the nanochannel walls as a function of the number of deposited bilayers. The dotted lines are the best fit exponential decay curves, $k = k_0[1 - \exp(-b/b_0)]$. The parameters obtained from the best fits are $k_0 = 84.1$ nm and $b_0 = 9.2$ bilayers.

Figure 4-10 shows how the ratio of wall/top film thicknesses varies as LbL deposition proceeds. In this case, lower growth rates are observed almost immediately and become significant above just 20 bilayers. In Figure 4-11, it can be seen that the nominal growth rate of the multilayer becomes an approximately linear function of the inverse gap size, and extrapolation suggests that confinement at a gap of about 210 nm results in no further deposition for the PDAC/SiO_2 system which is considerably larger than the 55 nm gap obtainable using TiO_2/PVS. This value is significantly bigger than both the dimensions of either the nanoparticles or polymer molecules, pointing again to surface charge-induced depletion of unadsorbed species as the likely mechanism.

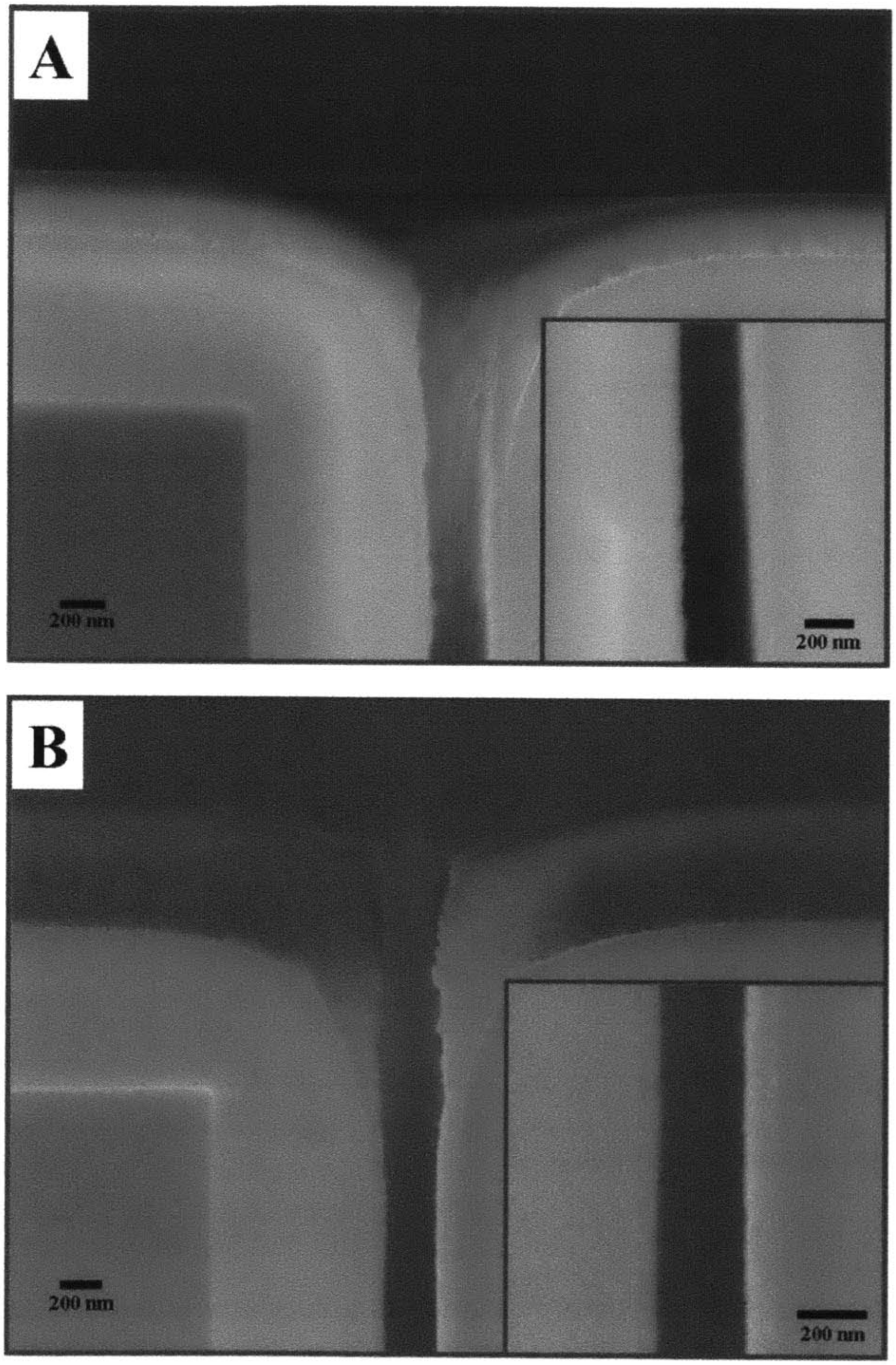

Figure 4-9 (A) SEM micrograph showing a cross-sectional view of the nanochannels coated with 30 bilayers of PDAC/SiO_2 The inset is a magnified view of the uniform, conformal multilayer within the nanochannel. (B) SEM micrograph of the nanochannels coated with a 60 bilayer PDAC/SiO_2 film after calcination. The inset is a cross-sectional image showing a conformal film of nanoporous silica throughout the nanochannel after calcination.

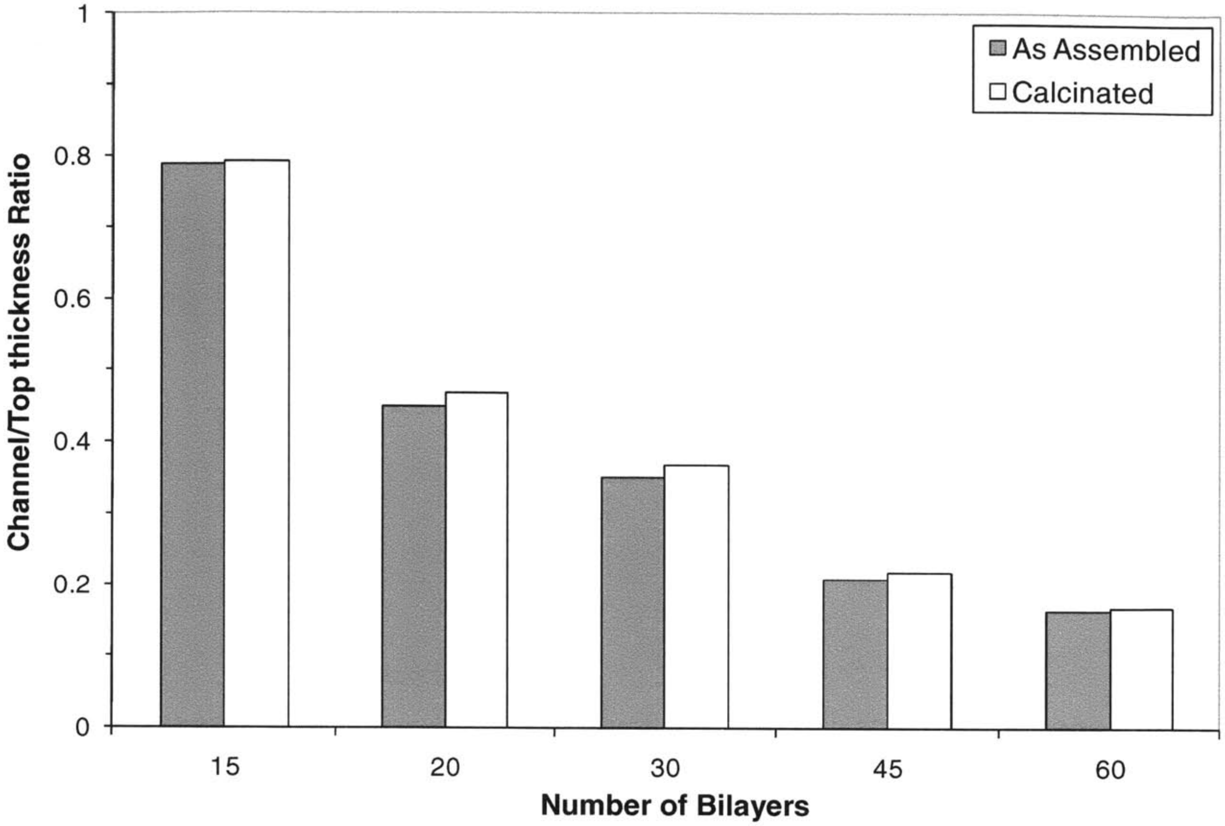

Figure 4-10 The ratio of the film thickness in the nanochannel wall to that on the top surface for as-assembled (filled) and calcinated (open) PDAC/SiO_2 multilayers as a function of the number of deposited bilayers.

These two studies show that for two polymer/nanoparticle systems we have achieved conformal, uniform multilayers with no observable bridging. The only significant difference between the results of these two studies is the significant difference in the lowest achievable gap size. We believe that this difference is attributable to the significantly different ionic strengths of the solutions from which these multilayers were assembled. Although no salt was added in either case, acidic and basic solutions were used to adjust the pH of each solution to the desired value. In the TiO_2/PVS case, the pH was 1.5 implying an ionic strength of about 0.03 M whereas in the PDAC/SiO_2 case, the pH was 9 and the ionic strength was on the order of 10^{-5} M. The limiting gap sizes for these systems are 55 nm and 210 nm respectively. For comparison, in our earlier work on PAH/PSS we achieved gap sizes of about 25 nm at an ionic strength of 0.1 M.[118]

These data are consistent with our proposed growth limitation mechanism of exclusion within the nanochannels. At low ionic strength, the wall surface charge is not as well screened, resulting in exclusion of charged species at higher gap sizes.

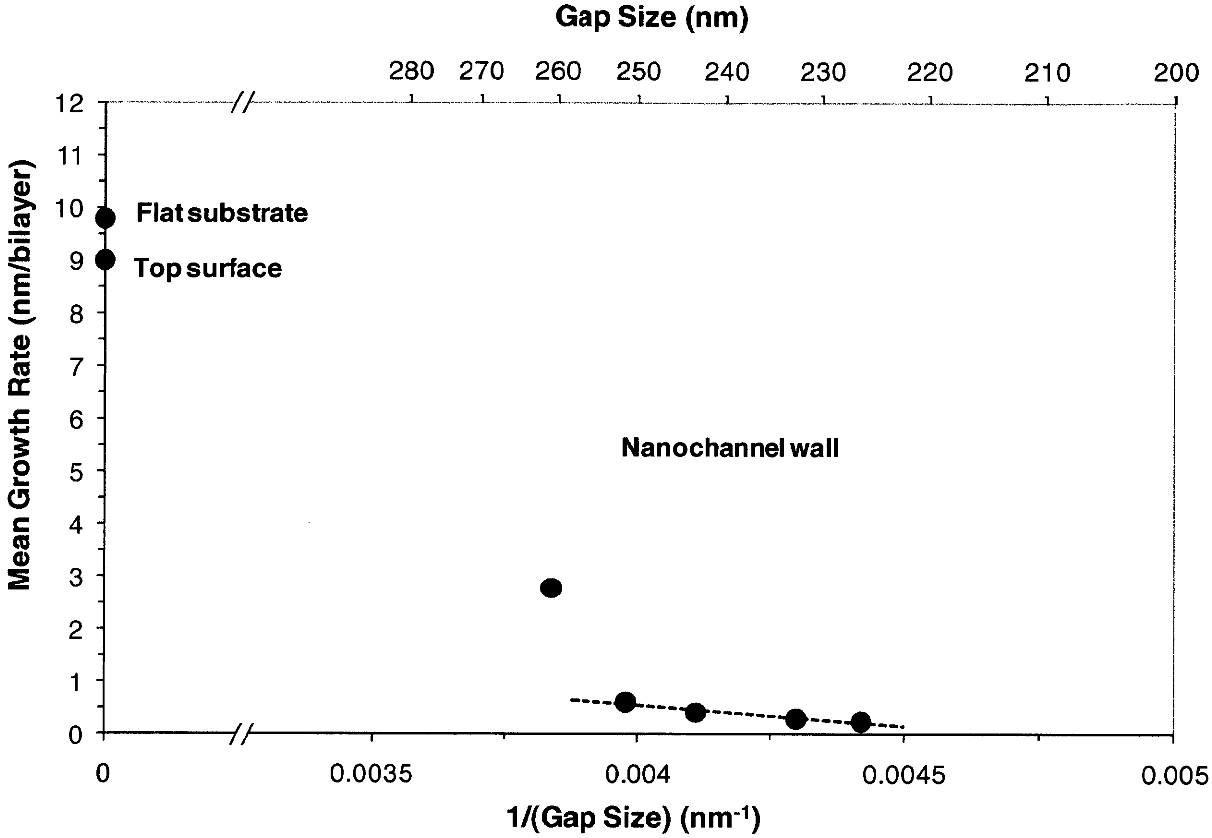

Figure 4-11 Comparison of the mean growth rate of PDAC/SiO_2 multilayers deposited in nanochannels and on flat substrates. The dotted line represents a linear fit of the last four data points as a function of the inverse gap size.

Ali *et al.* have also observed that confined LbL assembly of charged species results in interesting phenomena which differ from those found on a flat surface.[119] They measured *I-V* curves of track etched polycarbonate membranes containing asymmetric pores and observed rectification of ionic current. They fit these results to a Poisson-Nernst-Planck model to calculate the surface charge within the pore. They then assembled multilayer films of PAH and PSS within these pores and, assuming a constant LbL growth rate obtained from the literature, determined the dependence of surface charge on multilayer growth. They concluded that the surface charge of confined multilayers decreases as deposition proceeds and attributed this effect to ion pairing within the film. This proposed phenomenon could be another explanation for why we observe lower bilayer thicknesses as the gap size becomes smaller. It should be noted, however, that exclusion of charged species within the gap would also result in reduced charge overcompensation in agreement with Ali's results.

4.4 Conclusions

In this work we have used LbL assembly of TiO_2/PVS and PDAC/SiO_2 multilayers to conformally and uniformly coat high aspect ratio nanochannel arrays with polymer/nanoparticle composite multilayers and with nanoporous inorganic films. The multilayer thickness and therefore the nanochannel gap size can be tuned systematically by controlling the number of deposited bilayers. LbL assembly of TiO_2/PVS from solutions containing no added salt was successfully achieved down to gaps of below 80 nm and may be possible down to 55 nm. Films deposited on unconfined surfaces were significantly thicker than those deposited within the channels. These results support the idea that surface charge-induced depletion of unadsorbed species in confined geometries limits the growth of LbL assembled thin films within narrow channels, especially at low ionic strengths. The ability to functionalize high aspect ratio nanochannels with conformal, nanoporous, inorganic films has numerous applications including micro/nanofluidic reactors and separators or sensors based on size, charge, and potentially chemical or biological selectivity.

An interesting extension of this work is the feasibility of using LbL to fabricate all-nanoparticle multilayers. The following chapter describes our work on the deposition of these multilayers and the interesting complications which arise when no polymers are used.

Chapter 5 Layer-by-Layer Deposition of All-Nanoparticle Multilayers in Confined Geometries

5.1 Introduction

The layer-by-layer assembly of polyelectrolytes in confined pores or channels has been studied extensively in recent years. Many researchers have used this flexible surface modification technique to manipulate the surface charge in microfluidic devices[77,90,94] or in thin capillaries used for electrophoresis,[91] to decorate confined surfaces with functional nanoparticles or biomolecules,[92] to enable stimuli-responsive gating,[21] and to tune the optical properties of photonic crystals.[43] Others have used LbL assembly within porous templates to form polymer nanotubes[24,26,87,88] and nanoporous polymer spheres.[42] Still others have focused on the fundamental behavior of polyelectrolyte deposition in confined geometries.[41,93,95,118,121,122] In earlier work, we have found that PAH/PSS multilayers within confined geometries are thinner than those deposited on unconfined surfaces and that this effect is magnified by low ionic strength and by greater confinement.[118] Lazzara *et al.* came to very similar conclusions based on LbL deposition of dendrimers within the pores of AAO membranes.[121]

In a subsequent publication,[123] we investigated the LbL assembly of two nanoparticle/polyelectrolyte pairs within confined nanochannels. We demonstrated that at low ionic strength, drastically thinner multilayers are observed within confined channels, all without blocking or plugging of the channel itself. In this work, we extend on these results by investigating the LbL deposition of only nanoparticles within confined nanochannel arrays. In particular, we sequentially deposit silica and titania nanoparticles which have successfully been used to form antireflective, superhydrophilic, self cleaning films[17] as well as a means of producing structural color[19,27,28] when deposited on flat surfaces. The use of only nanoparticles implies additional constraints on the assembly conditions due to their propensity for aggregation and their rigid nature.[48] Due to these added complications, the behavior of this nanoparticle system in nanochannels is of fundamental interest. Additionally, the ability to form an intrinsically nanoporous multilayer within a porous substrate without harsh post-treatments like calcination may be of practical value in applications such as selective separations.

5.2 Experimental Section

Materials

Titania nanoparticles (average particle size ~6 nm) were synthesized by hydrolysis of titanium tetraisopropoxide as described in detail elsewhere.[120] Briefly, 2.5 mL titanium tetraisopropoxide was dissolved in 50 mL of ethanol and added dropwise to an ice bath-cooled, continuously stirred solution of DI water which had been adjusted to pH 1.5 using nitric acid (70 wt%, Sigma-Aldrich). The solution was allowed to stir overnight in the ice bath and then stored in a refrigerator. Silica nanoparticles (average particle size ~15 nm) were purchased from Sigma-Aldrich (Ludox HS-40, 40 wt%). Nanochannel arrays were fabricated by thermal oxidation of approximately 1.5 μm channels patterned by conventional photolithography as described in detail in Section 2.1.[59] The nanochannels were approximately 700 nm wide and 10 μm deep and therefore have an aspect ratio of about 15. Silicon wafers were purchased from WaferNet Inc. and served as control planar substrates.

LbL Assembly

DI water (18.2 MΩ·cm, Millipore Milli-Q) was used in all deposition solutions and rinse baths. The titania colloidal suspension was filtered using a 0.02 μm syringe filter (Anotop 25, Whatman) and diluted to 0.015 wt% with DI water adjusted to pH 1.5 using nitric acid. The silica suspension was filtered using a 0.2 μm syringe filter (Anotop 25, Whatman) and diluted to 0.015 wt% with pH-adjusted DI water. Rinse baths of the same pH as the deposition solution were prepared using DI water and filtered using 0.2 μm polyether sulfone filtration membranes (VWR). The titania rinse baths were adjusted using nitric acid to pH 1.5 while the silica rinse baths were adjusted to pH 9.0 with NaOH or to pH 3.0 with HCl.

Nanochannel array samples of approximately 0.5 cm^2 were affixed to glass slides using plasma-activated PDMS. These substrates as well as silicon wafer control samples were degreased by 10 min sonication in detergent solution (3% Micro-90, International Products Corp.) and then cleaned by 10 min sonication in 1 M HCl and in DI water. Automated LbL assembly was performed using a StratoSequence VI spin dipper (nanoStrata Inc.). Substrates were immersed in the titania and silica deposition suspensions for 15 min followed by three intermediate rinsing steps of 2, 2, and 1 min. The substrates were spun at 120 rpm during all deposition and rinsing steps. Every twenty bilayers, the deposition suspensions and rinse solutions were exchanged for fresh ones. Upon completion of LbL assembly, samples were removed immediately and dried with compressed air.

Characterization

The thicknesses of LbL-assembled nanoparticle films on planar silicon substrates were measured using spectroscopic ellipsometry (XLS-100, J.A. Woollam Co., Inc.) and profilometry (P-16+, KLA-Tencor). Films assembled within nanochannel arrays were characterized using SEM (JEOL 6320). Cross sectional samples were prepared by fracture of the coated array using a diamond scorer and sputter-coating with gold/palladium.

5.3 Results and Discussion

LbL assembly was first attempted using positively charged pH 1.5 titania nanoparticles and negatively charged pH 9.0 silica nanoparticles. At these pH values, both nanoparticles are highly charged.[48] The thicknesses of films deposited on planar silicon wafers were measured via ellipsometry and are shown in Figure 5-1. A linear fit of the data gives a slope of 0.30 nm/bilayer which is extremely low given that the nanoparticles have diameters of 6 and 15 nm. This means that nanoparticle adsorption is very sparse at every deposition step. The nonzero intercept indicates that there is an initial stage of higher growth, but even after 80 bilayers of LbL processing, the film is only about four nanoparticle bilayers thick. A micrograph of an 80 bilayer film deposited on a nanochannel array is shown in Figure 5-2. We see that the multilayer is extremely thin and, since it is partly composed of silica, is difficult to distinguish from the surface of the device. Interestingly, although the channels are coated conformally and uniformly, we do notice some instances of bridging of the nanochannels near the entrances of the channels.

The slow growth observed both via ellipsometry and SEM is due to unbalanced surface charge among the two types of nanoparticles. Silica nanoparticles are very highly negatively charged at pH 9.0, while titania nanoparticles have a positive charge which is lower in magnitude at pH 1.5.[48] To circumvent this problem, we repeated these experiments using much more moderately charged SiO_2 nanoparticles deposited at pH 3.0. The thicknesses of all-nanoparticle films on planar silicon substrates were measured using ellipsometry and profilometry and are plotted in Figure 5-3. These data show significantly higher growth rates with a bilayer thickness of about 13 nm. The significantly negative intercept indicates that growth is uneven at first and does not reach steady state until about 20 bilayers.

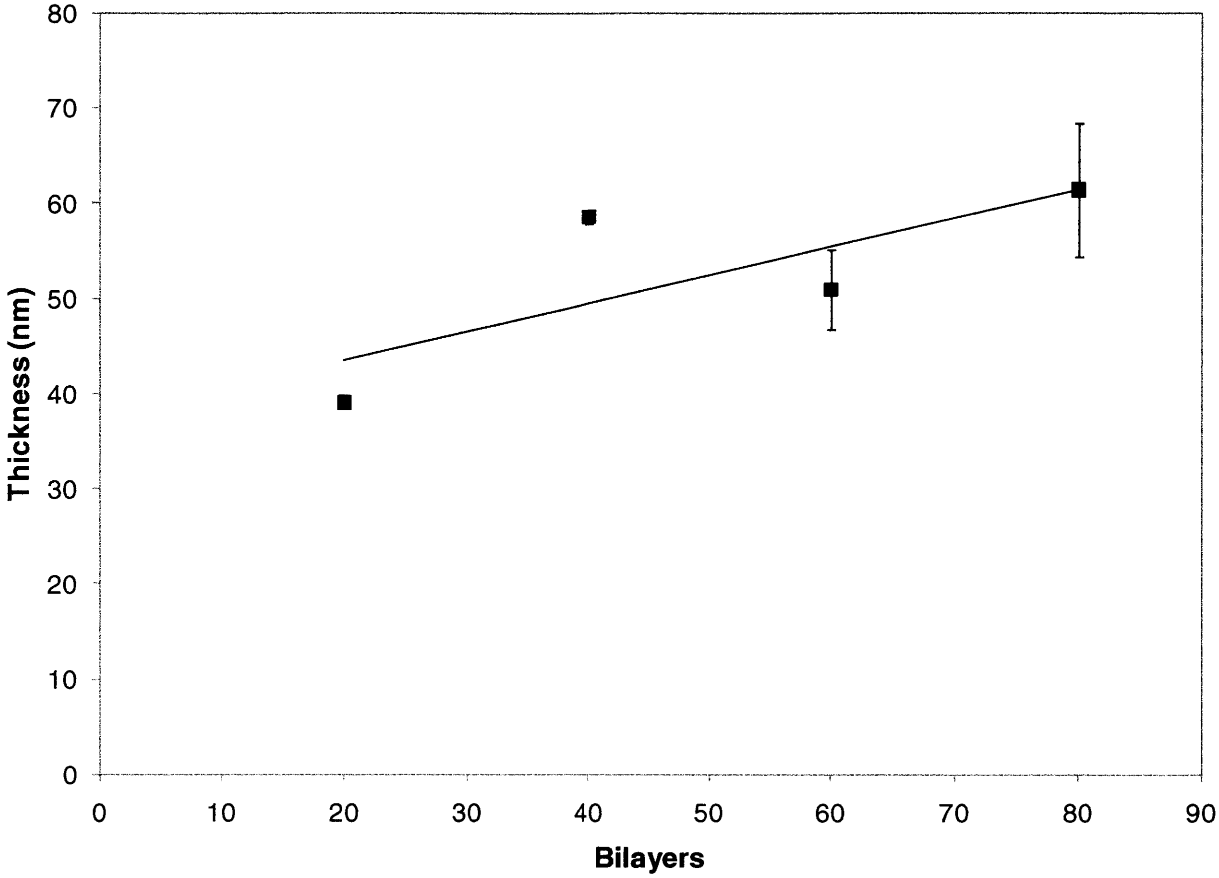

Figure 5-1 Growth curve for deposition of TiO_2 at pH 1.5 and SiO_2 at pH 9 obtained via ellipsometry. The bilayer thickness is just 0.3 nm/bilayer and the nonzero intercept indicates unsteady growth initially.

Cross-sectional SEM micrographs of fractured nanochannel array samples were taken to determine the structure of these nanoparticle multilayers within nanochannels. A set of wide view micrographs showing a large number of channels is given in Figure 5-4. These micrographs yield a number of interesting observations. First, it is clear that the channels are conformally and uniformly coated with nanoparticle multilayers with the exception of the channel entrance at high film thicknesses. Second, it is clear that the tops of the unconfined posts exhibit significantly higher multilayer growth rates than the confined channels. Third, and most interestingly, we see systematic and reproducible bridging of the nanochannels at about 40 bilayers and essentially complete covering of all nanochannels at 60 bilayers and above.

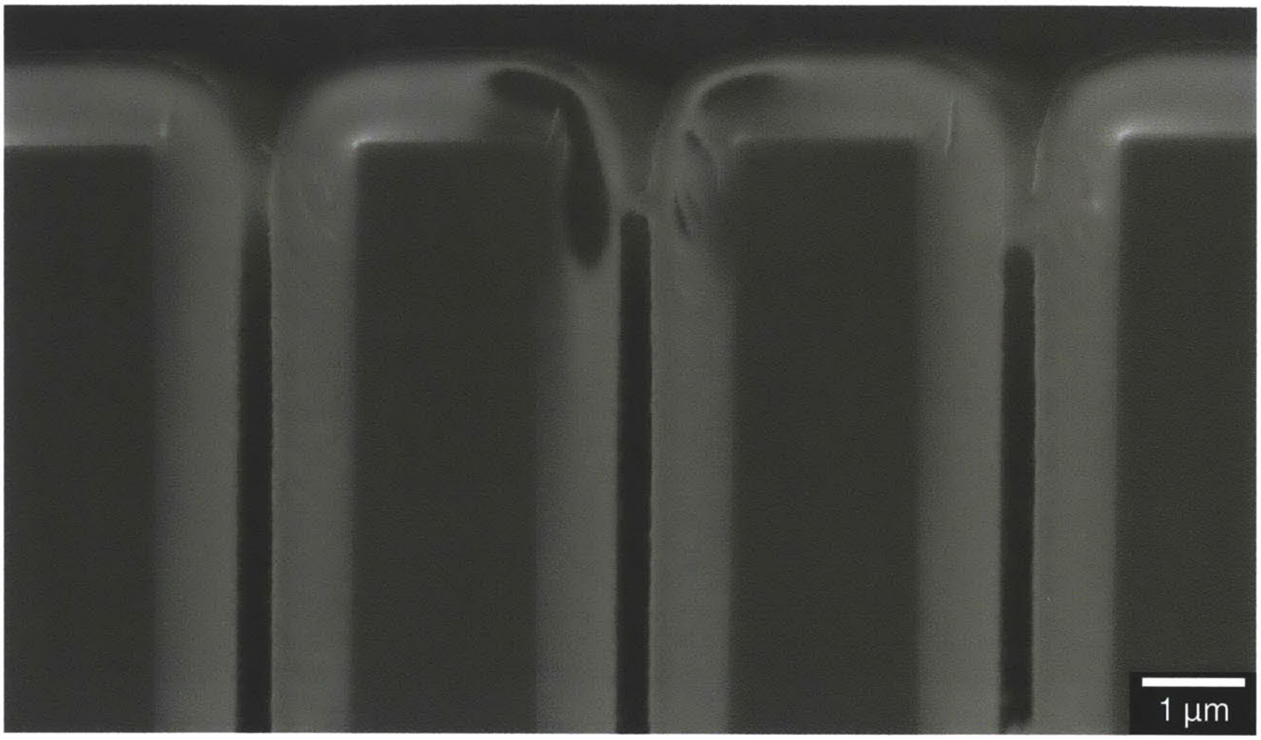

Figure 5-2 Cross-sectional micrograph of a nanochannel array coated with 80 bilayers of TiO_2 at pH 1.5 and SiO_2 at pH 9. The coating is extremely thin, but does exhibit bridging of the nanochannels in some cases.

After 20 bilayers we see results very similar to those observed for polymer/nanoparticle LbL deposition as discussed in Section 4.3[123]. The multilayer conformally coats the entire channel uniformly and without any bridging or clogging. A magnified view of the nanochannel array subjected to 20 bilayers of LbL processing is presented in Figure 5-5. Again the poor contrast between the silica nanochannel substrate and the silica/titania multilayer makes it somewhat difficult to see, but the texture difference renders the film clearly visible. We can see that the thickness atop the posts is significantly larger than that within the channels.

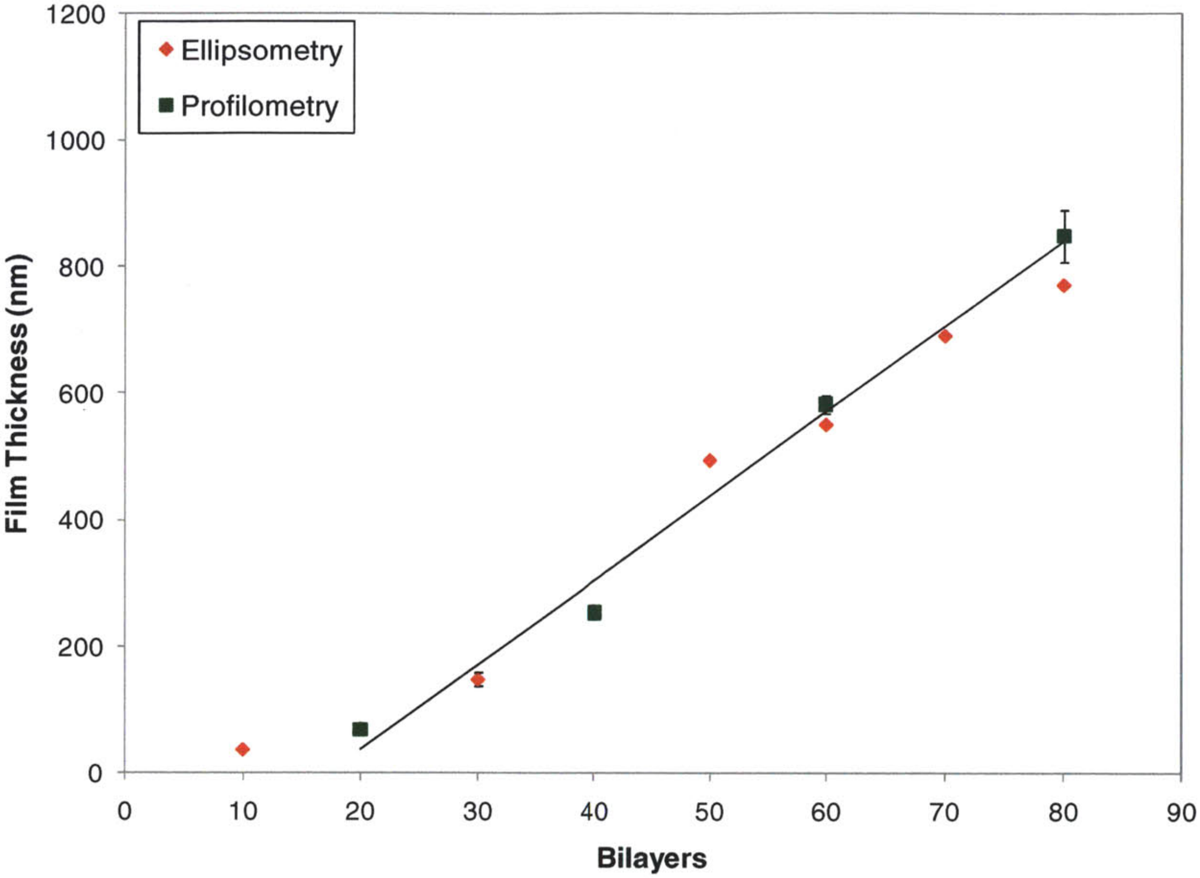

Figure 5-3 Nanoparticle multilayer thickness on planar silicon substrates as determined by ellipsometry and profilometry. After an initial period of slow growth, the film grows linearly with a slope of about 13 nm/bilayer.

After 40 bilayers, the story becomes much more interesting. Figure 5-4 shows that about half of the nanochannels are completely bridged, some are completely open, and others show bridges in the process of forming. Figure 5-6 provides a magnified view of this substrate and provides a good example of all three of these states. The channel on the left is completely bridged, the one in the middle exhibits a very delicate bridge which has just been formed, and the one on the right is almost completely open, although we can observe a thickening of the film near the mouth of the channel where a bridge will soon form. The insets show magnified views of fully formed and newly formed bridges. The discrepancy between unconfined and confined multilayer thicknesses is also more clearly evident at 40 bilayers. Although for some channels this is attributable to blockage of the channel, other channels that have not been bridged still clearly exhibit this discrepancy.

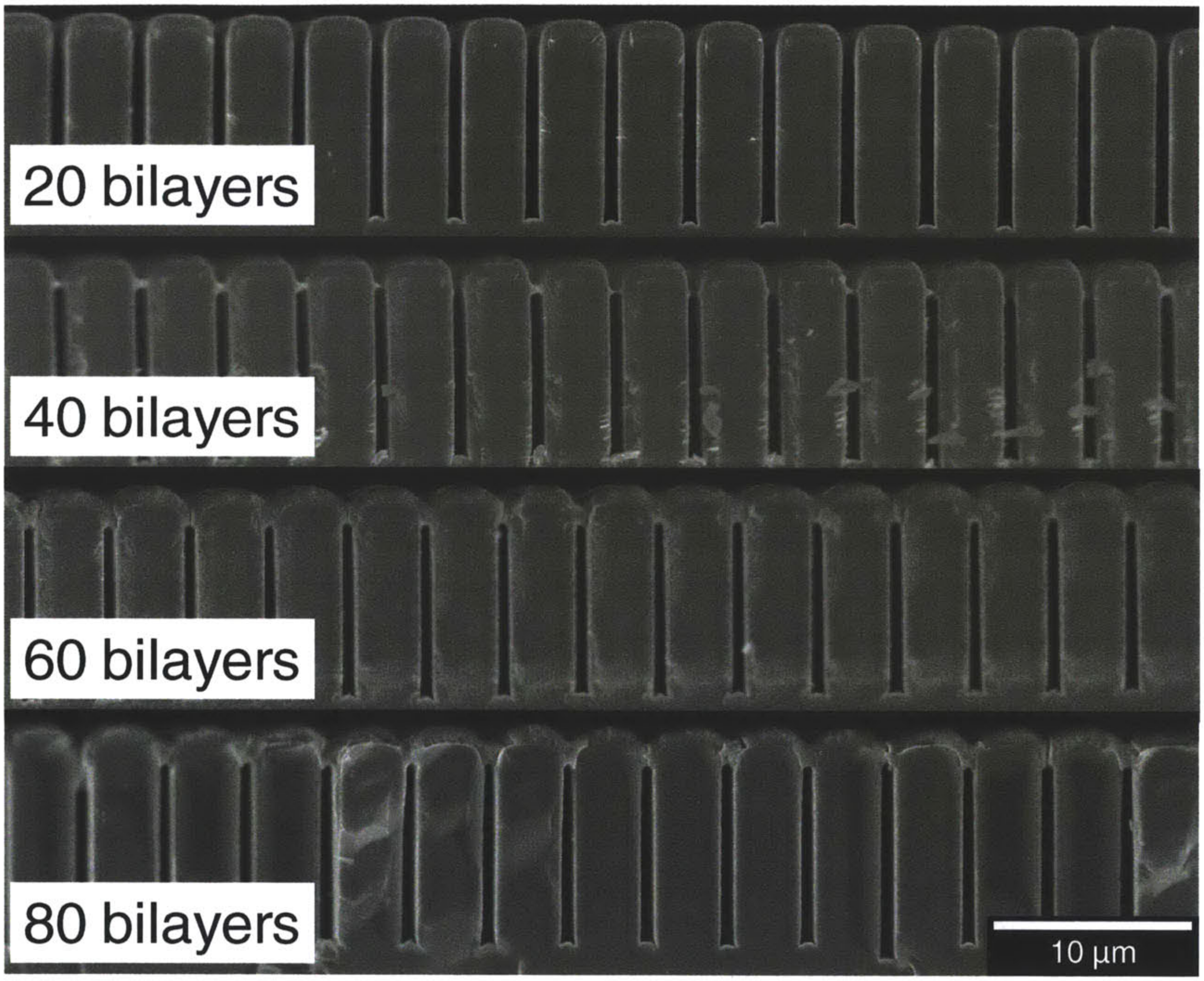

Figure 5-4 Composite micrograph highlighting the systematic nature of the bridging of nanochannels with TiO_2/SiO_2 nanoparticle multilayers. At 20 bilayers no bridging is observed, after 40 bilayers bridges begin to form, and at 60 and 80 bilayers channels are completely covered.

After 60 bilayers of LbL processing we obtain structures like those seen in Figure 5-7. We can see that the thickness of the unconfined multilayer is now very substantial and that the thicknesses of the bridges have drastically increased. In fact, the thickness of the bridge is greater than that of the multilayer on top of the posts. This suggests that the film grows quite quickly over a channel once it has been bridged. Some defects in the nanochannel are also evident in Figure 5-7. In one case, slight delamination from the surface appears to have occurred. This is likely due to the stresses which occur in the substrate and coating during fracture in preparation for SEM imaging. The fact that many defect-free channel bridges are also observed lends credence to this explanation. The other prominent defect is a small crack running through the bridge along the midline of the channel. This may also be caused by the force of fracturing the sample, but reveals that in some cases the bridges have at the least a weak spot and possibly even a small crack running through the middle of them. Nearly all defects fell into one of these two categories.

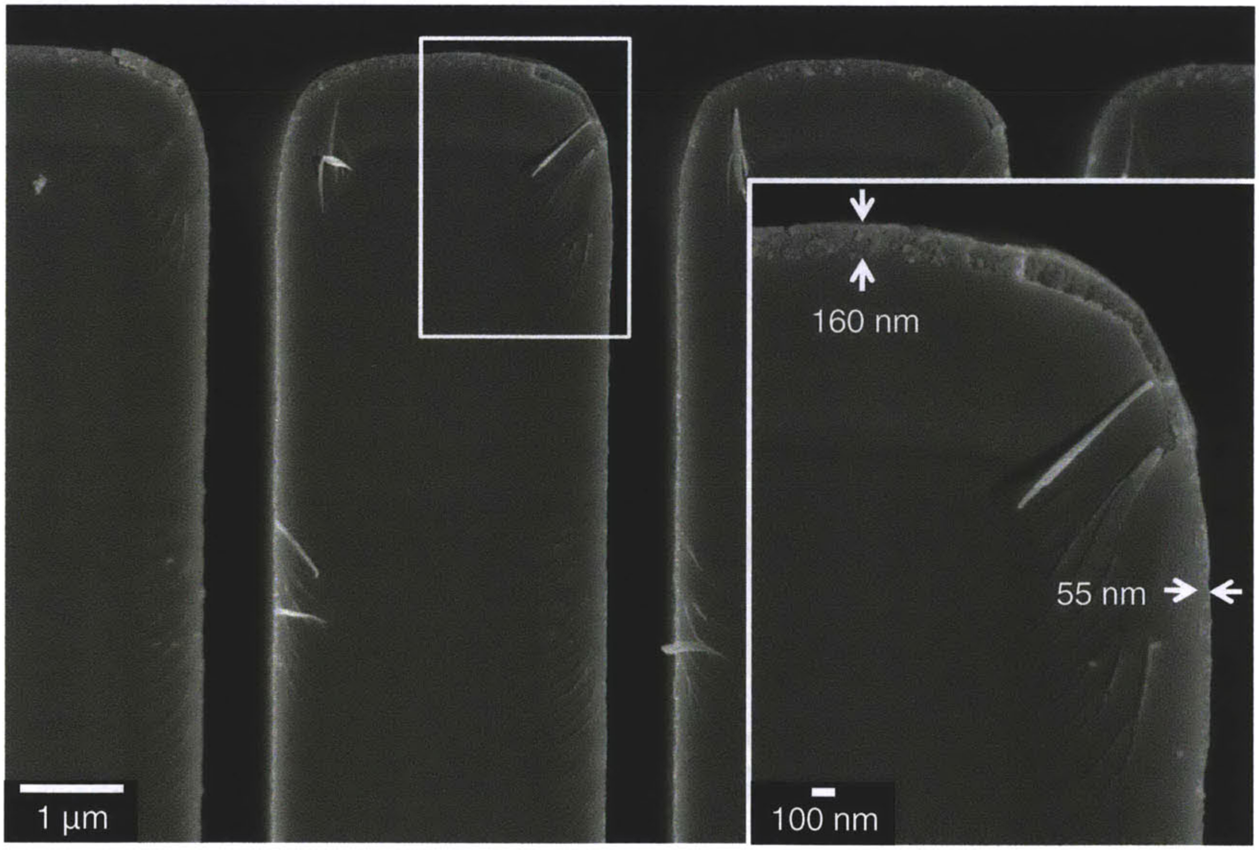

Figure 5-5 SEM micrograph of a nanochannel array coated with 20 bilayers of TiO_2/SiO_2 nanoparticles. Excellent conformality and uniformity are observed and the texture of the porous nanoparticle coating can be directly seen. The inset clearly shows the discrepancy between the thickness of the nanoparticle film on the top of the posts and that within the nanochannel.

After 80 bilayers, similar results are observed as shown in Figure 5-8. The thickness of the multilayer capping the entire substrate continues to grow and the thickness of the bridges remains higher than that of the unconfined multilayer. Although in general adhesion of the film is good, some small defects are present. Figure 5-9 provides a highly detailed view of the multilayer itself. We can clearly see the texture inherent in this nanoporous coating and can even see individual nanoparticles which appear to be roughly close-packed and are consistent with the 15 nm diameter expected for SiO_2 nanoparticles.

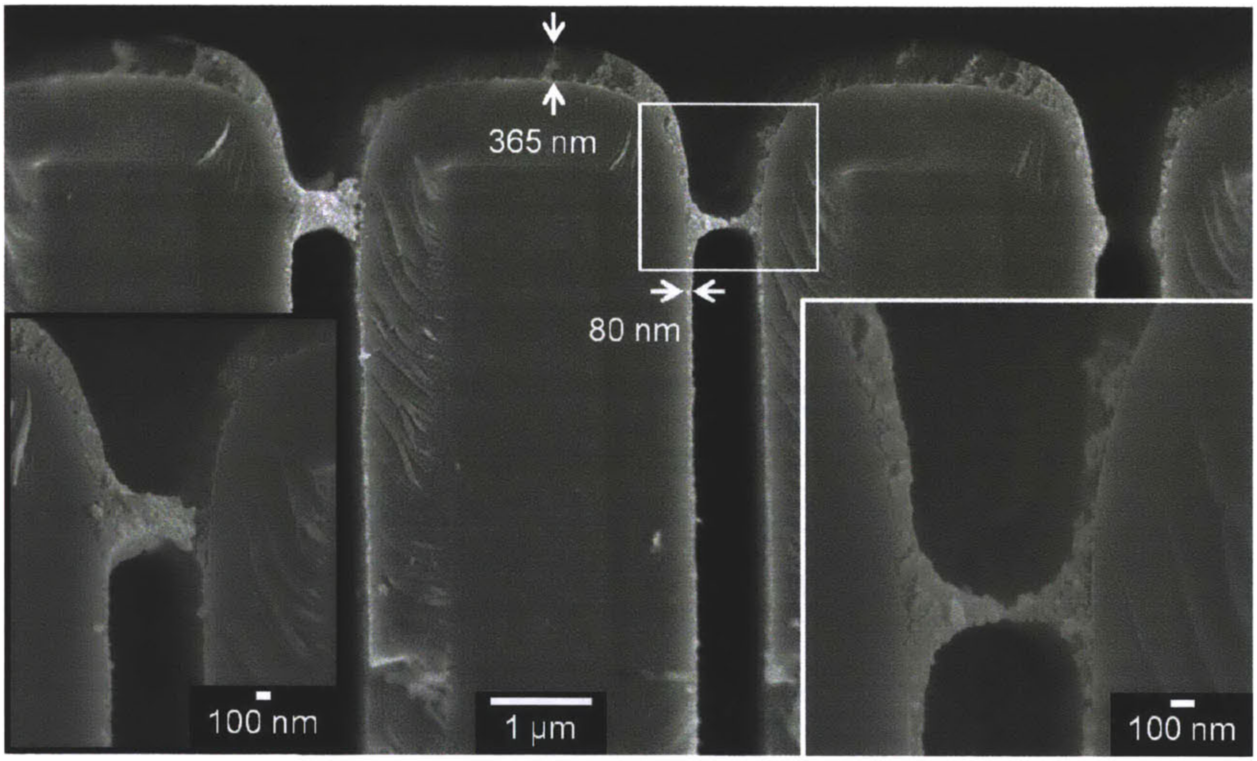

Figure 5-6 Micrograph of a nanochannel array coated with 40 bilayers of TiO_2/SiO_2 nanoparticles. Excellent conformality and uniformity are again observed, with the exception of bridge formation at the top of the channel. The process of bridge formation can be seen here as the rightmost channel has small protuberances which will thicken to form a delicate bridge as seen in the center channel. This bridge will then thicken with further deposition to form a robustly sealed channel as seen in the leftmost channel. Significantly thicker multilayers are observed on the unconfined top of the posts compared with the confined walls of the channel. The insets provide magnified views of newly formed and thickened bridges.

Analysis of SEM images of coated nanochannel arrays was used to quantify our results and compare them with those obtained for planar substrates. This comparison is provided in Figure

5-10. The data for the exterior, or top of the nanochannels show agreement with the trend observed using ellipsometry and profilometry, but are systematically higher. Also significant are the large standard deviations associated with these measurements as indicated by the error bars. Each of these points is the average of multiple measurements, indicating that although locally the film is very uniform, the variability across the substrate is relatively large. Comparison of the confined film thickness with the unconfined multilayer thickness and with the half channel width shows significantly slower growth within the channel and multilayers that remain much thinner than the theoretical maximum.

The deposition of nanoparticle multilayers before bridging occurs is consistent with the results for polymer/nanoparticle multilayers presented in Section 4.3. At low ionic strength, we once again observe significantly thicker multilayers on the unconfined top surfaces while the confined walls exhibit much slower growth. The multilayers are conformal and uniform, pointing to an equilibrium effect and not diffusion-limited transport of particles to the bottom of the channel. This is consistent with the idea of electrostatic exclusion of charged particles from the nanochannel due to the wall surface charge as laid out in detail in Section 2.3.

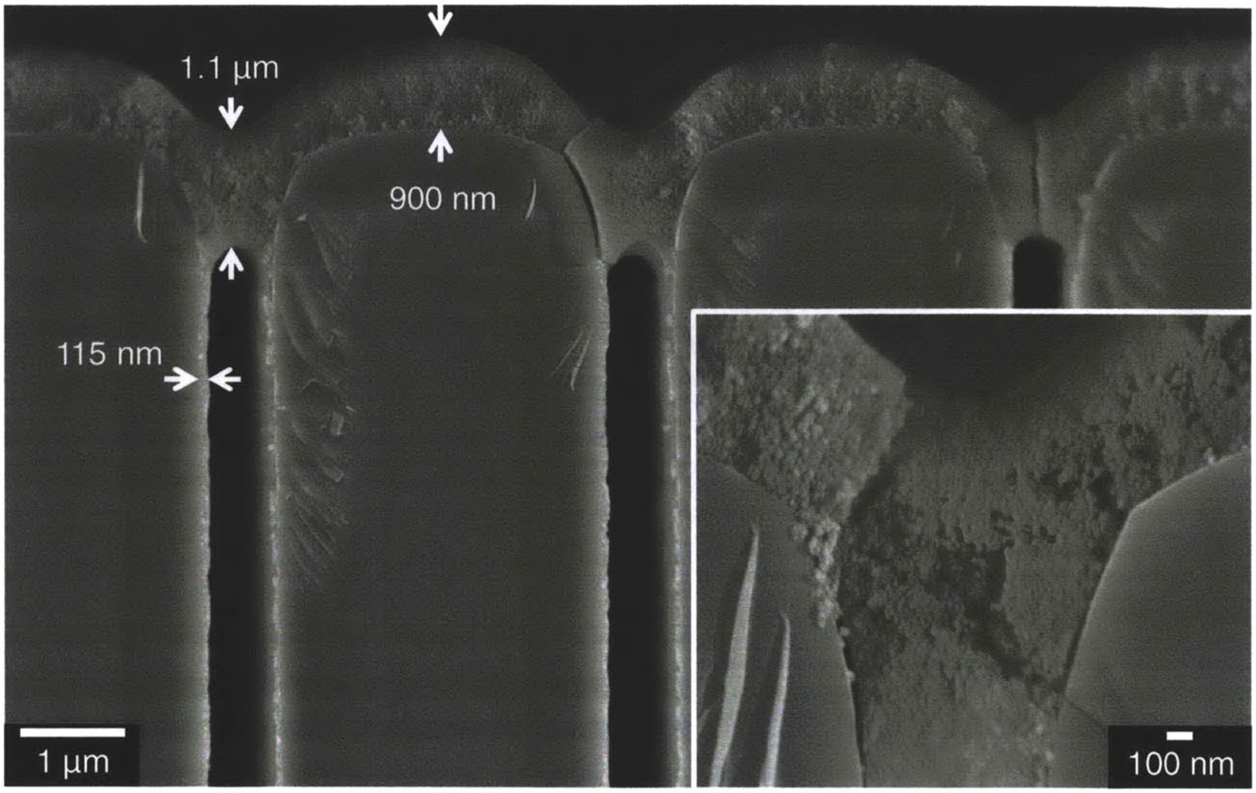

Figure 5-7 Micrograph of a nanochannel array subjected to 60 bilayers of TiO_2/SiO_2 nanoparticle deposition. Complete occlusion of the channel with a thick nanoporous multilayer is observed. Small defects near the channel openings are also evident, though many of these are likely caused by the fracture of the sample in preparation for imaging. The inset provides a magnified view of a nanochannel completely blocked by the nanoporous multilayer.

At around 40 bilayers bridging begins to occur, deviating from the behavior observed previously for polymer/nanoparticle multilayers. One of the most interesting things about this phenomenon is the fact that bridging blocks every single nanochannel and tends to occur at exactly the same point at the mouth of each nanochannel. It seems clear that this bridging phenomenon is a general feature of all-nanoparticle multilayer deposition since similar experiments with polymer/nanoparticle multilayers consistently resulted in open nanochannels, even at high film thicknesses. This is likely due to the intrinsic properties of charged nanoparticles. Unlike polymers, nanoparticles are rigid and therefore cannot bind to many charged sites on the surfaces on which they deposit. As a result, nanoparticles are not adsorbed as strongly to the surface and desorb much more easily as a consequence. One can imagine that if a titania nanoparticle desorbs during the silica deposition step, it will bind with free silica particles in solution, forming a larger aggregate. The resulting aggregates have higher surface charge and are therefore even more strongly excluded from the confined nanochannel and may adsorb preferentially near the entrance.

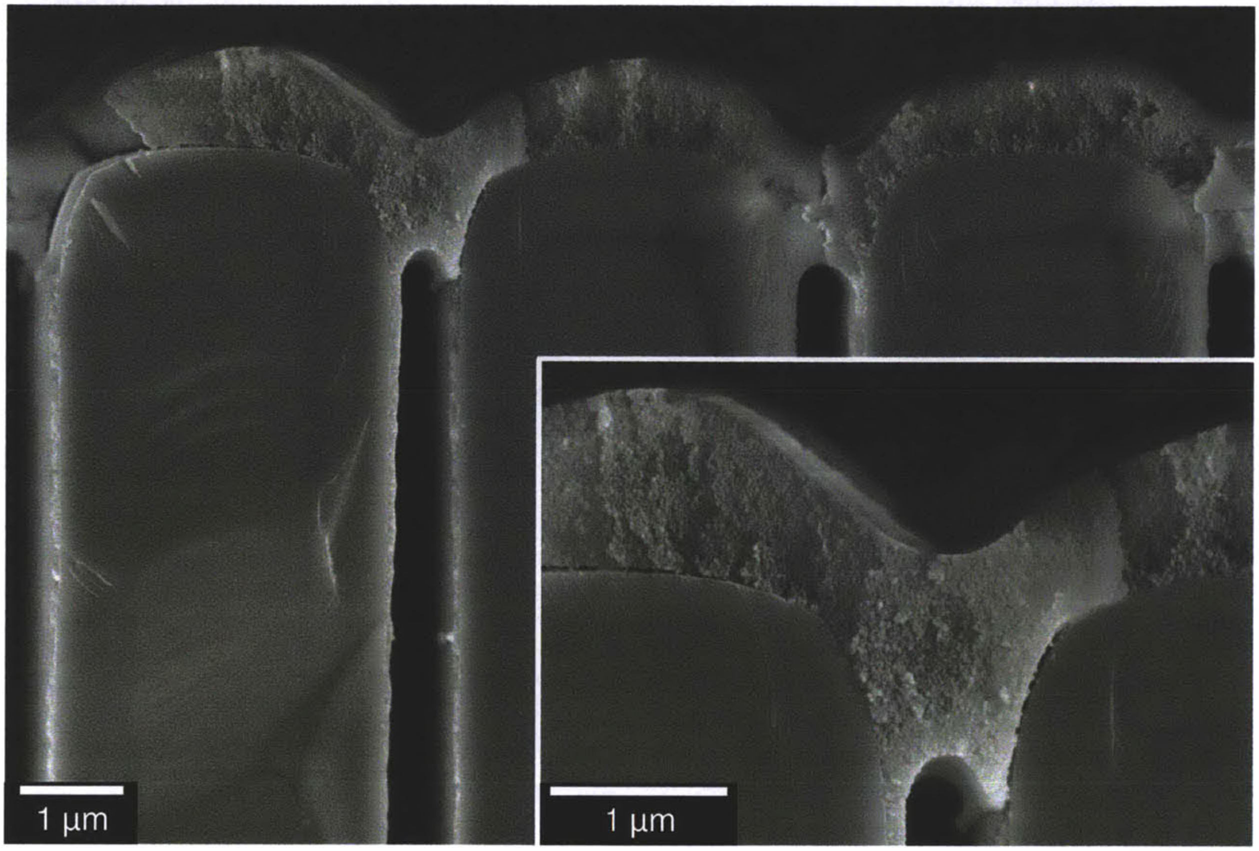

Figure 5-8 Micrograph of a nanochannel array subjected to 80 bilayers of TiO_2/SiO_2 nanoparticle deposition. The inset provides a magnified view of a nanochannel completely blocked by the nanoporous multilayer.

The spinning of the substrate during deposition might also contribute to this effect. Since the tops of the posts are directly exposed to the solution, adsorption of large aggregates might be less stable than within the nanochannel where the liquid is nearly stagnant and diffusion is dominant. This would also explain the dramatically higher growth rate within the hollow above a newly formed bridge. Alternatively this higher growth could be a simple consequence of the geometry; as the film grows from both sides of a V-shaped trench, the vertical depth of the film will grow more quickly than the thickness measured perpendicular to the sides of the trench.

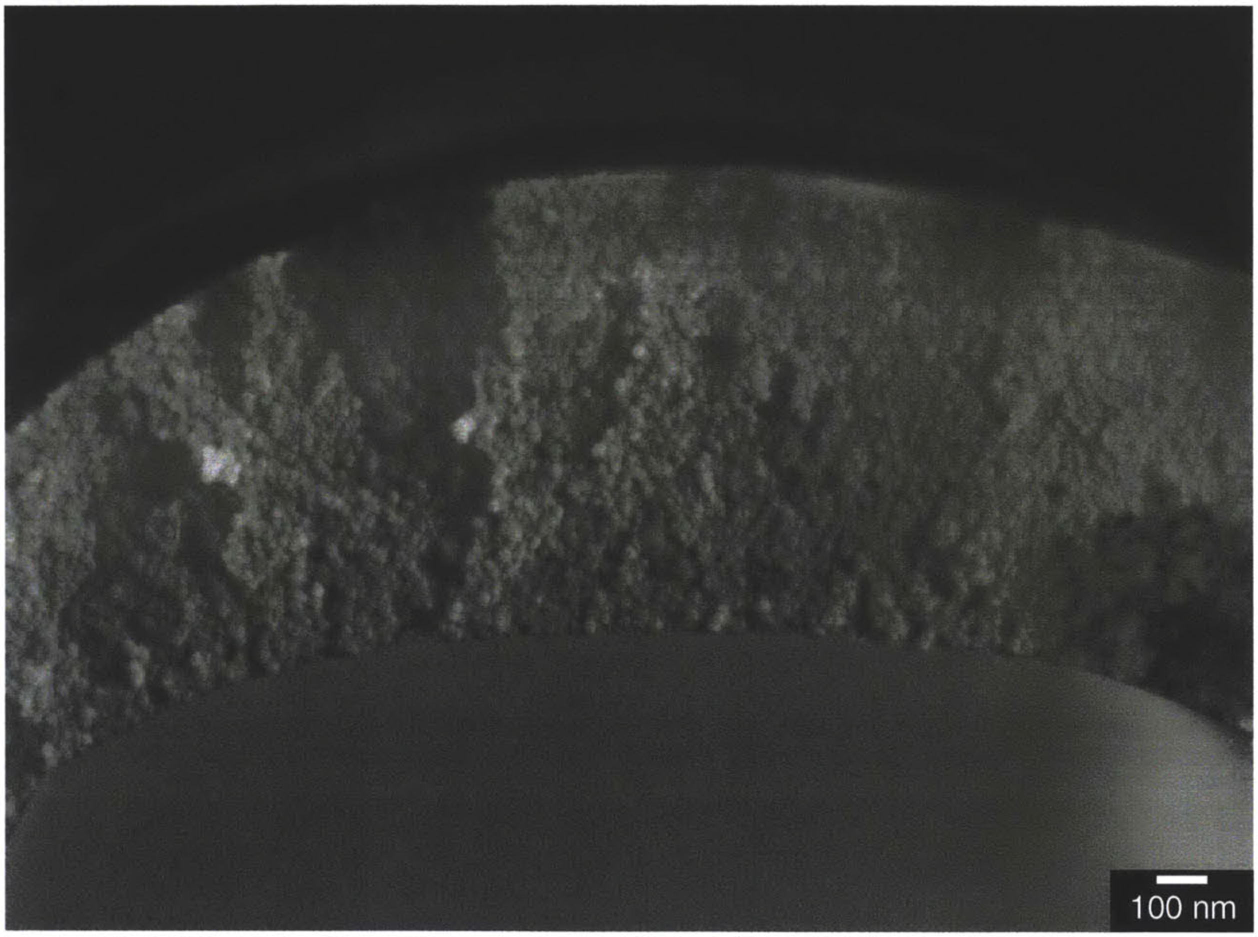

Figure 5-9 Highly magnified view of an 80 bilayer TiO_2/SiO_2 film deposited on a nanochannel array. The texture of the film and individual nanoparticles are clearly evident.

Carillo and Dobrynin have recently performed molecular dynamics simulations of all-nanoparticle LbL assembly in confined geometries.[124] They simulated the deposition of five bilayers of oppositely charged nanoparticles on substrates containing cylindrical pores which were 2.5, 5, and 7.5 times larger than the nanoparticles being deposited. Taking silica nanoparticles as a basis, these values correspond to 38, 65, and 113 nm pores in our system which is significantly smaller than the channels used here. Like us, they observed bridging of their pores, but at much lower film thicknesses due to their much smaller pores. They also found that slower growth occurs within the pores and that this growth plateaus as the pore becomes blocked. It is unclear from the fairly shallow pores they employed whether they, like us, see two distinct stages of growth within the pores: uniform, slow growth throughout the pore followed by bridging near the entrance of the pore.

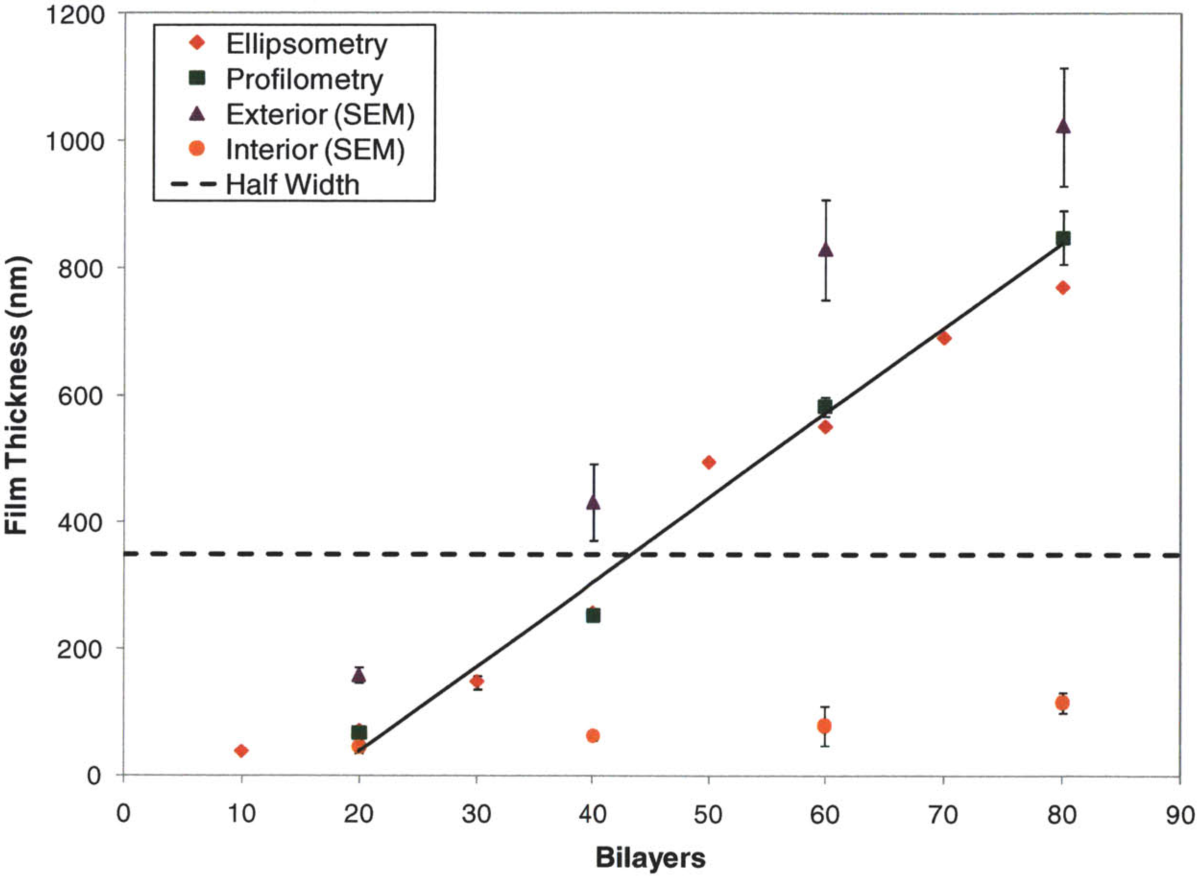

Figure 5-10 The thicknesses of TiO_2/SiO_2 multilayers deposited on planar silicon wafers and measured via ellipsometry and profilometry are compared with SEM measurements of multilayer thickness atop the posts (exterior) and on the walls of nanochannels (interior). The dashed line represents half the width of the nanochannel, the maximum film thickness achievable.

Their simulations do lead to a proposed mechanism for the bridging of the pores. Their simulations suggest that strings of positively charged and negatively charged nanoparticles form and that these aggregates bridge the pores. Their data show that nanoparticles desorb in pairs and that the resulting aggregates have more optimal electrostatic interactions than they had in the adsorbed state. This mechanism is qualitatively consistent with our results, showing that nanoparticles are particularly susceptible to desorption and that this results in aggregation and bridging of small pores or channels.

5.4 Conclusions

In this work we have demonstrated that LbL deposition of titania and silica nanoparticles in confined geometries results in conformal and uniform coverage of the channels and then reproducible, systematic bridging of the channel mouths. Films deposited on the confined channel walls were significantly thinner than those assembled on the unconfined tops of the posts. This is in agreement with theoretical and experimental results which show that electrostatic exclusion of depositing species is important for LbL deposition in extreme confinement or at low ionic strength. The bridging of the nanochannels was attributed to the weak adsorption of nanoparticles and to the ease with which they desorb to form large aggregates. Significant variability in film thickness over macroscopic distances was also observed, indicating that LbL deposition of nanoparticles is more sensitive to the local geometry than polymer/nanoparticle assembly.

This work provides a new route by which confined geometries can be coated with a nanoporous multilayer without the need for calcination. In addition, the systematic bridging of these channels is intriguing in that it results in the plugging of large nanochannels with a nanoporous layer. This unique geometry points to applications in selective separations wherein this porous layer could be deposited on an unselective, highly porous film. The thickness and functionality of the nanoparticle layer could be manipulated to provide high selectivity while preserving relatively high flux of the permeating species.

Chapter 6 Modification of Nanoporous Polymer Membranes for Selective Separations

6.1 Introduction

Although micro/nanofluidic devices have well-defined channels and are very useful for the fundamental study of LbL deposition in confinement, applications in large-scale separations problems demand much simpler, more readily available substrates. Consequently we have used commercial nanoporous polymer membranes with well-defined right cylindrical pores fabricated via etching of radiation tracks (see Section 2.2). One intriguing potential application of the electrolyte exclusion we observe while attempting LbL deposition is to build a membrane which selectively filters out ionic species. Such a filter could act as a reverse osmosis (RO) membrane for water desalination.

RO membranes currently used normally consist of a thin polyamide selective layer supported on a microfiltration or ultrafiltration membrane.[125] This asymmetric design allows for good mechanical strength due to the underlying porous membrane and good selectivity due to the thin selective layer. Since the membrane flux is inversely proportional to the membrane thickness, the selective layer should be as thin as possible while still achieving the desired selectivity. Many researchers and companies are active in this area since global desalination capacity is already over 40 million cubic meters per day and is expected to grow to over 60 million cubic meters per day by 2015.[125] Research in this area has already lead to steady improvements in flux from 43 L/m^2/bar/day in 1981 to 69 L/m^2/bar/day in 2005.[125]

Despite this, the selective layer is always very dense, and hence the membrane flux is severely compromised. If one could build a porous, highly charged selective layer that rejected ions without lowering the flux as drastically, its utility in desalination is clear. In this work, we have attempted to use our knowledge of LbL deposition of nanoparticles to construct a highly porous film which overcoats the pores of a track etched membrane. The interstices of the porous multilayer, which are on the same order as the nanoparticles that make up the porous layer, *i.e.* about 6 nm, are small enough that we may be able to get Debye layer overlap. Due to the high porosity, however, the water flux should be much higher than that of a typical RO membrane.

Many researchers have modified porous membranes with polymers in order to achieve selective separation of ions and some of them have used LbL assembly. For instance, Breuning's group uses canonical polyelectrolytes (*i.e.* PAH, PSS, PAA, PDAC) to coat underlying porous films consisting of anodized alumina, track etched polycarbonate, cellulose acetate, polyethersulfone, etc. Normally the objective is to show selectivity between monovalent and divalent and trivalent ions. The pH and ionic strength of assembly, chemical modification of the polyelectrolytes, and post assembly treatments such as cross-linking were used to tune the ion permeability and selectivity.[70,126-129] Others have also modified porous membranes specifically for use in reverse osmosis and nanofiltration.[130-133] In all of these cases, the films deposited were dense, selective polymer films which still significantly lower the permeation rate.

6.2 Experimental Section

Materials

PAH (M_w = 56,000) and PSS (M_w = 70,000) were purchased from Sigma-Aldrich. Titania nanoparticles (average particle size ~6 nm) were synthesized by hydrolysis of titanium tetraisopropoxide as described in detail elsewhere.[120] Silica nanoparticles (average particle size ~15 nm) were purchased from Sigma-Aldrich (Ludox HS-40, 40 wt%). TEPC membranes (Nuclepore, 0.2 μm) were purchased from Whatman.

LbL Assembly

DI water (18.2 MΩ·cm, Millipore Milli-Q) was used in all deposition solutions and rinse baths. The titania colloidal suspension was filtered using a 0.02 μm syringe filter (Anotop 25, Whatman) and diluted to 0.03 wt% with DI water adjusted to pH 1.5 using nitric acid. The silica suspension was filtered using a 0.2 μm syringe filter (Anotop 25, Whatman) and diluted to 0.03 wt% with DI water adjusted to pH 9 with 1 M NaOH. PAH and PSS solutions were dissolved in DI water to form 10 mM solutions (on a repeat unit basis) and their pH values were adjusted as desired using HCl and NaOH. Rinse baths consisted of DI water filtered using 0.2 μm polyether sulfone filtration membranes (VWR). TEPC membranes were mounted on custom built sample holders which suspended the membrane so that it was not touching the surface of the support. The membranes were affixed to these sample holders using transparent tape.

Automated LbL assembly was performed using a Zeiss slide stainer. Substrates were immersed in the cationic and anionic deposition solutions for 20 min followed by three intermediate rinsing steps of 2, 2, and 1 min. Every twenty bilayers, the deposition solutions and rinse solutions were exchanged for fresh ones. Upon completion of LbL assembly, samples were allowed to dry at ambient conditions.

Spin-assisted LbL assembly was performed using a StratoSequence VI spin dipper (nanoStrata Inc.). Substrates were immersed in the cationic and anionic deposition solutions for 15 min followed by three intermediate rinsing steps of 2, 2, and 1 min. The substrates were spun at 120 rpm during all deposition and rinsing steps. Every twenty bilayers, the deposition suspensions and rinse solutions were exchanged for fresh ones. Upon completion of LbL assembly, samples were allowed to dry at ambient conditions.

Spray-assisted LbL assembly was performed using an automated system purchased from Svaya Nanotechnologies Inc. This system consists of four atomizing nozzles which were actuated by solenoids under the control of a logic relay. The sequence and timing of nozzle actuation was programmed into the relay module using the Zelio Soft 2 software package (Schneider Electric). Deposition solutions were sprayed for 12 s followed by a 6 s delay to allow for draining of the solution from the substrate. Rinse solutions were sprayed for 20 s and also followed by a 6 s delay. Nitrogen gas at 30 psi was fed to the atomizing nozzles and the liquid flows were adjusted using the nozzle apertures. Deposition solutions were fed at about 18 mL/min and rinse solutions were fed at approximately 30 mL/min. During the rinse steps, two nozzles were used to rinse the substrates. A schematic of the spray coating apparatus is given in Figure 6-1.

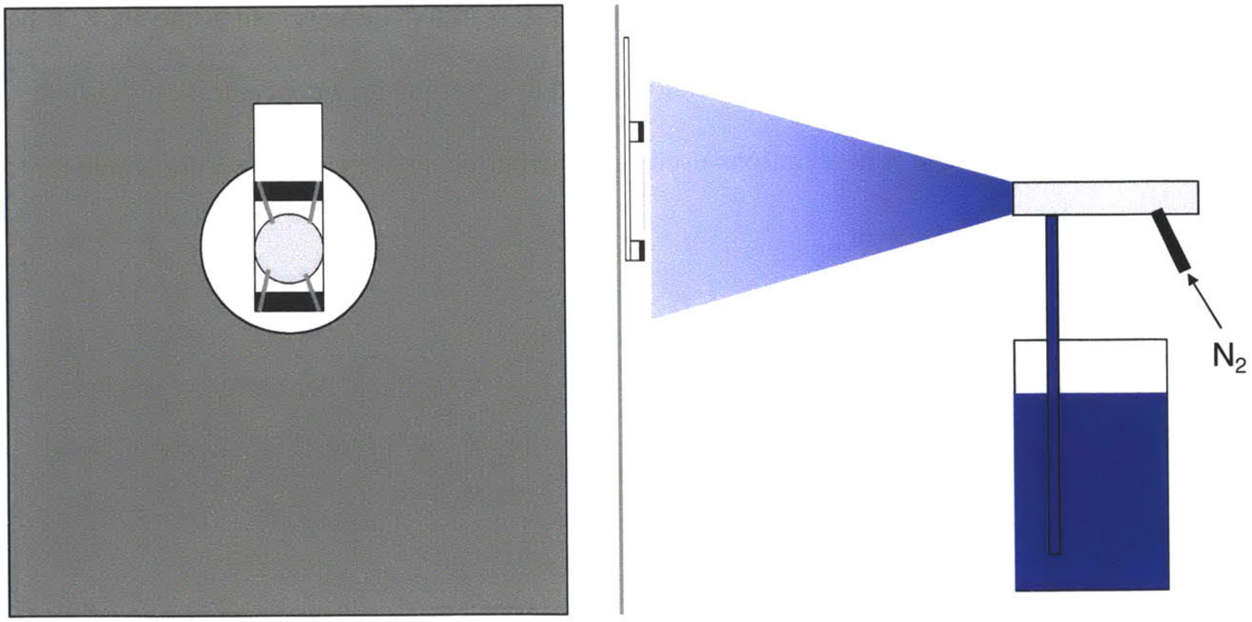

Figure 6-1 Schematic of spray LbL assembly apparatus. The sample is mounted on a metal plate which stands 20 cm from the atomizing nozzles. Nitrogen at 30 psi is used to atomize liquid fed from a reservoir as shown.

Characterization

Direct imaging of films assembled on TEPC membranes was carried out using SEM (JEOL 6320). Samples were sputter-coated with gold/palladium before imaging. The transport properties of coated membranes were determined by salt permeation measurements and by pressure-driven water permeation experiments.

To measure the salt permeation of these films, a custom-built diaphragm cell was designed and fabricated. A schematic of this apparatus is provided in Figure 6-2 and more detailed drawings are provided in Appendix B . The principle of this apparatus is quite simple: a solution of known concentration is placed on one side of the membrane and the concentration on the other side of the membrane is monitored as a function of time. The diaphragm cell consists of two magnetically-stirred compartments which are separated by a polymer membrane. The downstream cell initially contains pure DI water and a conductivity probe, which continuously measures the ionic conductivity (and therefore the salt concentration) of the downstream solution and prints it to the computer every 5 s. The upstream cell is initially empty, but at the start of the experiment a solution of known concentration is added to it, setting up a concentration gradient across the membrane. The concentrations used in our experiments were 0.6 M (comparable to seawater) and 10^{-3} M.

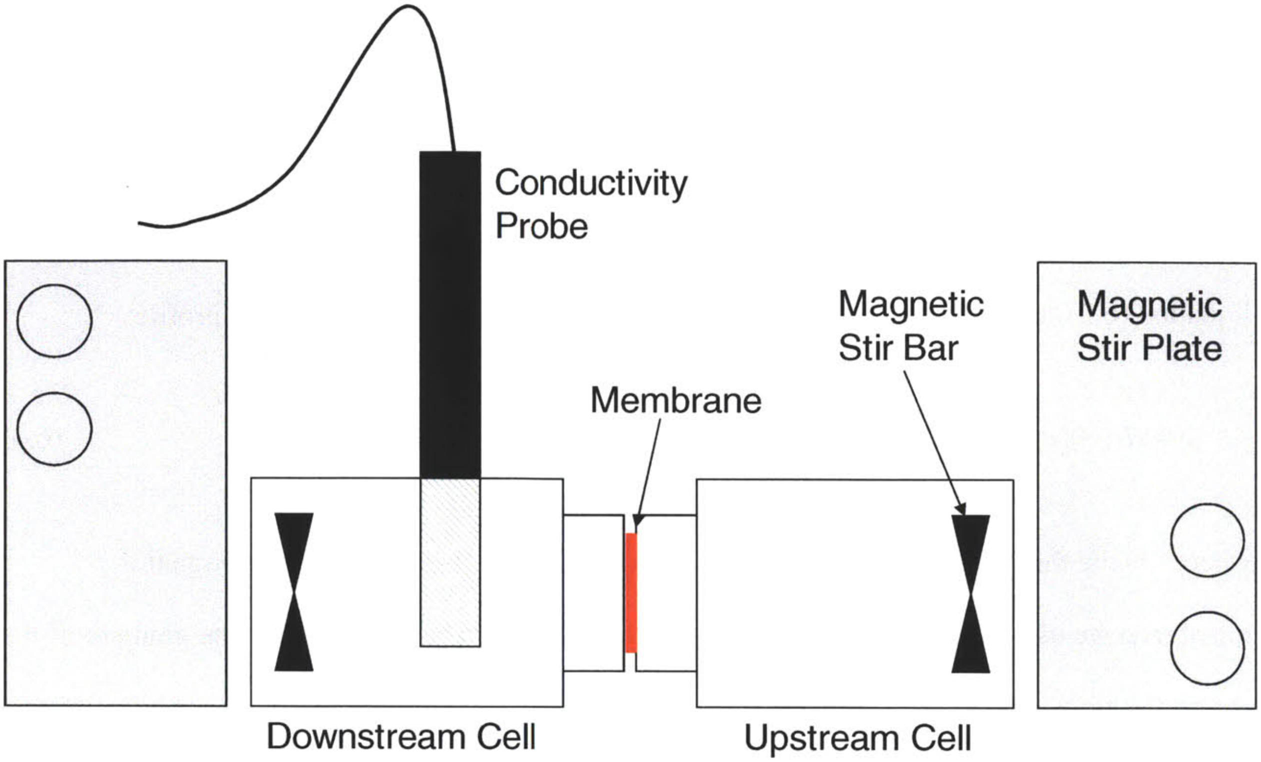

Figure 6-2 Schematic of custom-built diaphragm cell used to conduct ion permeation measurements. The membrane is sandwiched between two constantly-stirred aqueous solutions. Salt is injected into the upstream cell and the conductivity of the downstream cell is monitored to determine the rate at which salt permeates through the membrane.

To determine the permeance of the membrane of interest, we need to know how to extract this parameter from the data collected during the experiment *i.e.* the concentration in the downstream solution as a function of time. To do this, we need to calculate the concentration profile in the membrane. Fick's second law states that the change in concentration with time is proportional to the Laplacian of the concentration profile:

$$\frac{\partial c}{\partial t} = D\nabla^2 c \tag{6.1}$$

where c is the concentration of the substance of interest, t is time, and D is the diffusion coefficient. For one dimensional diffusion at steady state, this reduces to:

$$0 = D\frac{\partial^2 c}{\partial x^2} \tag{6.2}$$

The boundary conditions are simply that at each side of the membrane, the concentration is equal to the concentration in the adjacent solution multiplied by the partition coefficient H. Integrating Equation (6.2) subject to these boundary conditions gives a linear concentration profile:

$$c = Hc_0 + (c_\ell - c_0)\frac{H}{\ell}x \tag{6.3}$$

where ℓ is the thickness of the membrane. To determine the flux of a solute through this membrane we use Fick's first law which states that the flux j is proportional to the gradient of the concentration profile:

$$j = -D\nabla c \tag{6.4}$$

Combining Equations (6.3) and (6.4) we have:

$$j = \frac{DH}{\ell}(c_0 - c_\ell) \tag{6.5}$$

This result implicitly assumes that both the upstream and downstream concentrations are constant. Clearly this is not true in our case, however we can assume a pseudosteady state flux within the membrane and perform a mass balance on each compartment:

$$\begin{aligned} V_u\frac{dc_u}{dt} &= Aj = \frac{ADH}{\ell}(c_d - c_u) \\ V_d\frac{dc_d}{dt} &= -Aj = \frac{ADH}{\ell}(c_u - c_d) \end{aligned} \tag{6.6}$$

where V_u and V_d are the volumes of the upstream and downstream compartment respectively. Subtracting these two equations gives:

$$\frac{d(c_u - c_d)}{dt} = Aj\left(\frac{1}{V_u} + \frac{1}{V_d}\right) = \frac{ADH}{\ell}\left(\frac{1}{V_u} + \frac{1}{V_d}\right)(c_d - c_u) \tag{6.7}$$

The solution to this differential equation is simply an exponential subject to the initial condition that the concentration difference starts at a particular known value.

$$\ln\frac{c_{u0} - c_{d0}}{c_u - c_d} = -\frac{ADH}{\ell}\left(\frac{1}{V_u} + \frac{1}{V_d}\right)t \tag{6.8}$$

From this equation, it is clear that if we monitor the concentrations of the upstream and downstream cell, the only remaining unknowns are the diffusion coefficient and the partition coefficient. The product of these two parameters is the permeability, thus we can determine this important property from Equation (6.8). If we further assume that the initial downstream concentration is zero and that the experiment is quick enough that the change in the upstream concentration is small, we have:

$$\ln\frac{c_{u0}}{c_{u0} - c_d} = -\ln\left(1 - \frac{c_d}{c_{u0}}\right) = -\frac{ADH}{\ell V_d}t \tag{6.9}$$

Since the downstream concentration is much lower than the initial upstream concentration for a short experiment where the upstream concentration is unchanged, the logarithm can be approximated as:

$$\ln\left(1 - \frac{c_d}{c_{u0}}\right) \approx \frac{c_d}{c_{u0}} \tag{6.10}$$

Finally, we are left with a linear breakthrough curve whose slope is proportional to the permeability and known constants:

$$c_d = \frac{c_{u0} ADH}{\ell V_d} t \tag{6.11}$$

Permeability is an intrinsic property of a material and is therefore independent of the thickness of the membrane. For asymmetric membranes that are not uniform along the thickness dimension, a more useful measure is the permeance, which is the permeability divided by the film thickness:

$$P = \frac{m V_d}{A c_{u0}} \tag{6.12}$$

where m is the slope of the experimentally-measured breakthrough curve. An example of a breakthrough curve is provided in Figure 6-3. As shown in the figure, eventually the linear approximation breaks down and the slope of the data starts to decrease, but the initial data quite clearly are well approximated by a linear function. For more details on the data collection and analysis, see Appendix C

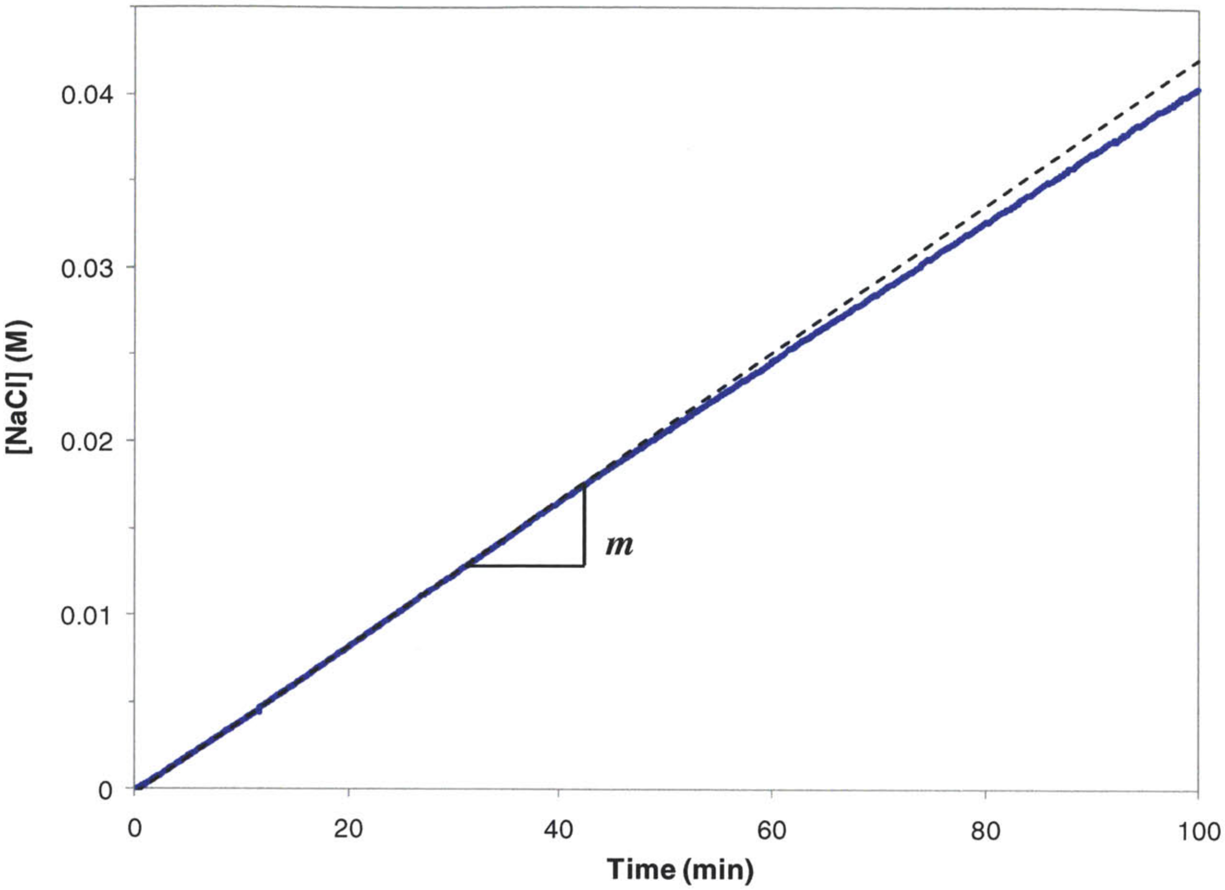

Figure 6-3 Representative breakthrough curve in which the concentration of NaCl in the downstream cell is measured as a function of time (blue line). The dashed line is a linear best fit of the initial slope and is used to calculate the permeance of the membrane.

To measure the permeation of water through these membranes, a dead end filtration cell was used. In this experiment, a membrane is mounted in the dead end filtration cell which is then attached to a pressurized dispensing vessel. The volume of water exiting the cell was then measured as a function of time and of pressure. A schematic of this apparatus is given in Figure 6-4.

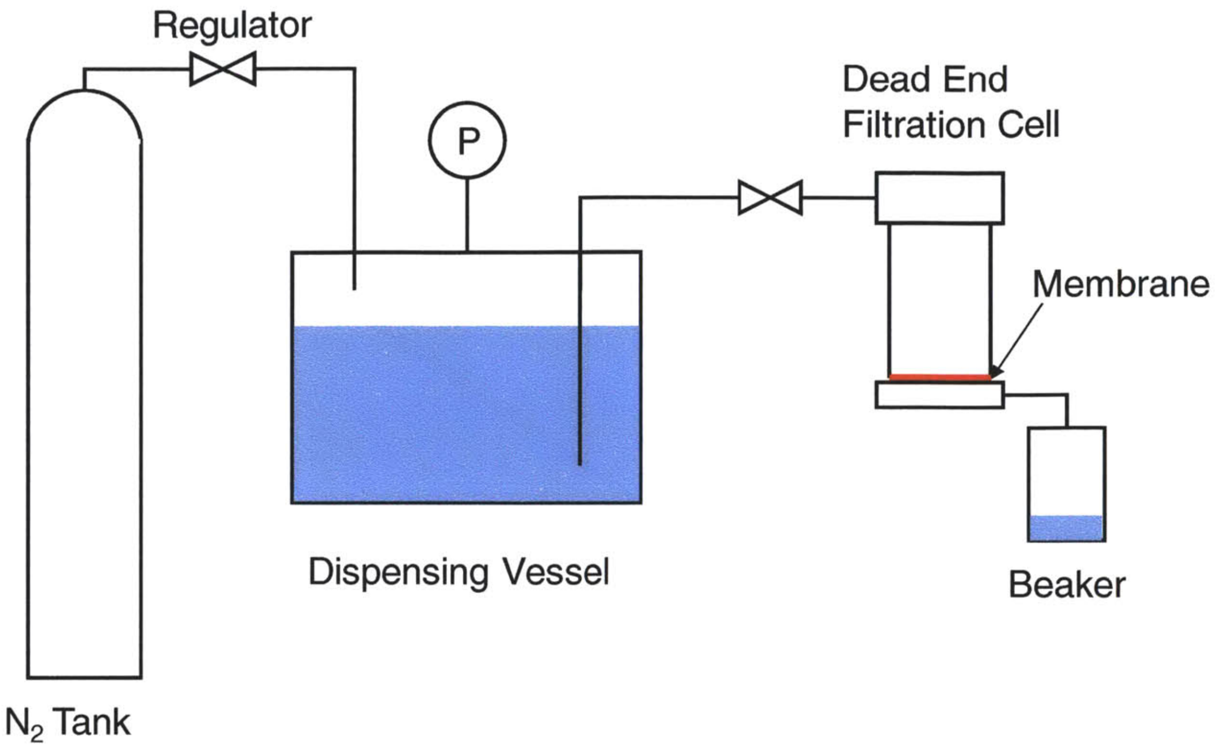

Figure 6-4 Schematic of the dead end filtration apparatus that was used to measure the water permeance of modified TEPC membranes. Water is driven through the membrane under pressure and the volume of water which passed through the membrane was measured as a function of time.

Since a TEPC membrane contains straight cylindrical pores, we model fluid flow through this membrane using the Hagen-Poiseuille equation. For each pore we have:

$$Q = \frac{\pi d^4 \Delta p}{128 \mu \ell} \tag{6.13}$$

where Q is the volumetric flow rate, d is the diameter of the pore, Δp is the pressure drop across the pore, μ is the viscosity of the fluid, and ℓ is the length of the pore which in our case also happens to be the thickness of the membrane. The number of pores in a given membrane area A is:

$$n_p = \frac{\phi A}{\frac{\pi}{4} d^2} \tag{6.14}$$

where ϕ is the void fraction in the polymer membrane. The volumetric flow for n_p pores is therefore:

$$Q = \frac{Ad^2\phi\Delta p}{32\mu\ell} \tag{6.15}$$

The analog of permeance water permeation is the superficial velocity (*i.e.* the flux) divided by the driving force (the pressure drop):

$$\frac{v}{\Delta p} = \frac{Q/A}{\Delta p} = \frac{d^2\phi}{32\mu\ell} \tag{6.16}$$

6.3 Two Simple Models for Transport in TEPC Membranes

To guide analysis of our results, simple models were developed for ion and water permeation within coated TEPC membranes. The first and simpler model describes how transport through the membrane changes as the pores are narrowed as is the case for conformal coating of the pore walls with PAH and PSS. The second model deals with the case in which a nanoporous skin is formed over the top of the TEPC membrane as in the case of TiO_2/SiO_2 and PAH/SiO_2. These two models are presented schematically in Figure 6-5. In both cases the membrane is assumed to be impermeable with the exception of the pores. The PAH/PSS membrane is also assumed to be impermeable as are the nanoparticles which make up the nanoporous multilayers. Changes in permeability due to double layer overlap and other electrostatic considerations are also completely ignored.

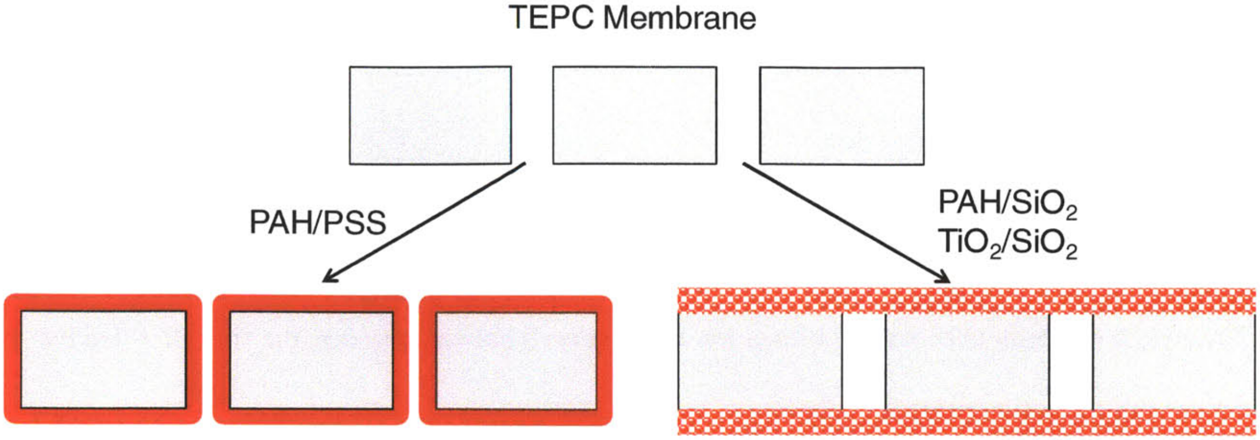

Figure 6-5 Schematic diagram of the two models considered here. The first assumes narrowed pores based on conformal coating of the nanochannels and the second assumes a nanoporous multilayer which covers the pores.

6.3.1. Transport in Narrowed Pores

Starting with Equation (6.5) above we know that the salt permeance is given by:

$$P_{NaCl} = \frac{j}{\Delta c} = P_0 \phi \tag{6.17}$$

where P_0 is the permeance of an open pore of length ℓ. The void fraction of the composite membrane is the initial void fraction multiplied by the reduction due to narrowing of the pores, therefore we have:

$$P_{NaCl} = P_0 \phi_0 \left(\frac{d}{d_0} \right)^2 = \frac{P_0 \phi_0}{d_0^2} d^2 \tag{6.18}$$

where ϕ_0 is the void fraction of the uncoated membrane and d and d_0 are the diameters of the coated and uncoated pore respectively. For pressure driven flow in cylindrical pores we start with Equation (6.16) and again substitute for the void fraction:

$$P_{H_2O} = \frac{v}{\Delta p} = \frac{\phi d^2}{32 \mu \ell} = \frac{d^2}{32 \mu \ell} \phi_0 \left(\frac{d}{d_0} \right)^2 = \frac{\phi_0}{32 d_0^2 \mu \ell} d^4 \tag{6.19}$$

The ratio of these two permeances is:

$$\frac{P_{NaCl}}{P_{H_2O}} = \frac{32\mu\ell P_0}{d^2} \tag{6.20}$$

This shows that as the pores narrow, the water permeance decreases more quickly than the ion permeance. The only parameter in this expression which is not constant is the pore diameter *d*. Eliminating the pore diameter by solving Equation (6.19) for *d* and substituting into Equation (6.18) we have:

$$P_{NaCl} = \frac{P_0\phi_0}{d_0^2} d^2 = \frac{P_0\phi_0}{d_0^2}\sqrt{\frac{32\mu\ell P_{H_2O}}{\phi_0}} d_0 = \frac{P_0}{d_0}\sqrt{32\phi_0\mu\ell P_{H_2O}} \tag{6.21}$$

This expression shows that the ion permeance scales as the square root of the water permeance and thus a log-log plot of P_{NaCl} vs. P_{H2O} should have a slope of 0.5. The remaining parameters in this expression are all constants.

6.3.2. Transport in Covered Pores

For covered pores, we must calculate the effective diffusion coefficients in the porous layer and in the pore. Assuming the spheres are impermeable to salt, the reduction in the diffusion coefficient for the nanoparticle coating is given by:[134]

$$\frac{D_{coating}}{D_0} = \frac{\varepsilon}{1 + \frac{1-\varepsilon}{2}} = \frac{2\varepsilon}{3-\varepsilon} \tag{6.22}$$

where D_0 is the diffusion coefficient in the continuum (water), $D_{coating}$ is the diffusivity in the porous coating, and ε is the void fraction of the polymer/nanoparticle or nanoparticle/nanoparticle coating. Putting this resistance in series with the resistance due to the TEPC film we have:

$$P_{NaCl}=\frac{j}{\Delta C}=\frac{1}{\frac{\ell_{TEPC}}{D_{TEPC}}+\frac{2\ell_{coating}}{D_{coating}}}=\frac{1}{\frac{\ell_{TEPC}}{D_0\phi}+\frac{2\ell_{coating}(3-\varepsilon)}{2D_0\varepsilon}}=\frac{D_0}{\frac{\ell_{TEPC}}{\phi}+\frac{2\ell_{coating}(3-\varepsilon)}{2\varepsilon}} \tag{6.23}$$

where ℓ_{TEPC} is the thickness of the TEPC membrane and $\ell_{coating}$ is the thickness of the nanoparticle coating. In writing it this way we have implicitly assumed that H is 1 which is very reasonable for a porous film. Pressure driven flow in a packed bed is given by the Blake-Kozeny equation:

$$\frac{v}{\Delta p}=\frac{d_p^2\varepsilon^3}{150\mu L(1-\varepsilon)^2} \tag{6.24}$$

where d_p is the diameter of the nanoparticles. Combining this result with Equation (6.16) as resistances in series and assuming that the particles coat only the top and bottom of the film and not the pores, we have for the composite membrane:

$$P_{H_2O}=\frac{1}{\frac{32\mu\ell_{TEPC}}{\phi d^2}+\frac{300\mu\ell_{coating}(1-\varepsilon)^2}{d_p^2\varepsilon^3}} \tag{6.25}$$

The ratio of these permeances is therefore:

$$\frac{P_{NaCl}}{P_{H_2O}}=\frac{\frac{32\mu\ell_{TEPC}}{\phi d^2}+\frac{300\mu\ell_{coating}(1-\varepsilon)^2}{d_p^2\varepsilon^3}}{\frac{\ell_{TEPC}}{\phi}+\frac{2\ell_{coating}(3-\varepsilon)}{2\varepsilon}}D_0 \tag{6.26}$$

Again we are left with one parameter that is not constant, the thickness of the nanoparticle coating. Solving Equation (6.25) for $\ell_{coating}$ and substituting the result into Equation (6.23) we obtain:

$$P_{NaCl} = \frac{D_0}{\frac{\ell_{TEPC}}{\phi} + \frac{2\ell_{coating}(3-\varepsilon)}{2\varepsilon}} = \frac{D_0}{\frac{\ell_{TEPC}}{\phi} + \frac{\left(\frac{1}{P_{H_2O}} - \frac{32\mu\ell_{TEPC}}{\phi d^2}\right) d_p^2 \varepsilon^2 (3-\varepsilon)}{300\mu(1-\varepsilon)^2}} \tag{6.27}$$

For this complicated expression, it is instructive to look at the limiting behavior. If the nanoporous film is the limiting resistance the above expression reduces to:

$$P_{NaCl} = \frac{300 D_0 \mu (1-\varepsilon)^2 P_{H_2O}}{d_p^2 \varepsilon^2 (3-\varepsilon)} \tag{6.28}$$

Thus a log-log plot of P_{NaCl} vs. P_{H2O} should have a slope of 1. If, however, the membrane itself is limiting, Equation (6.27) reduces to:

$$P_{NaCl} = \frac{D_0 \phi_0}{\ell_{TEPC}} \left[\frac{150(1-\varepsilon)^2}{150(1-\varepsilon)^2 - 16\ell_{TEPC} d_p^2 \varepsilon^2 (3-\varepsilon)} \right] \tag{6.29}$$

This expression is simply a collection of constants and our ion permeance is therefore independent of the water permeance, meaning a log-log plot of P_{NaCl} vs. P_{H2O} should have a slope of 0.

6.4 Results and Discussion

Our first efforts focused on using the PAH/PSS polyelectrolyte pair deposited at pH 4 with 0.1 M NaCl. Since we have extensively studied this system, it provides a convenient baseline from which to start. Multilayers of increasing thickness were assembled in the pores of TEPC membranes and the permeation measured as described above. Normalized permeance data are shown in Figure 6-6 and compared to the volume reduction of the pores. The volume reduction was calculated based on the thicknesses of swelled, confined multilayers measured in Section

3.3. The data show that the permeance of the films to 0.6 M NaCl is essentially unchanged after twenty bilayers. Although at low bilayers, the permeability is lower than predicted by the volume occluded, eventually the prediction catches up to and surpasses the experimental value. This residual permeability of about 10% of the initial value indicates that either there is a residual gap that cannot be filled or that the polymer itself has an appreciable permeability to salt ions. In any case, continuing to coat the pores beyond about 20 bilayers does not result in significant gains in ion permeance.

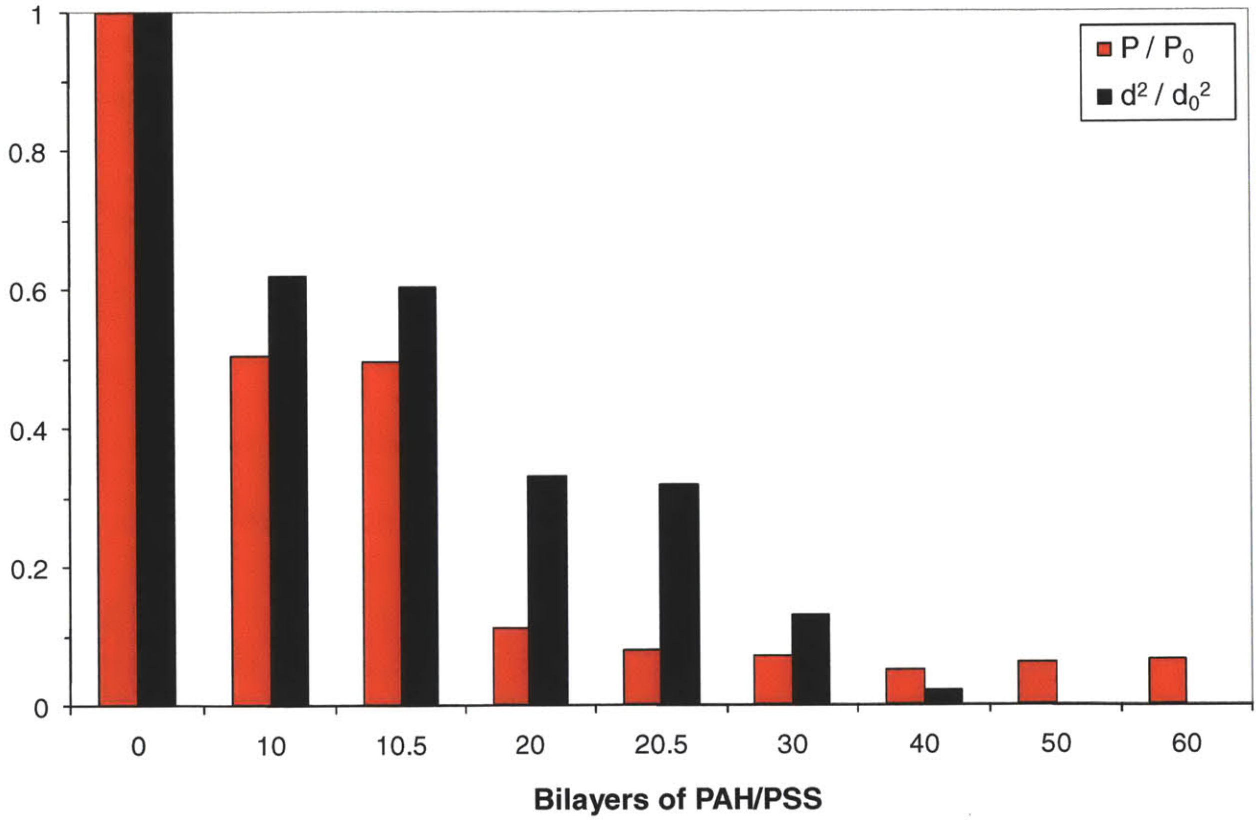

Figure 6-6 Normalized 0.6 M NaCl permeance values for TEPC membranes coated with increasing amounts of PAH/PSS assembled at pH 4 with 0.1 M NaCl. These values are compared with the permeance reduction expected based solely on the loss of pore volume due to polyelectrolyte deposition.

The 10.5 and 20.5 bilayer experiments were performed to see whether the surface charge affected the transport properties. These films were topped with PAH and therefore have positive surface charge instead of the negative surface charge present in whole bilayer samples. The results show that the surface charge does not significantly affect the ion permeance of these composite membranes.

To compare these results with commercially available reverse osmosis membranes, similar experiments were performed on Filmtec RO membranes obtained from Dow Water. As is shown in Figure 6-7, this residual permeance observed for PAH/PSS-modified membranes is still approximately two orders of magnitude higher than what one would expect for a conventional RO membrane. For the films for which we have data, it is also interesting to note that the permeance appears to be independent of solute concentration. This is a discouraging finding since in our fundamental studies of LbL deposition, we find that the ionic strength plays a critical role in determining whether and to what extent film growth occurs. Consequently, one would expect that the charge-based exclusion which is responsible for retarding film growth within the channel would also inhibit salt ions, therefore lowering the salt permeance.

A major problem with using polyelectrolyte multilayers to modify a porous membrane is the fact that the polymer forms a dense layer which not only lowers the ion flux, but also drastically reduces the water flux. We hoped to suppress this effect by fabricating porous films made by utilizing nanoparticles in the deposition. Our first attempts focused on TiO_2/SiO_2 deposited at pH 1.5 and 9 respectively. Spray coating was used instead of conventional dipped LbL assembly because this method has been shown to encourage bridging of porous structures.[89] Micrographs of one of the resulting films are given in Figure 6-8. As these micrographs clearly show, little to no bridging was observed and the pore diameters appeared to be essentially unchanged. To encourage bridging, we decided to try a polymer/nanoparticle system: PAH/SiO_2 deposited at pH 7.5 and 9 respectively.

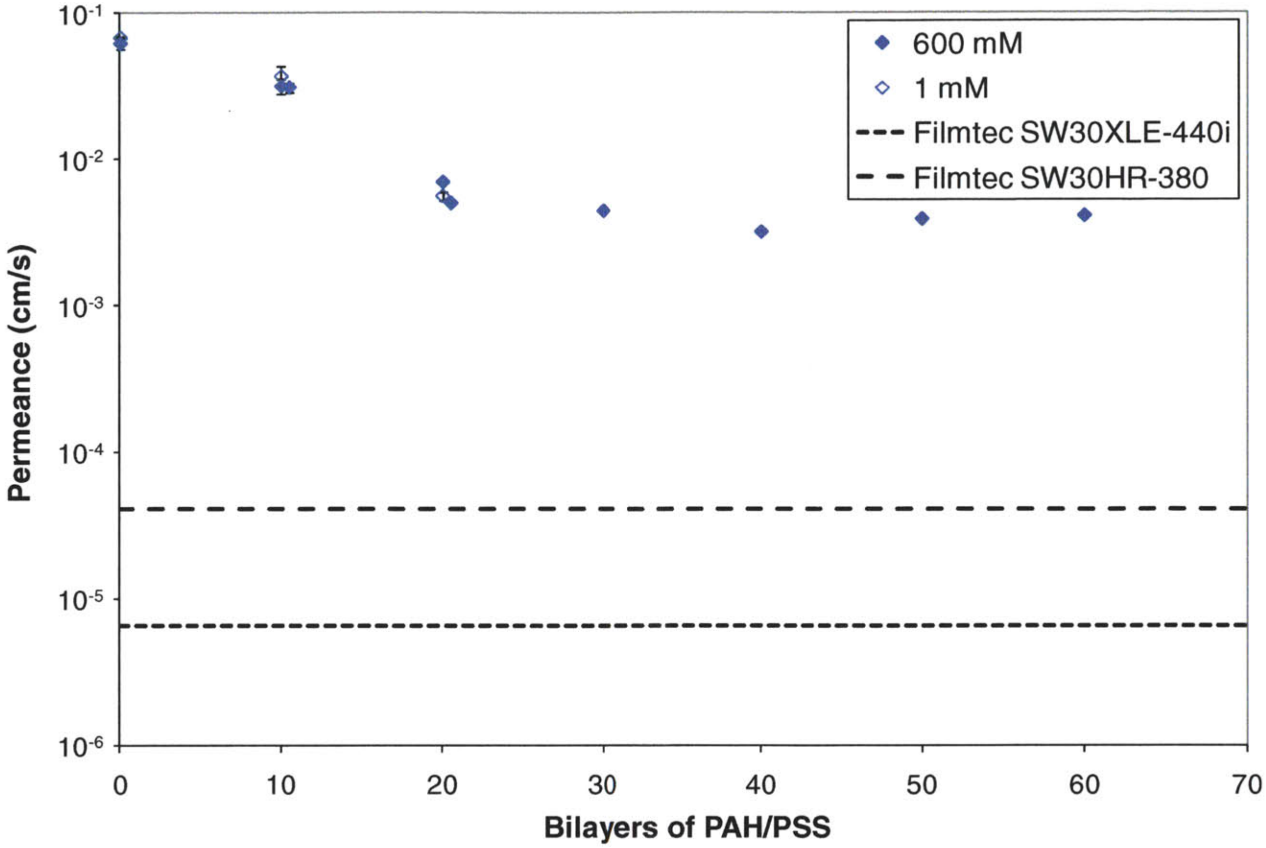

Figure 6-7 Membrane permeance as a function of the number of bilayers deposited on a TEPC film. The dashed lines represent commercially available RO membranes. Two values of the initial upstream concentration were used in order to determine whether permeation was dependent on the ionic strength of the upstream solution.

This combination is also porous, but is much more stable due to the presence of flexible, charged PAH chains. Micrographs of films spray-coated with this pair are given in Figure 6-9. As these images show, the pores are clearly smaller after 20 bilayers and are almost completely covered after 40 bilayers. The 60 bilayer film has marginally more complete coverage, though there are still visible defects such as pinholes and cracks. The close-up view of the 60 bilayer film shows individual nanoparticles and suggests that the film does exhibit significant porosity.

Ion transport measurements were carried out on a series of these films to determine whether this new porous structure would serve as a better ion barrier. The results are given in Figure 6-10 and are once again compared with those for commercially available RO membranes.

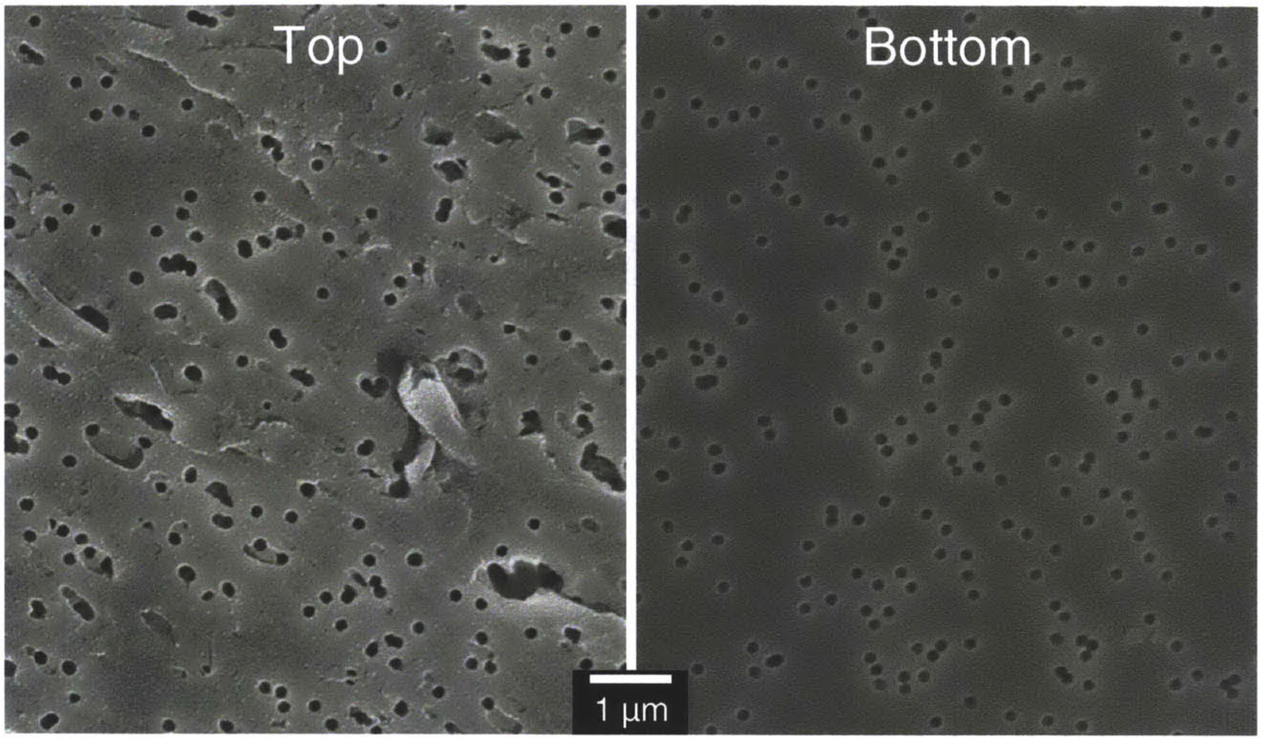

Figure 6-8 Micrographs showing a 20 bilayer TiO_2/SiO_2 spray-coated film assembled at pH 1.5 and 9 respectively on a TEPC membrane with 200 nm pores.

The data show that these modified membranes exhibit very little change in permeance even as fairly thick multilayers of PAH/SiO_2 are deposited on them. The permeance values are around three orders of magnitude higher than those observed for the Filmtec RO membranes. This could be due to a number of factors including defects or an absence of sufficient charge within the multilayer to act as an effective barrier. It is clear from the above micrographs that the composite multilayer coating does have defects such as cracks which might serve as shunts for solute moving through the film. It is also not clear that we have complete bridging of all pores, although we certainly have more bridging than was observed in the spin-assisted dipped LbL deposition of polymer/nanoparticle combinations on nanochannels substrates.

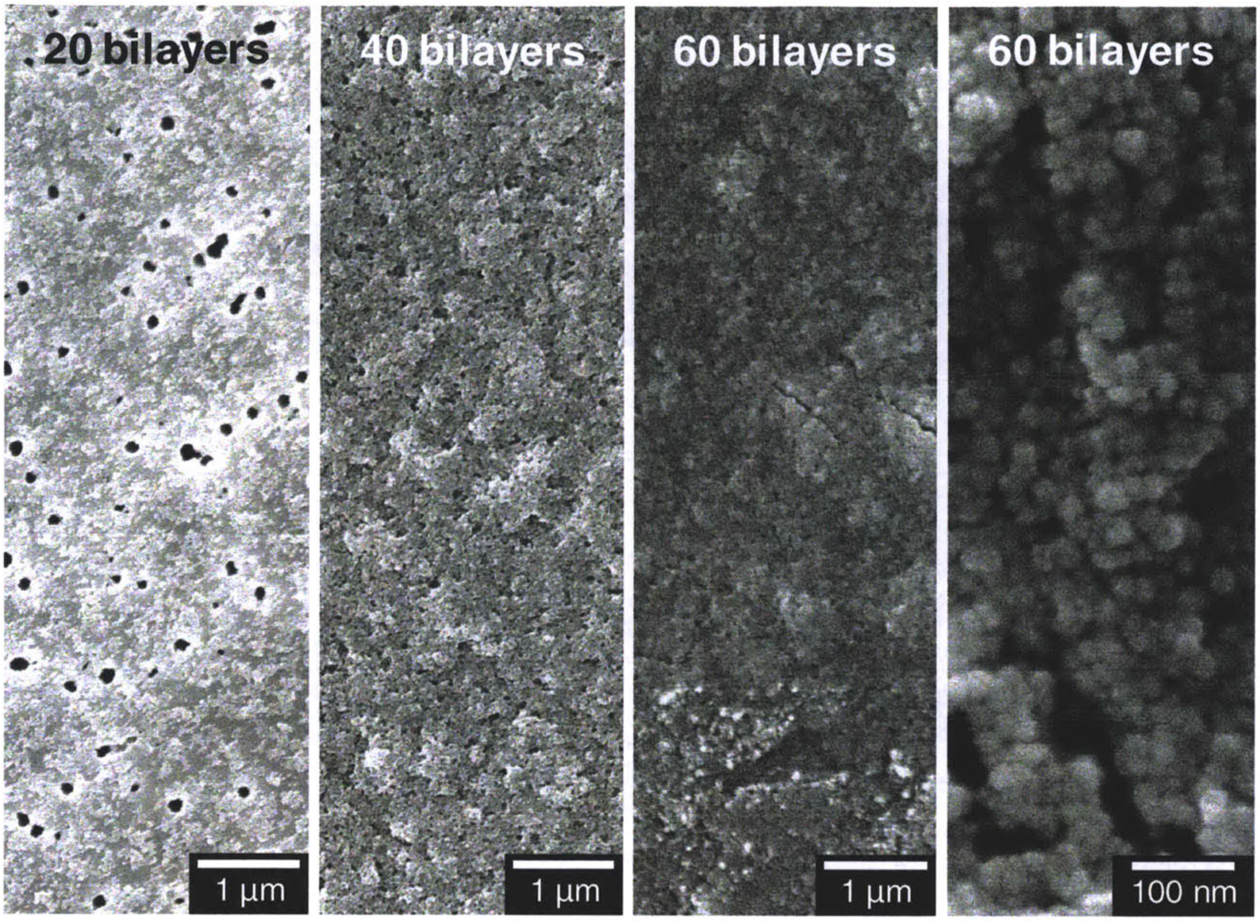

Figure 6-9 Micrographs showing PAH/SiO_2 multilayers spray-coated onto TEPC membranes with 200 nm pores.

The water permeance of these films was also measured to compare their performance with commercially available membranes. The results of these experiments are given in Figure 6-11. As the data show, our expectation that a porous nanoparticle-containing multilayer would allow higher fluxes than conventional RO membranes is borne out experimentally. These films have well over an order of magnitude higher permeance than the commercial Filmtec membranes. Of interest is the fact that most of the drop in water permeance occurs within the first twenty bilayers; after this point, it decreases much more slowly. The polymer-coated films, which we expect to fill in the pores rather than bridging them, show significantly lower fluxes as expected. Like the nanoparticle-coated films, the permeance decreases quickly, but to a lower value on par with the commercial membranes after just thirty bilayers.

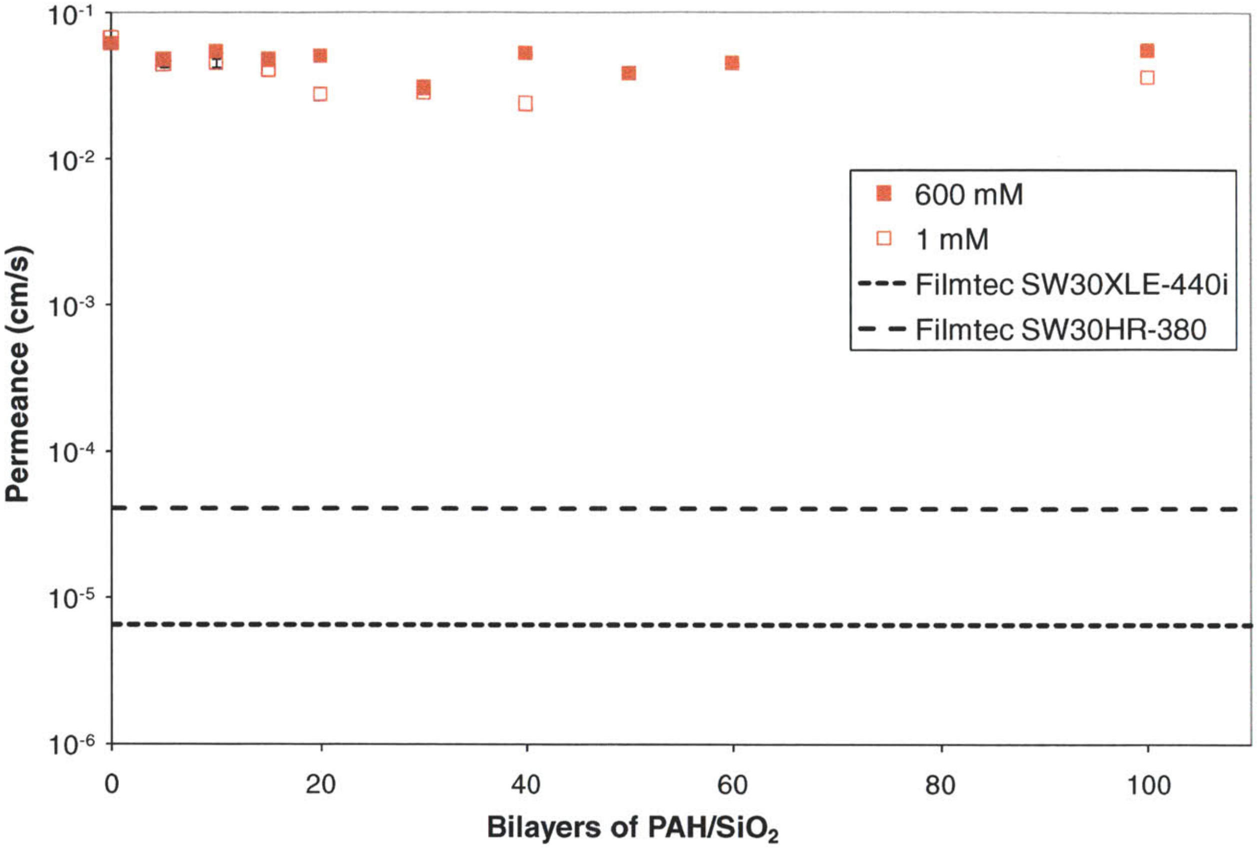

Figure 6-10 Permeance of TEPC membranes modified by LbL deposition of PAH/SiO_2. The dashed lines represent commercially available RO membranes.

To understand the tradeoff between low ion flux and high water flux, we plotted the ion permeance against the water permeance for both our modified TEPC systems and the commercial Filmtec membranes in Figure 6-12. As the data show, the commercial membranes significantly outperform our modified TEPC membranes. These data are compared with the models proposed in Section 6.3. Once again, these models assume that all surfaces are completely uncharged.

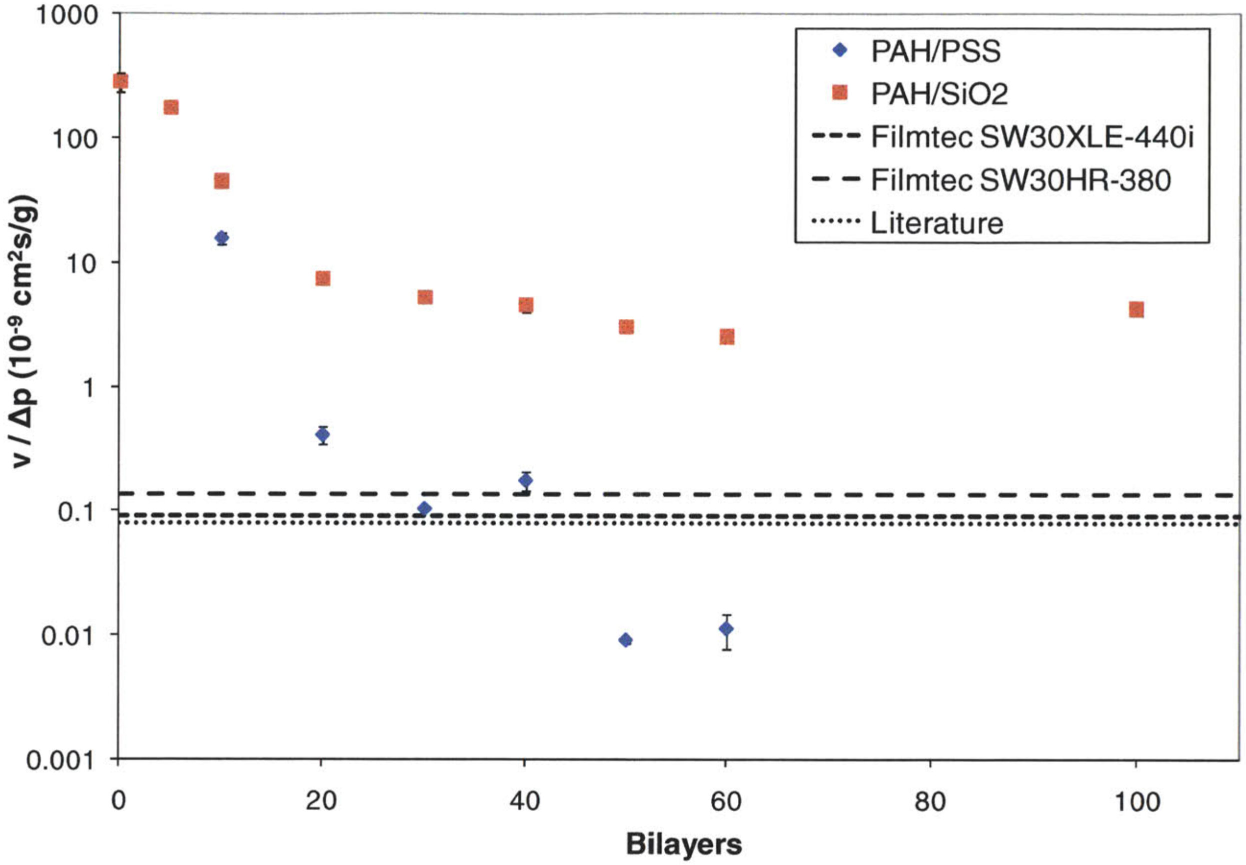

Figure 6-11 Water permeance (superficial velocity divided by pressure drop) as a function of the number of bilayers of (PAH/PSS) (pH 4.0, 0.1 M NaCl) and (PAH/SiO_2) (pH 7.5/9.0) deposited. The dashed lines represent commercially available RO membranes and values quoted in the literature.[125]

As the data show, our experiments are no better than the models produced, meaning we are not seeing the benefits of exclusion due to charged surfaces or at the very least those benefits are being overwhelmed by other detrimental effects. The PAH/PSS data show a slope of about 0.3 compared with the theoretical slope of 0.5. The PAH/SiO_2 data do agree fairly well with our theoretical prediction. We are for the most part within the regime in which the underlying membrane is the limiting resistance and our slope of 0.06 is quite close to the theoretical slope of 0 for this parameter space. All of this seems to indicate that the charge present within the pores or in a thin skin on top of the membrane is not having an appreciable effect on the ion transport properties of these composite membranes at the conditions investigated. This may be due to the screening effect of salt at 0.6 M where the Debye length is just 4 Å, but the data for 1 mM where the Debye length is close to 10 nm show little discernable difference from those at 0.6 M. Additionally it could be that defects within the film overwhelm any exclusion of ions due to surface charge.

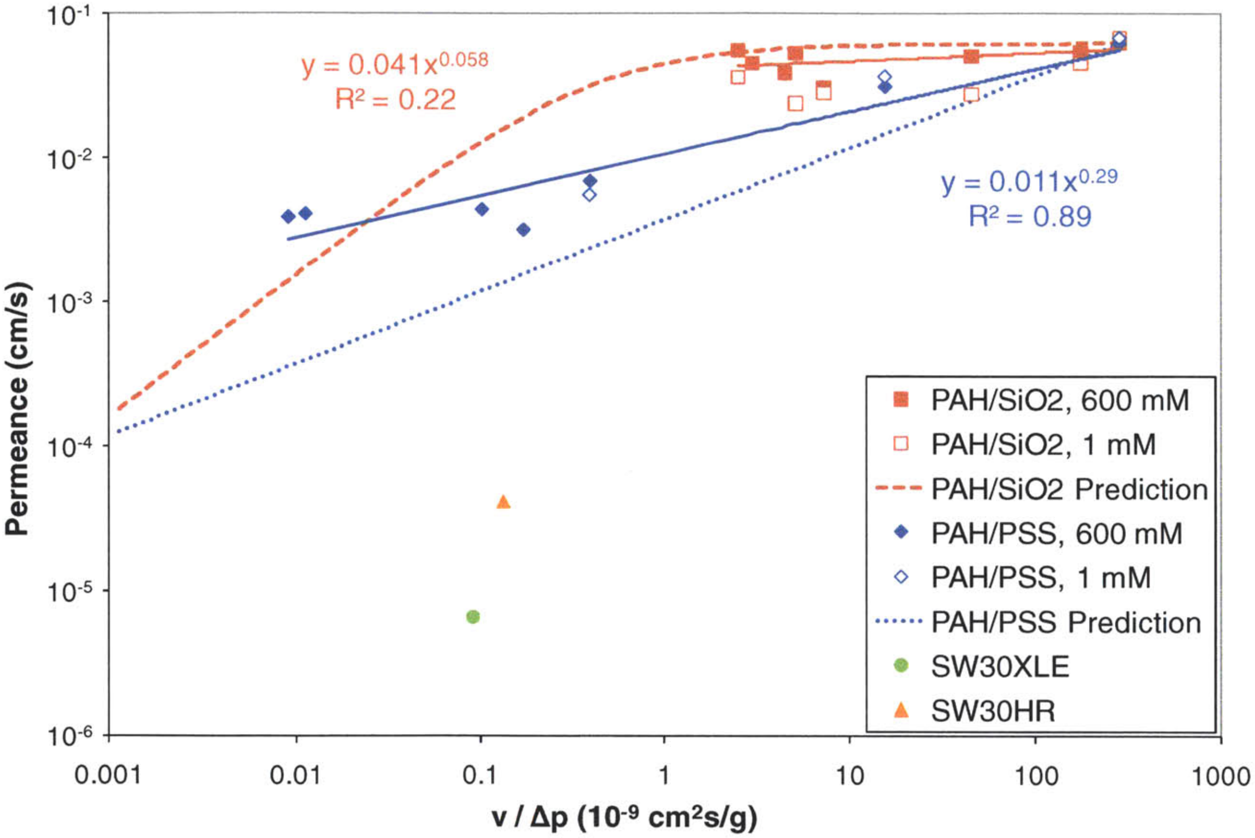

Figure 6-12 Ion permeance as a function of water permeance for a series of modified TEPC membranes and two commercially available RO membranes. The dashed lines represent predictions from simple models which assume no charge-based effects and the solid lines represent best fits of the 600 mM data.

6.5 Conclusions

In this work we have attempted to apply the knowledge gained in the fundamental study of LbL assembly in confined geometries to the formation of a nanoporous skin layer for ion rejection. We have experimented with three different combinations of nanoparticles and polymers to explore how the modification of TEPC membranes affects the ion and water flux through the composite membrane. Two simple models were proposed to explain our results. The first, which describes the conformal coating of the pore walls with impermeable polymer, predicts that for every order of magnitude drop in ion permeance achieved, a drop in water flux of two orders of magnitude is required. The second model describes the coating of a porous substrate with a porous bed of nanoparticles which do not appreciably penetrate the pores. This model predicted two regimes: the membrane-controlled regime in which the ion and water permeances are independent and the coating-controlled regime in which their relationship is linear. Our data show that in the first case the ion permeance scales as the 0.3 power of water permeance. In the second case, our data agree well with the model, but that we are firmly in the membrane-controlled regime.

Comparisons between our composite membranes and commercial RO membranes show that our ion permeance values are over an order of magnitude higher for PAH/PSS and nearly three orders of magnitude higher for PAH/SiO_2. The PAH/SiO_2-coated films do show at least one order of magnitude higher water permeance than commercially available films. As a whole, our results indicate that either ion exclusion is not occurring in these systems or it is being overwhelmed by other factors such as film defects.

Chapter 7 Summary and Future Work

7.1 Summary

In this thesis, the layer-by-layer assembly of polyelectrolytes and charged nanoparticles in confined geometries was studied from a fundamental perspective and in terms of applying that knowledge towards applications. We started with a brief introduction to polymer physics, discussing how the configuration of a molecule in solution affects the way that it adsorbs onto a surface. Two parameters which give us control over the conformation of a polyelectrolyte were then discussed, namely the pH for weak polyelectrolytes and ionic strength for all polyelectrolytes. Layer-by-layer assembly was then introduced as a general directed assembly method by which any combination of macromolecular or colloidal materials with complementary functionalities could be incorporated into a finely structured film.

Substrates containing geometrically confined pores or channels were discussed next. The fabrication of nanochannel arrays and hybrid micro/nanofluidic devices which were used as substrates for most of the fundamental investigations in this work was described in detail. Polymeric membranes with well-defined cylindrical pores were also discussed as a platform for our work on applications in separations. Additionally, the special considerations which arise due to the electrostatic environment in confined geometries were introduced. In particular, we described the exclusion of charge-bearing species from narrow channels which have charged surfaces as well as the role of ionic strength in mediating this effect.

Having laid the groundwork for our experimental investigations, we moved on to discuss the LbL assembly of polyelectrolytes in confined nanofluidic arrays. We proved that PAH/PSS multilayers form conformal, uniform coatings throughout the high aspect ratio channels and measured the film thicknesses within and outside the channel for comparison with films deposited on planar surfaces. We found that confined multilayers are systematically thinner than those deposited on flat surfaces and attributed this result to the partial exclusion of polyelectrolyte molecules from the channel during adsorption. We also investigated the effect of the deposition solutions' ionic strength on confined multilayer growth. We then discussed the systematic narrowing of nanochannels within a hybrid micro/fluidic device and introduced a method by which we monitored the channel thickness using simple conductance measurements. We found that we were able to narrow the gap to just 11 nm before film growth slowed due to physical exclusion.

We extended this work to include the LbL assembly of nanoparticle-containing multilayers. Specifically, deposition of TiO_2 nanoparticles in concert with PVS and of SiO_2 nanoparticles paired with PDAC was performed. Again, uniform and conformal films were created in high aspect ratio nanochannel arrays. Since these films were deposited at low ionic strength however, the effect of surface charge-induced exclusion was greatly magnified, resulting in confined multilayers which were five to six times thinner than the corresponding unconfined film. Additionally, the limiting channel width was much larger; around 50 nm for TiO_2/PVS and over 200 nm for PDAC/SiO_2. We also demonstrated that these films could be calcinated at high temperature, resulting in completely inorganic, nanoporous films.

Having successfully incorporated nanoparticles into a composite multilayer, we next attempted to form confined multilayers using only oppositely charged nanoparticles. Careful control of the deposition pH yielded successful LbL assembly which for thin films yielded similar behavior to what had been observed for the two previous cases. These multilayers conformally and uniformly coated the entire nanochannel and again exhibited decreased film thickness when confined. As the film built up however, differences emerged. When the nanochannel width narrowed to about 500 nm, the channels were systematically bridged by the nanoparticle film. This happened at a similar position near the top of the channel throughout the array. Eventually the channels became completely plugged with a thick nanoporous coating covering the entire substrate. This technique serves both as a method of depositing a thin nanoporous layer within high aspect ratio nanochannels without the need for calcination and as a means of capping the channels with an inorganic nanoporous thin film.

Our consistent observation of surface charge-induced exclusion in confined channels with charged walls led us to attempt to modify TEPC membranes with nanoparticle-containing multilayers in an attempt to form a semipermeable composite membrane which retained its porosity and hence its high water permeance. We measured both the ion and water permeance of these modified films and introduced simple mathematical models to compare with these experimental results. Our data show that ion exclusion effects are not evident in the results meaning that our films do not carry enough charge, the charge is screened by the high electrolyte concentration, or the films have flaws and defects that overwhelm any ion rejection the film might have. When compared to commercial RO membranes, the modified membranes have somewhat higher water permeance, but drastically reduced salt rejection.

In summary, this thesis highlights a number of interesting consequences that arise when LbL assembly is carried out in confined geometries. This work adds to our fundamental understanding of deposition in high aspect ratio pores or channels and points to ways in which we can control the structure of films deposited on these interesting substrates. This work also suggests a number of applications, showing that LbL assembly is a viable method of surface functionalization in nanofluidic devices and other confined surfaces.

7.2 Future Work

In the first part of this thesis we demonstrated systematic narrowing of nanochannels using LbL deposition of PAH and PSS. In future work, it would be interesting to look at the effect of low ionic strengths on deposition. In this work we focused largely on salt concentration of 0.1 M and higher. The problem with going to lower ionic strengths is that growth becomes extremely slow so that the resulting films are difficult to characterize accurately. A faster growing system such as PAH/PSS deposited at pH 9.3 or PAH/PAA deposited at pH 7.5 and pH 3.5 respectively may allow a greater range of deposition ionic strengths to be investigated. This would give more confidence that the hypothesized exclusion mechanism is correct. Additionally, a more systematic study of the effect of the initial channel thickness would also shed light on this phenomenon.

This work also points towards applications beyond simple narrowing of the channels. The conductance-based measuring of the channel thickness would be very useful for monitoring the behavior of stimuli-responsive films *i.e.* films which swell in response to changes in pH, temperature, or even electrical current. Additionally, the modification of these channels with specific chemical or biological functionalities using LbL could lead to the ability to carry out reactions and perform analytical techniques within such a device.

Our work on all nanoparticle coatings also suggests interesting future experiments. In particular, the deposition of these multilayers as part of a device may be very useful in terms of providing a very high specific surface area. If the particles could be functionalized after deposition to increase their surface charge or to decorate them with specific functional molecules this high surface area could lead to ion rejection or very efficient reaction and detection. These sorts of nanoporous films may also be interesting as a matrix for on-chip chromatography. The robustness of these multilayers is also an interesting area that could be explored. Calcination or hydrothermal treatments could be employed and optimized to increase the strength of these nanoporous layers and to tune the structure of the film.

Our work on the modification of porous TEPC membranes leaves a number of open questions. Further investigations should focus on determining whether the films fabricated here failed due to defects or due to a lack of sufficient charge within the nanoporous multilayer. The surface charge of these nanoparticles could be modified by attaching charged groups to their surface or by measuring ion permeation at different pH values for which the particles carry different amounts of surface charge. Techniques like hydrothermal treatment could also be attempted and optimized in order to increase the robustness of the nanoporous multilayer and reduce the frequency of defects.

It would also be interesting to determine whether all nanoparticle LbL at the conditions so successfully used in systematically capping the nanochannel arrays gives similar results on TEPC membranes. If so, this might be a promising alternative to the PAH/SiO_2 system used in this work. Our results seem to suggest that TiO_2/SiO_2 results in relatively low numbers of defects as is, but strategies to improve adhesion such as precursor polyelectrolyte multilayers should also be looked at if this becomes a problem. It would also be interesting to look at whether just a few bilayers of polymer deposition on top of the nanoparticle film is enough to seal the defect sites without compromising the high flux inordinately.

References

1. Li, Z.; Lee, D.; Sheng, X.; Cohen, R. E.; Rubner, M. F. Two-Level Antibacterial Coating with Both Release-Killing and Contact-Killing Capabilities. *Langmuir* **2006**, *22*, 9820-9823.
2. Lee, D.; Cohen, R. E.; Rubner, M. F. Antibacterial Properties of Ag Nanoparticle Loaded Multilayers and Formation of Magnetically Directed Antibacterial Microparticles. *Langmuir* **2005**, *21*, 9651-9659.
3. Lichter, J. A.; Rubner, M. F. Polyelectrolyte Multilayers with Intrinsic Antimicrobial Functionality: The Importance of Mobile Polycations. *Langmuir* **2009**, *25*, 7686-7694.
4. Lichter, J. A.; Van Vliet, K. J.; Rubner, M. F. Design of Antibacterial Surfaces and Interfaces: Polyelectrolyte Multilayers as a Multifunctional Platform. *Macromolecules* **2009**, *42*, 8573-8586.
5. Mendelsohn, J. D.; Yang, S. Y.; Hiller, J. A.; Hochbaum, A. I.; Rubner, M. F. Rational Design of Cytophilic and Cytophobic Polyelectrolyte Multilayer Thin Films. *Biomacromolecules* **2003**, *4*, 96-106.
6. Thompson, M. T.; Berg, M. C.; Tobias, I. S.; Rubner, M. F.; Van Vliet, K. J. Tuning compliance of nanoscale polyelectrolyte multilayers to modulate cell adhesion. *Biomaterials* **2005**, *26*, 6836-6845.
7. Swiston, A. J.; Cheng, C.; Um, S. H.; Irvine, D. J.; Cohen, R. E.; Rubner, M. F. Surface Functionalization of Living Cells with Multilayer Patches. *Nano Lett.* **2008**, *8*, 4446-4453.
8. Zhai, L.; Cebeci, F. C.; Cohen, R. E.; Rubner, M. F. Stable Superhydrophobic Coatings from Polyelectrolyte Multilayers. *Nano Lett.* **2004**, *4*, 1349-1353.
9. Zhai, L.; Berg, M. C.; Cebeci, F. C.; Kim, Y.; Milwid, J. M.; Rubner, M. F.; Cohen, R. E. Patterned Superhydrophobic Surfaces: Toward a Synthetic Mimic of the Namib Desert Beetle. *Nano Lett.* **2006**, *6*, 1213-1217.
10. Bravo, J.; Zhai, L.; Wu, Z.; Cohen, R. E.; Rubner, M. F. Transparent Superhydrophobic Films Based on Silica Nanoparticles. *Langmuir* **2007**, *23*, 7293-7298.
11. Tuteja, A.; Choi, W.; Ma, M.; Mabry, J. M.; Mazzella, S. A.; Rutledge, G. C.; McKinley, G. H.; Cohen, R. E. Designing Superoleophobic Surfaces. *Science* **2007**, *318*, 1618-1622.
12. Tuteja, A.; Choi, W.; Mabry, J. M.; McKinley, G. H.; Cohen, R. E. Robust omniphobic surfaces. *Proc. Natl. Acad. Sci. U. S. A.* **2008**, *105*, 18200-18205.
13. Choi, W.; Tuteja, A.; Chhatre, S.; Mabry, J. M.; Cohen, R. E.; McKinley, G. H. Fabrics with Tunable Oleophobicity. *Adv. Mater.* **2009**, *21*, 2190-2195.
14. Chhatre, S. S.; Tuteja, A.; Choi, W.; Revaux, A. l.; Smith, D.; Mabry, J. M.; McKinley, G. H.; Cohen, R. E. Thermal Annealing Treatment to Achieve Switchable and Reversible Oleophobicity on Fabrics. *Langmuir* **2009**, *25*, 13625-13632.
15. Chhatre, S. S.; Choi, W.; Tuteja, A.; Park, K.-C.; Mabry, J. M.; McKinley, G. H.; Cohen, R. E. Scale Dependence of Omniphobic Mesh Surfaces. *Langmuir* **2009**, *26*, 4027-4035.
16. Srinivasan, S.; Chhatre, S. S.; Mabry, J. M.; Cohen, R. E.; McKinley, G. H. Solution spraying of poly(methyl methacrylate) blends to fabricate microtextured, superoleophobic surfaces. *Polymer* **2011**, *52*, 3209-3218.
17. Lee, D.; Rubner, M. F.; Cohen, R. E. All-Nanoparticle Thin-Film Coatings. *Nano Lett.* **2006**, *6*, 2305-2312.

18. Cebeci, F. C.; Wu, Z.; Zhai, L.; Cohen, R. E.; Rubner, M. F. Nanoporosity-Driven Superhydrophilicity: A Means to Create Multifunctional Antifogging Coatings. *Langmuir* **2006**, *22*, 2856-2862.
19. Wu, Z.; Lee, D.; Rubner, Michael F.; Cohen, Robert E. Structural Color in Porous, Superhydrophilic, and Self-Cleaning SiO_2/TiO_2 Bragg Stacks. *Small* **2007**, *3*, 1445-1451.
20. Nuraje, N.; Asmatulu, R.; Cohen, R. E.; Rubner, M. F. Durable Antifog Films from Layer-by-Layer Molecularly Blended Hydrophilic Polysaccharides. *Langmuir* **2011**, *27*, 782-791.
21. Lee, D.; Nolte, A. J.; Kunz, A. L.; Rubner, M. F.; Cohen, R. E. pH-Induced Hysteretic Gating of Track-Etched Polycarbonate Membranes: Swelling/Deswelling Behavior of Polyelectrolyte Multilayers in Confined Geometry. *J. Am. Chem. Soc.* **2006**, *128*, 8521-8529.
22. Zhai, L.; Nolte, A. J.; Cohen, R. E.; Rubner, M. F. pH-Gated Porosity Transitions of Polyelectrolyte Multilayers in Confined Geometries and Their Application as Tunable Bragg Reflectors. *Macromolecules* **2004**, *37*, 6113-6123.
23. Itano, K.; Choi, J.; Rubner, M. F. Mechanism of the pH-Induced Discontinuous Swelling/Deswelling Transitions of Poly(allylamine hydrochloride)-Containing Polyelectrolyte Multilayer Films. *Macromolecules* **2005**, *38*, 3450-3460.
24. Chia, K.-K.; Rubner, M. F.; Cohen, R. E. pH-Responsive Reversibly Swellable Nanotube Arrays. *Langmuir* **2009**, *25*, 14044-14052.
25. Tan, W. S.; Cohen, R. E.; Rubner, M. F.; Sukhishvili, S. A. Temperature-Induced, Reversible Swelling Transitions in Multilayers of a Cationic Triblock Copolymer and a Polyacid. *Macromolecules* **2010**, *43*, 1950-1957.
26. Lee, D.; Cohen, R. E.; Rubner, M. F. Heterostructured Magnetic Nanotubes. *Langmuir* **2007**, *23*, 123-129.
27. Kurt, P.; Banerjee, D.; Cohen, R. E.; Rubner, M. F. Structural color via layer-by-layer deposition: layered nanoparticle arrays with near-UV and visible reflectivity bands. *J. Mater. Chem.* **2009**, *19*, 8920-8927.
28. Nogueira, G. M.; Banerjee, D.; Cohen, R. E.; Rubner, M. F. Spray-Layer-by-Layer Assembly Can More Rapidly Produce Optical-Quality Multistack Heterostructures. *Langmuir* **2011**, *27*, 7860-7867.
29. Flory, P. J., *Principles of Polymer Chemistry*. Cornell University Press: Ithaca, NY, 1953.
30. Shiratori, S. S.; Rubner, M. F. pH-Dependent Thickness Behavior of Sequentially Adsorbed Layers of Weak Polyelectrolytes. *Macromolecules* **2000**, *33*, 4213-4219.
31. Choi, J.; Rubner, M. F. Influence of the Degree of Ionization on Weak Polyelectrolyte Multilayer Assembly. *Macromolecules* **2004**, *38*, 116-124.
32. Stockton, W. B.; Rubner, M. F. Molecular-Level Processing of Conjugated Polymers. 4. Layer-by-Layer Manipulation of Polyaniline via Hydrogen-Bonding Interactions. *Macromolecules* **1997**, *30*, 2717-2725.
33. Sukhishvili, S. A.; Granick, S. Layered, Erasable, Ultrathin Polymer Films. *J. Am. Chem. Soc.* **2000**, *122*, 9550-9551.
34. Wang, L.; Wang, Z.; Zhang, X.; Shen, J.; Chi, L.; Fuchs, H. A new approach for the fabrication of an alternating multilayer film of poly(4-vinylpyridine) and poly(acrylic acid) based on hydrogen bonding. *Macromol. Rapid Commun.* **1997**, *18*, 509-514.
35. Bourdillon, C.; Demaille, C.; Moiroux, J.; Savéant, J.-M. From Homogeneous Electroenzymatic Kinetics to Antigen-Antibody Construction and Characterization of

Spatially Ordered Catalytic Enzyme Assemblies on Electrodes. *Acc. Chem. Res.* **1996**, *29*, 529-535.

36. Hoshi, T.; Anzai, J.-i.; Osa, T. Controlled Deposition of Glucose Oxidase on Platinum Electrode Based on an Avidin/Biotin System for the Regulation of Output Current of Glucose Sensors. *Anal. Chem.* **1995**, *67*, 770-774.
37. Decher, G. Fuzzy Nanoassemblies: Toward Layered Polymeric Multicomposites. *Science* **1997**, *277*, 1232-1237.
38. Schmitt, J.; Grünewald, T.; Decher, G.; Pershan, P. S.; Kjaer, K.; Lösche, M. Internal structure of layer-by-layer adsorbed polyelectrolyte films: a neutron and x-ray reflectivity study. *Macromolecules* **1993**, *26*, 7058-7063.
39. Lösche, M.; Schmitt, J.; Decher, G.; Bouwman, W. G.; Kjaer, K. Detailed Structure of Molecularly Thin Polyelectrolyte Multilayer Films on Solid Substrates as Revealed by Neutron Reflectometry. *Macromolecules* **1998**, *31*, 8893-8906.
40. Caruso, F.; Lichtenfeld, H.; Giersig, M.; Mohwald, H. Electrostatic Self-Assembly of Silica Nanoparticle-Polyelectrolyte Multilayers on Polystyrene Latex Particles. *J. Am. Chem. Soc.* **1998**, *120*, 8523-8524.
41. Wang, Y.; Angelatos, A. S.; Dunstan, D. E.; Caruso, F. Infiltration of Macromolecules into Nanoporous Silica Particles. *Macromolecules* **2007**, *40*, 7594-7600.
42. Wang, Y.; Caruso, F. Template Synthesis of Stimuli-Responsive Nanoporous Polymer-Based Spheres via Sequential Assembly. *Chem. Mater.* **2006**, *18*, 4089-4100.
43. Arsenault, A. C.; Halfyard, J.; Wang, Z.; Kitaev, V.; Ozin, G. A.; Manners, I.; Mihi, A.; Miguez, H. Tailoring Photonic Crystals with Nanometer-Scale Precision Using Polyelectrolyte Multilayers. *Langmuir* **2005**, *21*, 499-503.
44. Lavalle, P.; Gergely, C.; Cuisinier, F. J. G.; Decher, G.; Schaaf, P.; Voegel, J. C.; Picart, C. Comparison of the Structure of Polyelectrolyte Multilayer Films Exhibiting a Linear and an Exponential Growth Regime: An in Situ Atomic Force Microscopy Study. *Macromolecules* **2002**, *35*, 4458-4465.
45. Iler, R. K. Multilayers of colloidal particles. *J. Colloid Interface Sci.* **1966**, *21*, 569-594.
46. Wu, Z.; Walish, J.; Nolte, A.; Zhai, L.; Cohen, R. E.; Rubner, M. F. Deformable Antireflection Coatings from Polymer and Nanoparticle Multilayers. *Adv. Mater.* **2006**, *18*, 2699-2702.
47. Du, Y.; Luna, L. E.; Tan, W. S.; Rubner, M. F.; Cohen, R. E. Hollow Silica Nanoparticles in UV-Visible Antireflection Coatings for Poly(methyl methacrylate) Substrates. *ACS Nano* **2010**, *4*, 4308-4316.
48. Lee, D.; Omolade, D.; Cohen, R. E.; Rubner, M. F. pH-Dependent Structure and Properties of TiO_2/SiO_2 Nanoparticle Multilayer Thin Films. *Chem. Mater.* **2007**, *19*, 1427-1433.
49. Lee, D.; Gemici, Z.; Rubner, M. F.; Cohen, R. E. Multilayers of Oppositely Charged SiO_2 Nanoparticles: Effect of Surface Charge on Multilayer Assembly. *Langmuir* **2007**, *23*, 8833-8837.
50. Srivastava, S.; Kotov, N. A. Composite Layer-by-Layer (LBL) Assembly with Inorganic Nanoparticles and Nanowires. *Acc. Chem. Res.* **2008**, *41*, 1831-1841.
51. Gemici, Z.; Shimomura, H.; Cohen, R. E.; Rubner, M. F. Hydrothermal Treatment of Nanoparticle Thin Films for Enhanced Mechanical Durability. *Langmuir* **2008**, *24*, 2168-2177.

52. Ostrander, J. W.; Mamedov, A. A.; Kotov, N. A. Two Modes of Linear Layer-by-Layer Growth of Nanoparticle-Polylectrolyte Multilayers and Different Interactions in the Layer-by-layer Deposition. *J. Am. Chem. Soc.* **2001**, *123*, 1101-1110.
53. Kotov, N. A.; Dekany, I.; Fendler, J. H. Layer-by-Layer Self-Assembly of Polyelectrolyte-Semiconductor Nanoparticle Composite Films. *J. Phys. Chem.* **1995**, *99*, 13065-13069.
54. Lvov, Y.; Ariga, K.; Onda, M.; Ichinose, I.; Kunitake, T. Alternate Assembly of Ordered Multilayers of SiO_2 and Other Nanoparticles and Polyions. *Langmuir* **1997**, *13*, 6195-6203.
55. Shimomura, H.; Gemici, Z.; Cohen, R. E.; Rubner, M. F. Layer-by-Layer-Assembled High-Performance Broadband Antireflection Coatings. *ACS Appl. Mater. Interfaces* **2010**, *2*, 813-820.
56. Mao, P.; Han, J. Fabrication and characterization of 20 nm planar nanofluidic channels by glass–glass and glass–silicon bonding. *Lab Chip* **2005**, *5*, 837-844.
57. Turner, S. W.; Perez, A. M.; Lopez, A.; Craighead, H. G. Monolithic nanofluid sieving structures for DNA manipulation. *J. Vac. Sci. Technol., B* **1998**, *16*, 3835-3840.
58. Austin, R. H.; Tegenfeldt, J. O.; Cao, H.; Chou, S. Y.; Cox, E. C. Scanning the controls: genomics and nanotechnology. *IEEE Trans. Nanotechnol.* **2002**, *1*, 12-18.
59. Mao, P.; Han, J. Massively-parallel ultra-high-aspect-ratio nanochannels as mesoporous membranes. *Lab Chip* **2009**, *9*, 586-591.
60. Sato, K.; Shikida, M.; Matsushima, Y.; Yamashiro, T.; Asaumi, K.; Iriye, Y.; Yamamoto, M. Characterization of orientation-dependent etching properties of single-crystal silicon: effects of KOH concentration. *Sens. Actuators, A* **1998**, *64*, 87-93.
61. Price, P. B.; Walker, R. M. Chemical Etching of Charged-Particle Tracks in Solids. *J. Appl. Phys.* **1962**, *33*, 3407-3412.
62. Fleischer, R. L.; Price, P. B.; Walker, R. M. Method of Forming Fine Holes of Near Atomic Dimensions. *Rev. Sci. Instrum.* **1963**, *34*, 510-512.
63. Yamazaki, I. M.; Paterson, R.; Geraldo, L. P. A new generation of track etched membranes for microfiltration and ultrafiltration. Part I. Preparation and characterisation. *J. Membr. Sci.* **1996**, *118*, 239-245.
64. Ferain, E.; Legras, R. Track-etched membrane: dynamics of pore formation. *Nucl. Instrum. Methods Phys. Res., Sect. B* **1994**, *84*, 331-336.
65. Furneaux, R. C.; Rigby, W. R.; Davidson, A. P. The formation of controlled-porosity membranes from anodically oxidized aluminium. *Nature* **1989**, *337*, 147-149.
66. Krishnan, R.; Thompson, C. V. Monodomain High-Aspect-Ratio 2D and 3D Ordered Porous Alumina Structures with Independently Controlled Pore Spacing and Diameter. *Adv. Mater.* **2007**, *19*, 988-992.
67. Hiemenz, P. C.; Rajagopalan, R., *Principles of Colloid and Suface Chemistry*. 3rd ed.; Marcel Dekker: New York, 1997.
68. Schoch, R. B.; Han, J.; Renaud, P. Transport phenomena in nanofluidics. *Rev. Mod. Phys.* **2008**, *80*, 839.
69. Böhmer, M. R.; Evers, O. A.; Scheutjens, J. M. H. M. Weak polyelectrolytes between two surfaces: adsorption and stabilization. *Macromolecules* **1990**, *23*, 2288-2301.
70. Decher, G.; Schlenoff, J. B., *Multilayer Thin Films*. Wiley-VCH: Weinheim, 2003.
71. Podsiadlo, P.; Sui, L.; Elkasabi, Y.; Burgardt, P.; Lee, J.; Miryala, A.; Kusumaatmaja, W.; Carman, M. R.; Shtein, M.; Kieffer, J.; Lahann, J.; Kotov, N. A. Layer-by-Layer

Assembled Films of Cellulose Nanowires with Antireflective Properties. *Langmuir* **2007**, *23*, 7901-7906.

72. Hiller, J. A.; Mendelsohn, J. D.; Rubner, M. F. Reversibly erasable nanoporous anti-reflection coatings from polyelectrolyte multilayers. *Nat. Mater.* **2002**, *1*, 59-63.
73. Chua, P.-H.; Neoh, K.-G.; Kang, E.-T.; Wang, W. Surface functionalization of titanium with hyaluronic acid/chitosan polyelectrolyte multilayers and RGD for promoting osteoblast functions and inhibiting bacterial adhesion. *Biomaterials* **2008**, *29*, 1412-1421.
74. Malcher, M.; Volodkin, D.; Heurtault, B.; André, P.; Schaaf, P.; Möhwald, H.; Voegel, J.-C.; Sokolowski, A.; Ball, V.; Boulmedais, F.; Frisch, B. Embedded Silver Ions-Containing Liposomes in Polyelectrolyte Multilayers: Cargos Films for Antibacterial Agents. *Langmuir* **2008**, *24*, 10209-10215.
75. Boulmedais, F.; Frisch, B.; Etienne, O.; Lavalle, P.; Picart, C.; Ogier, J.; Voegel, J. C.; Schaaf, P.; Egles, C. Polyelectrolyte multilayer films with pegylated polypeptides as a new type of anti-microbial protection for biomaterials. *Biomaterials* **2004**, *25*, 2003-2011.
76. Zhang, L.; Li, Y.; Sun, J.; Shen, J. Mechanically Stable Antireflection and Antifogging Coatings Fabricated by the Layer-by-Layer Deposition Process and Postcalcination. *Langmuir* **2008**, *24*, 10851-10857.
77. Barker, S. L. R.; Ross, D.; Tarlov, M. J.; Gaitan, M.; Locascio, L. E. Control of Flow Direction in Microfluidic Devices with Polyelectrolyte Multilayers. *Anal. Chem.* **2000**, *72*, 5925-5929.
78. Saleh, O. A.; Sohn, L. L. Direct detection of antibody-antigen binding using an on-chip artificial pore. *Proc. Natl. Acad. Sci. U. S. A.* **2003**, *100*, 820-824.
79. Sohn, L. L.; Saleh, O. A.; Facer, G. R.; Beavis, A. J.; Allan, R. S.; Notterman, D. A. Capacitance cytometry: Measuring biological cells one by one. *Proc. Natl. Acad. Sci. U. S. A.* **2000**, *97*, 10687-10690.
80. Fu, J.; Mao, P.; Han, J. Nanofilter array chip for fast gel-free biomolecule separation. *Appl. Phys. Lett.* **2005**, *87*, 263902-3.
81. Fu, J.; Schoch, R. B.; Stevens, A. L.; Tannenbaum, S. R.; Han, J. A patterned anisotropic nanofluidic sieving structure for continuous-flow separation of DNA and proteins. *Nat. Nanotechnol.* **2007**, *2*, 121-128.
82. Fu, J.; Yoo, J.; Han, J. Molecular Sieving in Periodic Free-Energy Landscapes Created by Patterned Nanofilter Arrays. *Phys. Rev. Lett.* **2006**, *97*, 018103.
83. Han, J.; Craighead, H. G. Separation of Long DNA Molecules in a Microfabricated Entropic Trap Array. *Science* **2000**, *288*, 1026-1029.
84. Llopis, S. L.; Osiri, J.; Soper, S. A. Surface modification of poly(methyl methacrylate) microfluidic devices for high-resolution separations of single-stranded DNA. *Electrophoresis* **2007**, *28*, 984-993.
85. Wang, Y. C.; Stevens, A. L.; Han, J. Million-fold Preconcentration of Proteins and Peptides by Nanofluidic Filter. *Anal. Chem.* **2005**, *77*, 4293-4299.
86. Wang, Y.; Angelatos, A. S.; Caruso, F. Template Synthesis of Nanostructured Materials via Layer-by-Layer Assembly. *Chem. Mater.* **2008**, *20*, 848-858.
87. Ai, S.; Lu, G.; He, Q.; Li, J. Highly Flexible Polyelectrolyte Nanotubes. *J. Am. Chem. Soc.* **2003**, *125*, 11140-11141.
88. Hou, S.; Harrell, C. C.; Trofin, L.; Kohli, P.; Martin, C. R. Layer-by-Layer Nanotube Template Synthesis. *J. Am. Chem. Soc.* **2004**, *126*, 5674-5675.

89. Krogman, K. C.; Lowery, J. L.; Zacharia, N. S.; Rutledge, G. C.; Hammond, P. T. Spraying asymmetry into functional membranes layer-by-layer. *Nat. Mater.* **2009**, *8*, 512-518.
90. Sui, Z.; Schlenoff, J. B. Controlling Electroosmotic Flow in Microchannels with pH-Responsive Polyelectrolyte Multilayers. *Langmuir* **2003**, *19*, 7829-7831.
91. Graul, T. W.; Schlenoff, J. B. Capillaries Modified by Polyelectrolyte Multilayers for Electrophoretic Separations. *Anal. Chem.* **1999**, *71*, 4007-4013.
92. Liu, Y.; Xue, Y.; Ji, J.; Chen, X.; Kong, J.; Yang, P.; Girault, H. H.; Liu, B. Gold Nanoparticle Assembly Microfluidic Reactor for Efficient On-line Proteolysis. *Mol. Cell. Proteomics* **2007**, *6*, 1428-1436.
93. Angelatos, A. S.; Wang, Y.; Caruso, F. Probing the Conformation of Polyelectrolytes in Mesoporous Silica Spheres. *Langmuir* **2008**, *24*, 4224-4230.
94. Barker, S. L. R.; Tarlov, M. J.; Canavan, H.; Hickman, J. J.; Locascio, L. E. Plastic Microfluidic Devices Modified with Polyelectrolyte Multilayers. *Anal. Chem.* **2000**, *72*, 4899-4903.
95. Alem, H.; Blondeau, F.; Glinel, K.; Demoustier-Champagne, S.; Jonas, A. M. Layer-by-Layer Assembly of Polyelectrolytes in Nanopores. *Macromolecules* **2007**, *40*, 3366-3372.
96. Wang, Y.; Yu, A.; Caruso, F. Nanoporous Polyelectrolyte Spheres Prepared by Sequentially Coating Sacrificial Mesoporous Silica Spheres. *Angew. Chem., Int. Ed.* **2005**, *44*, 2888-2892.
97. Nolte, A. J.; Rubner, M. F.; Cohen, R. E. Determining the Young's Modulus of Polyelectrolyte Multilayer Films via Stress-Induced Mechanical Buckling Instabilities. *Macromolecules* **2005**, *38*, 5367-5370.
98. Stein, D.; Kruithof, M.; Dekker, C. Surface-Charge-Governed Ion Transport in Nanofluidic Channels. *Phys. Rev. Lett.* **2004**, *93*, 035901.
99. Durstock, M. F.; Rubner, M. F. Dielectric Properties of Polyelectrolyte Multilayers. *Langmuir* **2001**, *17*, 7865-7872.
100. Hirose, E.; Iwamoto, Y.; Norisuye, T. Chain Stiffness and Excluded-Volume Effects in Sodium Poly(styrenesulfonate) Solutions at High Ionic Strength. *Macromolecules* **1999**, *32*, 8629-8634.
101. Brandrup, J.; Immergut, E. H., *Polymer Handbook*. 3rd ed.; Wiley: New York, 1989.
102. Borochov, N.; Eisenberg, H. Stiff (DNA) and Flexible (NaPSS) Polyelectrolyte Chain Expansion at Very Low Salt Concentration. *Macromolecules* **2002**, *27*, 1440-1445.
103. Baur, J. W. Ph.D. Thesis, Department of Materials Science and Engineering, MIT, Cambridge, 1997.
104. Cosgrove, T.; Obey, T. M.; Vincent, B. The configuration of sodium poly(styrene sulfonate) at polystyrene/solution interfaces. *J. Colloid Interface Sci.* **1986**, *111*, 409-418.
105. Nolte, A. J.; Takane, N.; Hindman, E.; Gaynor, W.; Rubner, M. F.; Cohen, R. E. Thin Film Thickness Gradients and Spatial Patterning via Salt Etching of Polyelectrolyte Multilayers. *Macromolecules* **2007**, *40*, 5479-5486.
106. Deen, W. M. Hindered transport of large molecules in liquid-filled pores. *AIChE J.* **1987**, *33*, 1409-1425.
107. Hiller, J.; Rubner, M. F. Reversible Molecular Memory and pH-Switchable Swelling Transitions in Polyelectrolyte Multilayers. *Macromolecules* **2003**, *36*, 4078-4083.
108. Dubas, S. T.; Schlenoff, J. B. Swelling and Smoothing of Polyelectrolyte Multilayers by Salt. *Langmuir* **2001**, *17*, 7725-7727.

109. Huh, D.; Mills, K. L.; Zhu, X.; Burns, M. A.; Thouless, M. D.; Takayama, S. Tuneable elastomeric nanochannels for nanofluidic manipulation. *Nat. Mater.* **2007**, *6*, 424-428.
110. Abgrall, P.; Nguyen, N. T. Nanofluidic Devices and Their Applications. *Anal. Chem.* **2008**, *80*, 2326-2341.
111. Makamba, H.; Kim, J. H.; Lim, K.; Park, N.; Hahn, J. H. Surface modification of poly(dimethylsiloxane) microchannels. *Electrophoresis* **2003**, *24*, 3607-3619.
112. Liu, J.; Lee, M. L. Permanent surface modification of polymeric capillary electrophoresis microchips for protein and peptide analysis. *Electrophoresis* **2006**, *27*, 3533-3546.
113. Horvath, J.; Dolník, V. Polymer wall coatings for capillary electrophoresis. *Electrophoresis* **2001**, *22*, 644-655.
114. Baxamusa, S. H.; Gleason, K. K. Thin Polymer Films with High Step Coverage in Microtrenches by Initiated CVD. *Chem. Vap. Deposition* **2008**, *14*, 313-318.
115. Ozaydin-Ince, G.; Gleason, K. K. Tunable Conformality of Polymer Coatings on High Aspect Ratio Features. *Chem. Vap. Deposition* **2010**, *16*, 100-105.
116. Esker, A. R.; Mengel, C.; Wegner, G. Ultrathin Films of a Polyelectrolyte with Layered Architecture. *Science* **1998**, *280*, 892-895.
117. Caruso, F.; Caruso, R. A.; Möhwald, H. Nanoengineering of Inorganic and Hybrid Hollow Spheres by Colloidal Templating. *Science* **1998**, *282*, 1111-1114.
118. DeRocher, J. P.; Mao, P.; Han, J.; Rubner, M. F.; Cohen, R. E. Layer-by-Layer Assembly of Polyelectrolytes in Nanofluidic Devices. *Macromolecules* **2010**, *43*, 2430-2437.
119. Ali, M.; Yameen, B.; Cervera, J.; Ramírez, P.; Neumann, R.; Ensinger, W.; Knoll, W.; Azzaroni, O. Layer-by-Layer Assembly of Polyelectrolytes into Ionic Current Rectifying Solid-State Nanopores: Insights from Theory and Experiment. *J. Am. Chem. Soc.* **2010**, *132*, 8338-8348.
120. Choi, W.; Termin, A.; Hoffmann, M. R. The Role of Metal Ion Dopants in Quantum-Sized TiO_2: Correlation between Photoreactivity and Charge Carrier Recombination Dynamics. *J. Phys. Chem.* **1994**, *98*, 13669-13679.
121. Lazzara, T. D.; Lau, K. H. A.; Abou-Kandil, A. I.; Caminade, A.-M.; Majoral, J.-P.; Knoll, W. Polyelectrolyte Layer-by-Layer Deposition in Cylindrical Nanopores. *ACS Nano* **2010**, *4*, 3909-3920.
122. Roy, C. J.; Dupont-Gillain, C.; Demoustier-Champagne, S.; Jonas, A. M.; Landoulsi, J. Growth Mechanism of Confined Polyelectrolyte Multilayers in Nanoporous Templates. *Langmuir* **2009**, *26*, 3350-3355.
123. Kim, J. Y.; DeRocher, J. P.; Mao, P.; Han, J.; Cohen, R. E.; Rubner, M. F. Formation of Nanoparticle-Containing Multilayers in Nanochannels via Layer-by-Layer Assembly. *Chem. Mater.* **2010**, *22*, 6409-6415.
124. Carrillo, J.-M. Y.; Dobrynin, A. V. Layer-by-Layer Assembly of Charged Nanoparticles on Porous Substrates: Molecular Dynamics Simulations. *ACS Nano* **2011**, *5*, 3010-3019.
125. Fritzmann, C.; Löwenberg, J.; Wintgens, T.; Melin, T. State-of-the-art of reverse osmosis desalination. *Desalination* **2007**, *216*, 1-76.
126. Adusumilli, M.; Bruening, M. L. Variation of Ion-Exchange Capacity, ζ Potential, and Ion-Transport Selectivities with the Number of Layers in a Multilayer Polyelectrolyte Film. *Langmuir* **2009**, *25*, 7478-7485.
127. Ouyang, L.; Malaisamy, R.; Bruening, M. L. Multilayer polyelectrolyte films as nanofiltration membranes for separating monovalent and divalent cations. *J. Membr. Sci.* **2008**, *310*, 76-84.

128. Hong, S. U.; Malaisamy, R.; Bruening, M. L. Separation of Fluoride from Other Monovalent Anions Using Multilayer Polyelectrolyte Nanofiltration Membranes. *Langmuir* **2007**, *23*, 1716-1722.
129. Harris, J. J.; Stair, J. L.; Bruening, M. L. Layered Polyelectrolyte Films as Selective, Ultrathin Barriers for Anion Transport. *Chem. Mater.* **2000**, *12*, 1941-1946.
130. Jin, W.; Toutianoush, A.; Tieke, B. Use of Polyelectrolyte Layer-by-Layer Assemblies as Nanofiltration and Reverse Osmosis Membranes. *Langmuir* **2003**, *19*, 2550-2553.
131. Park, J.; Park, J.; Kim, S. H.; Cho, J.; Bang, J. Desalination membranes from pH-controlled and thermally-crosslinked layer-by-layer assembled multilayers. *J. Mater. Chem.* **2010**, *20*, 2085-2091.
132. Lajimi, R. H.; Ferjani, E.; Roudesli, M. S.; Deratani, A. Effect of LbL surface modification on characteristics and performances of cellulose acetate nanofiltration membranes. *Desalination* **2011**, *266*, 78-86.
133. Sarkar, A.; Carver, P. I.; Zhang, T.; Merrington, A.; Bruza, K. J.; Rousseau, J. L.; Keinath, S. E.; Dvornic, P. R. Dendrimer-based coatings for surface modification of polyamide reverse osmosis membranes. *J. Membr. Sci.* **2010**, *349*, 421-428.
134. DeRocher, J. P.; Gettelfinger, B. T.; Wang, J.; Nuxoll, E. E.; Cussler, E. L. Barrier membranes with different sizes of aligned flakes. *J. Membr. Sci.* **2005**, *254*, 21-30.

Nomenclature

A	area (m^2)
b	number of bilayers (dimensionless)
b^*	number of bilayers normalized by the number of bilayers required to fill the channel (dimensionless)
c	concentration (M)
C_∞	characteristic ratio (dimensionless)
d	pore diameter (m)
d_p	particle diameter (m)
D	diffusion coefficient (m^2/s)
e	elementary charge (C)
f	gap thickness (m)
F	Faraday constant (C/mol)
H	partition coefficient (dimensionless)
H_n	height of a nanochannel (m)
j	diffusive flux ($mol/m^2/s$)
k	film thickness (m)
k^*	film thickness normalized by half the channel width (dimensionless)
l	length of a bond in a polymer backbone (m)
ℓ	film thickness (m)
L_n	length of a nanochannel (m)
m	slope of multilayer growth curve *i.e.* bilayer thickness (m) or slope of salt breakthrough curve (M/s)
M_w	weight average molecular weight (g/mol)
n_b	number of bonds in a polymer chain (dimensionless)
n_p	number of pores (dimensionless)
N	number of channels in an array (dimensionless)
p	pressure (Pa)

P	ion permeance (m/s) or water permeance *i.e.* $v/\Delta p$ (m^2s/g)
Q	volumetric flow rate (L/s)
$\overline{r}^2$	mean square end-to-end distance (m^2)
R	gas constant (J/mol/K)
R_i	resistance of channel i (Ω)
S	electrical conductance (S)
t	time (s)
T	temperature (K)
v	superficial velocity (m/s)
V	volume (L)
W_n	width of a nanochannel (m)
W_0	width of an uncoated nanochannel (m)
x	generic spatial dimension (m)
z	integer indicating the valence of an ionic species (dimensionless)

α	coil expansion factor (dimensionless)
ε	void fraction (dimensionless)
ε_0	permittivity of free space (F/m)
ε_r	relative permittivity *i.e.* dielectric constant (dimensionless)
θ	bond angle (degrees)
λ_D	Debye length (m)
μ	viscosity (kg/m/s)
μ_i	electrical mobility of species i ($m^2/V/s$)
ρ	electrical resistivity ($\Omega \cdot m$)
σ	surface charge density (C/m^2)
ϕ	volume fraction (dimensionless)

Abbreviations

AAO	Anodized aluminum oxide
CVD	Chemical vapor deposition
DC	Direct current
DI	Deionized
DRIE	Deep reactive ion etching
FTIR	Fourier transform infrared
LbL	Layer-by-layer
LPCVD	Low pressure chemical vapor deposition
PAA	Poly(acrylic acid)
PAH	Poly(allylamine hydrochloride)
PDAC	Poly(diallyldimethylammonium chloride)
PDMS	Poly(dimethylsiloxane)
PECVD	Plasma enhanced chemical vapor deposition
PEM	Polyelectrolyte multilayer
PSS	Poly(styrenesulfonate)
PVS	Poly(vinyl sulfone)
RMS	Root mean square
RO	Reverse osmosis
rpm	Revolutions per minute
SEM	Scanning electron microscopy
TEPC	Track etched polycarbonate

Appendix A MATLAB Script for Analyzing Profilometry Data

```
function profileanalysis(filename, xscale, noise, threshold)

% filename:     the filename of the data file i.e. xxx.txt
% xscale:       the scan length in microns
% noise:        noise tolerance for both baseline and step data in nm
% threshold:    binning threshold i.e. all baseline data should be above it
%               and all step data should be below it

% open filename specified and read data
fid = fopen(filename, 'r');

% this is the number of data points
lengthcell = textscan(fid, '%s %d', 1, 'headerlines', 3);
length = cell2mat(lengthcell(2));

% this is the raw data
datacell = textscan(fid, '%d %f %f %f %f %f', length, 'headerlines', 3);

% close data file
fclose(fid);

% convert data to matrix and convert units to nm from A
data = cell2mat(datacell(2:6));
data = data/10;

% scale x axis according to input scan length
x = linspace(0, xscale, length);

% initialize baseline and step bins
baselinevec = NaN*ones(length,1);
stepvec = NaN*ones(length,1);

% bin data depending on if it's above or below the threshold value
for i = 1:length
    if data(i,3) > threshold
        baselinevec(i,1) = data(i,3);
    else
        stepvec(i,1) = data(i,3);
    end %if
end %for

% calculate averages by removing all NaN and computing the mean
baselinedata = baselinevec;
baselinedata(isnan(baselinedata)) = [];
baseline = mean(baselinedata);

stepdata = stepvec;
stepdata(isnan(stepdata)) = [];
step = mean(stepdata);
```

```
% iterate until baseline data is within tolerance
baselinevectemp = baselinevec;
while max(abs(baselinevectemp - baseline)) > noise
% if criteria is not met, go back to original binned vector
    baselinevectemp = baselinevec;
    for i = 1:length
        if abs(baselinevec(i) - baseline) > noise
            baselinevectemp(i) = NaN;
        end %if
    end %for

% recalculate average after outliers have been eliminated
    baselinedata = baselinevectemp;
    baselinedata(isnan(baselinedata)) = [];
    baseline = mean(baselinedata);

end %while

% iterate until step data is within tolerance
stepvectemp = stepvec;
while max(abs(stepvectemp-step)) > noise
% if criteria is not met, go back to original binned vector
    stepvectemp = stepvec;
    for i = 1:length
        if abs(stepvec(i)-step) > noise
            stepvectemp(i) = NaN;
        end %if
    end %for

% recalculate average after outliers have been eliminated
    stepdata = stepvectemp;
    stepdata(isnan(stepdata)) = [];
    step = mean(stepdata);

end %while

% plot resulting data
% blue is raw data
% red is baseline data used to calculate average (dotted line)
% green is step data used to calculate average (dotted line)
% dotted black line is threshold used for binning

figure(1)
plot(x,data(:,3),'-b', x,baselinevectemp,'-r', x,baseline*ones(length,1),'--
r', x,stepvectemp,'-g', x,step*ones(length,1),'--g',
x,threshold*ones(length,1),'--k')
xlabel('Scan Length (\mum)')
ylabel('Height (nm)')
legend('Raw','Baseline','Baseline Fit','Step','Step
Fit','Threshold','Location','SouthEast')

% calculate trench depth
disp(['The depth is ' num2str(abs(step-baseline)) ' nm.'])

end %function
```

Example Run:

```
>> profileanalysis('26bi-2.txt', 342, 5, -20)

The depth is 51.7146 nm.
```

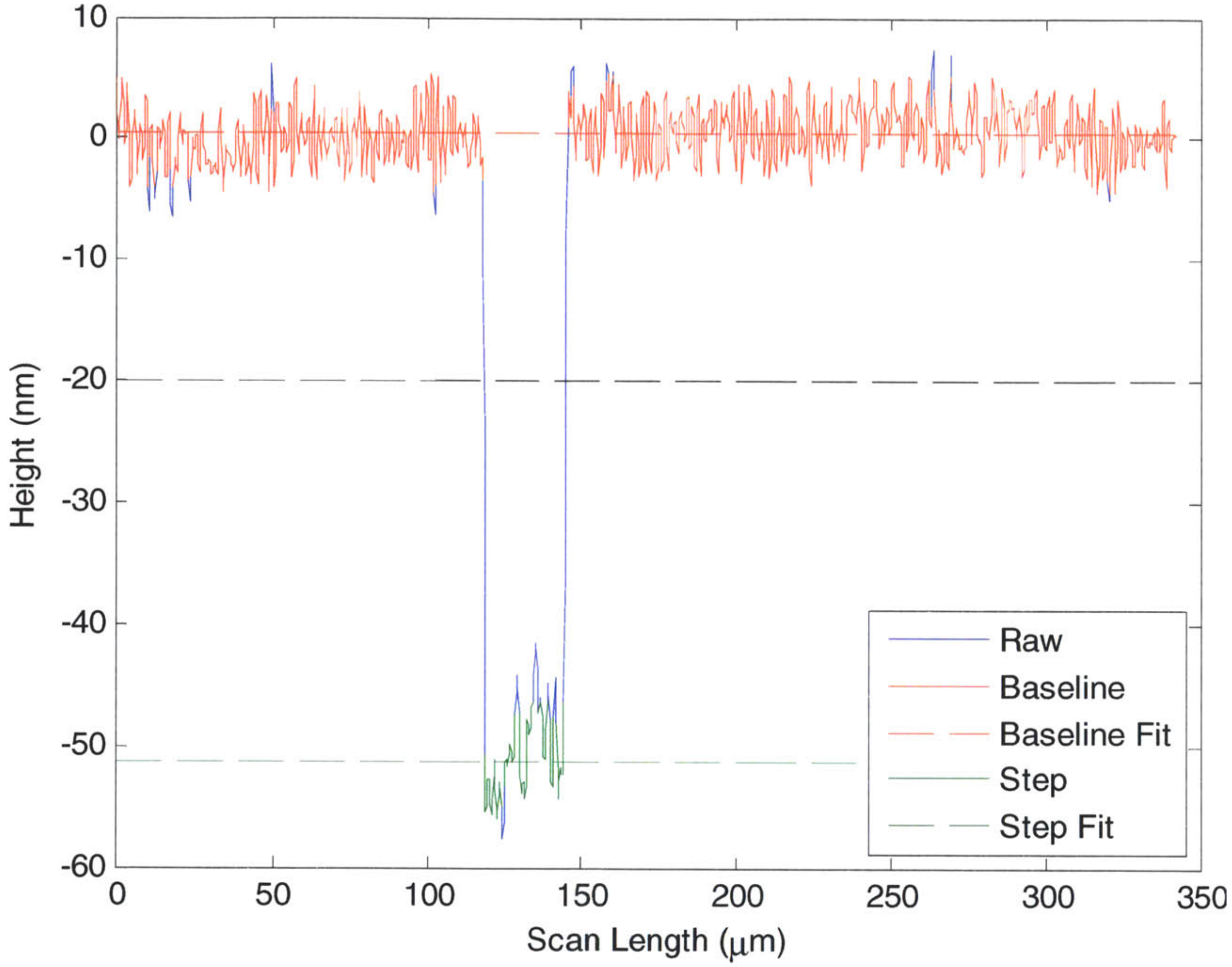

Figure A-1 Example of output provided by profilometry data analysis MATLAB script. The blue line represents the complete data set, the red points are those that are counted in the average used to establish the baseline (dashed red line) and the green points are those that are used to determine the height of the step (dashed green line). The dashed black line represents the threshold provided as input to differentiate between the baseline and step data.

Appendix B Plans for Diaphragm Cell

The diaphragm cell was designed in conjunction with the MIT Central Machine Shop and constructed by them. The body of the apparatus was made from Delrin®. A cutaway side view is provided in Figure B-1. The diaphragm cell was designed in a modular way so that membranes of different sizes could be accommodated. Each cell consists of a cylindrical chamber 3 cm in diameter. A small retaining ring is fixed within the chamber using a set screw in order to keep the stir bar in place. The small opening in the top is for adding solution to the cell and accommodates the conductivity probe. The large opening is threaded so that the piece which interfaces with the membrane can be changed. The one shown below was designed for 25 mm membranes and therefore has a bore of 15 mm. The adjoining piece of the other cell is also shown to highlight the mechanism by which the two cells are sealed together. One side has a collar which is threaded on the inside and can be tightened around the threaded piece on the other side to ensure a tight seal. The membrane is sandwiched between rubber gaskets. Holes are drilled in both end pieces which allow them to be removed easily by inserting a small metal rod.

Figure B-2 is a front/back cutaway view of the diaphragm cell depicting the piece which holds the electrode bolted to the top of the cell. The 13 mm bore through which the electrode passes as well as the chamber itself are shown. Figure B-3 is a top view of the diaphragm cell. The top piece and its bolts are shown as well as the underlying body of the cell to the left and right of the top piece. Additionally, the interfacing piece is depicted with a threaded end which screws into the collar of the other interfacing piece, fastening them together. The small hole drilled into the interfacing piece allows this piece to be unscrewed from the body of the diaphragm cell.

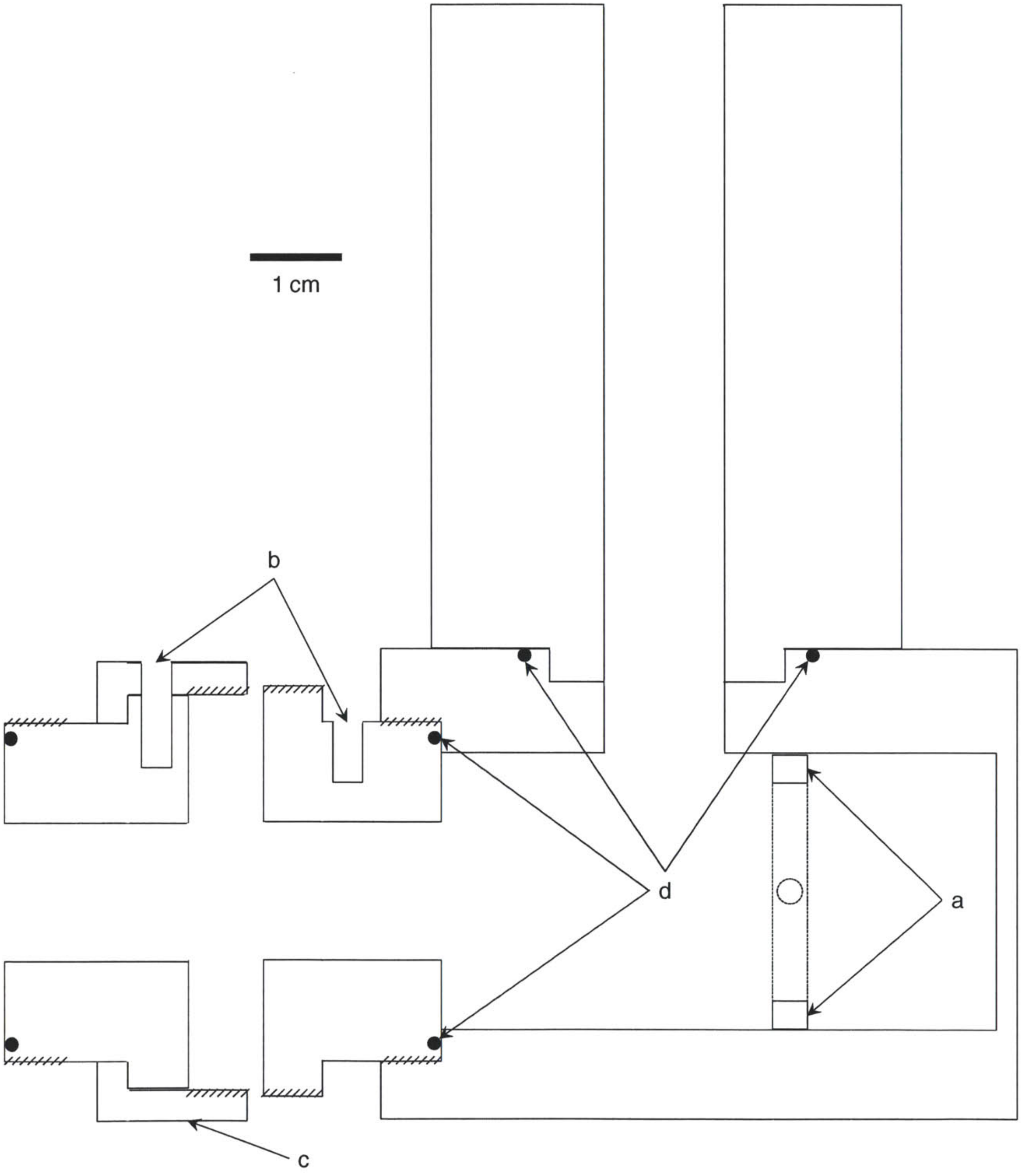

Figure B-1 Cutaway side view of one diaphragm cell and the interfacing piece of the second cell. a) stir bar retaining ring, b) holes to allow insertion of tool to remove end pieces, c) threaded collar to clamp the two cells together, d) o-rings.

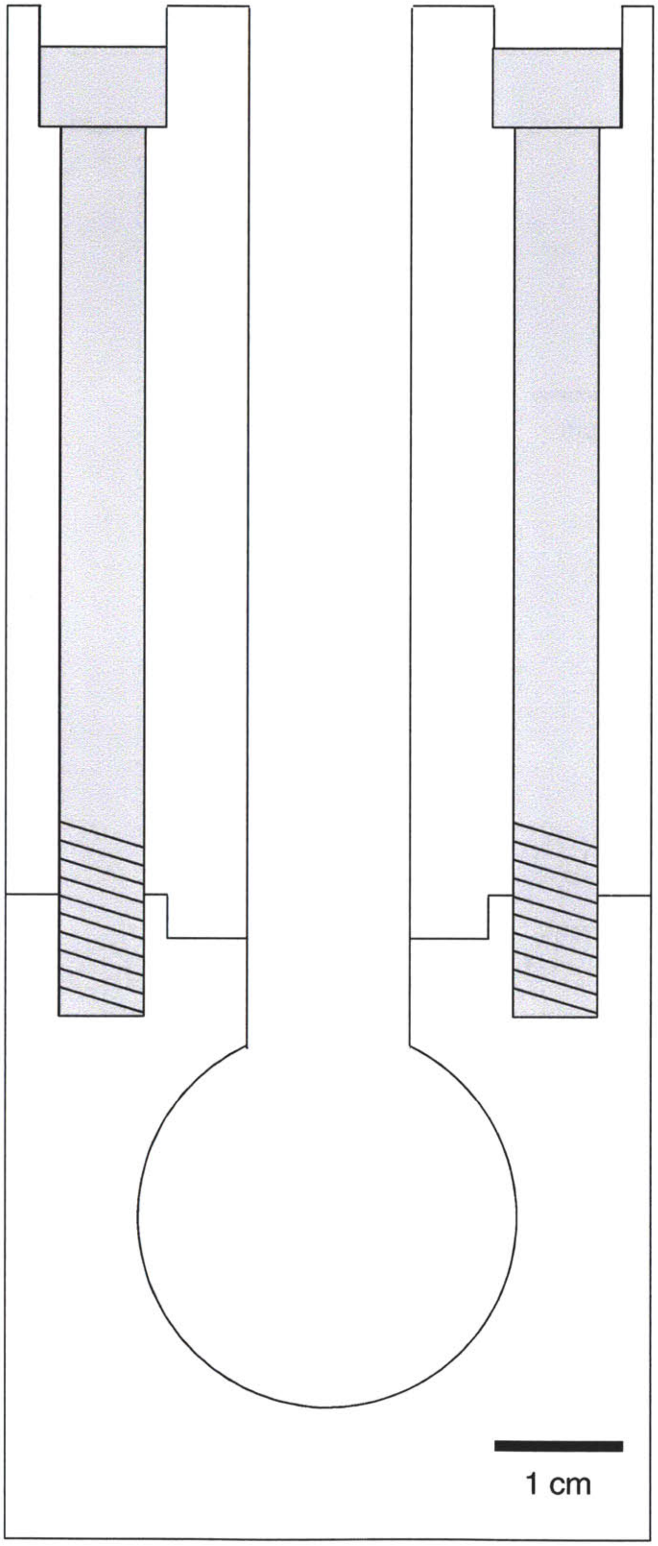

Figure B-2 Front/back cutaway view of diaphragm cell showing the bolts used to attach the top piece which supports the conductivity electrode.

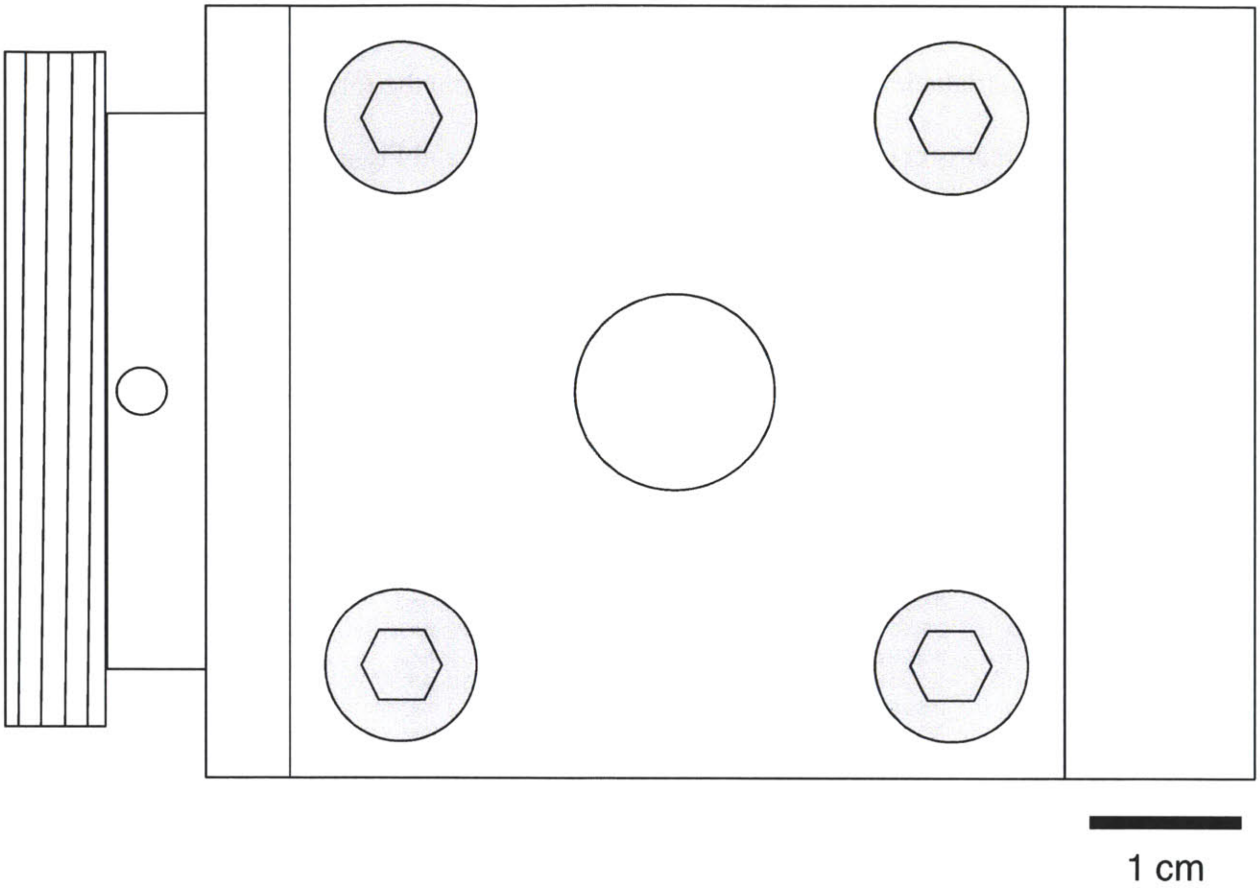

Figure B-3 Top view of diaphragm cell showing the electrode support piece bolted to the top of the diaphragm cell. The threaded interfacing piece which screws into the threaded collar from the other diaphragm cell is shown on the left. The small hole is for insertion of a metal rod which allows the interfacing piece to be removed from the body of the diaphragm cell.

Appendix C Excel Macros for Ion Permeance Data Analysis

The first macro (datacleanup) simply converts the data from the format which is output by the meter into one that is convenient for analysis. Figure C-1 and Figure C-2 show examples of raw data ("Sheet1") and formatted data ("Sheet2") for a particular run. The code for this macro is also given below. The conductance data were then converted to values of the NaCl concentration using a calibration curve (Figure C-3).

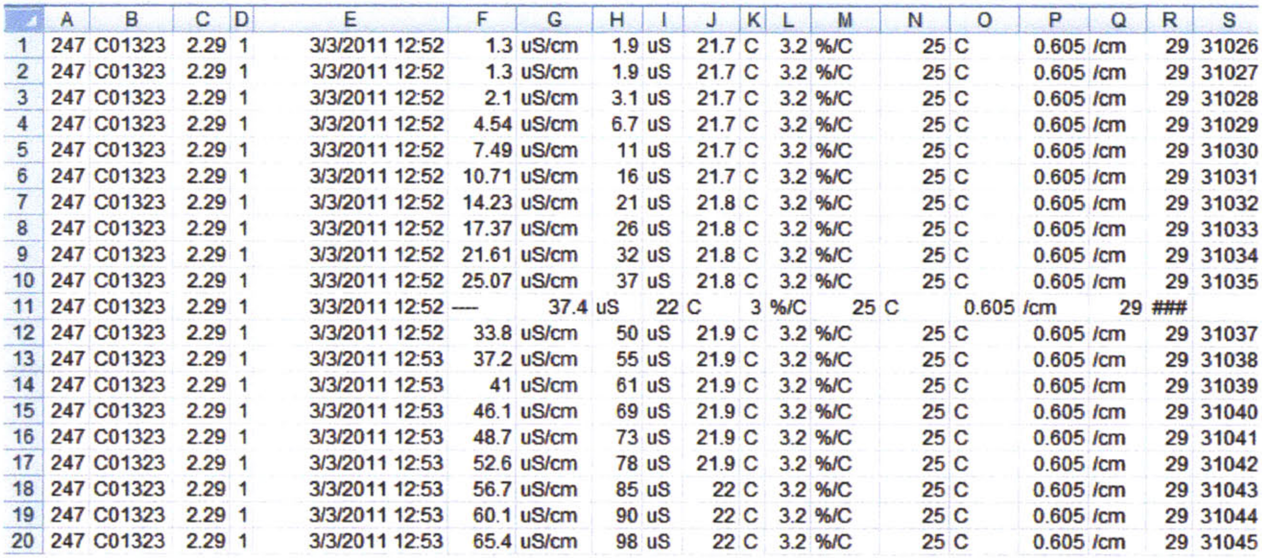

	A	B	C	D	E	F	G	H	I	J	K	L	M	N	O	P	Q	R	S
1	247	C01323	2.29	1	3/3/2011 12:52	1.3	uS/cm	1.9	uS	21.7	C	3.2	%/C	25	C	0.605	/cm	29	31026
2	247	C01323	2.29	1	3/3/2011 12:52	1.3	uS/cm	1.9	uS	21.7	C	3.2	%/C	25	C	0.605	/cm	29	31027
3	247	C01323	2.29	1	3/3/2011 12:52	2.1	uS/cm	3.1	uS	21.7	C	3.2	%/C	25	C	0.605	/cm	29	31028
4	247	C01323	2.29	1	3/3/2011 12:52	4.54	uS/cm	6.7	uS	21.7	C	3.2	%/C	25	C	0.605	/cm	29	31029
5	247	C01323	2.29	1	3/3/2011 12:52	7.49	uS/cm	11	uS	21.7	C	3.2	%/C	25	C	0.605	/cm	29	31030
6	247	C01323	2.29	1	3/3/2011 12:52	10.71	uS/cm	16	uS	21.7	C	3.2	%/C	25	C	0.605	/cm	29	31031
7	247	C01323	2.29	1	3/3/2011 12:52	14.23	uS/cm	21	uS	21.8	C	3.2	%/C	25	C	0.605	/cm	29	31032
8	247	C01323	2.29	1	3/3/2011 12:52	17.37	uS/cm	26	uS	21.8	C	3.2	%/C	25	C	0.605	/cm	29	31033
9	247	C01323	2.29	1	3/3/2011 12:52	21.61	uS/cm	32	uS	21.8	C	3.2	%/C	25	C	0.605	/cm	29	31034
10	247	C01323	2.29	1	3/3/2011 12:52	25.07	uS/cm	37	uS	21.8	C	3.2	%/C	25	C	0.605	/cm	29	31035
11	247	C01323	2.29	1	3/3/2011 12:52	----	37.4	uS	22	C	3	%/C	25	C	0.605	/cm	29	###	
12	247	C01323	2.29	1	3/3/2011 12:52	33.8	uS/cm	50	uS	21.9	C	3.2	%/C	25	C	0.605	/cm	29	31037
13	247	C01323	2.29	1	3/3/2011 12:53	37.2	uS/cm	55	uS	21.9	C	3.2	%/C	25	C	0.605	/cm	29	31038
14	247	C01323	2.29	1	3/3/2011 12:53	41	uS/cm	61	uS	21.9	C	3.2	%/C	25	C	0.605	/cm	29	31039
15	247	C01323	2.29	1	3/3/2011 12:53	46.1	uS/cm	69	uS	21.9	C	3.2	%/C	25	C	0.605	/cm	29	31040
16	247	C01323	2.29	1	3/3/2011 12:53	48.7	uS/cm	73	uS	21.9	C	3.2	%/C	25	C	0.605	/cm	29	31041
17	247	C01323	2.29	1	3/3/2011 12:53	52.6	uS/cm	78	uS	21.9	C	3.2	%/C	25	C	0.605	/cm	29	31042
18	247	C01323	2.29	1	3/3/2011 12:53	56.7	uS/cm	85	uS	22	C	3.2	%/C	25	C	0.605	/cm	29	31043
19	247	C01323	2.29	1	3/3/2011 12:53	60.1	uS/cm	90	uS	22	C	3.2	%/C	25	C	0.605	/cm	29	31044
20	247	C01323	2.29	1	3/3/2011 12:53	65.4	uS/cm	98	uS	22	C	3.2	%/C	25	C	0.605	/cm	29	31045

Figure C-1 Example of raw data transmitted from the conductivity meter and imported into Excel ("Sheet1").

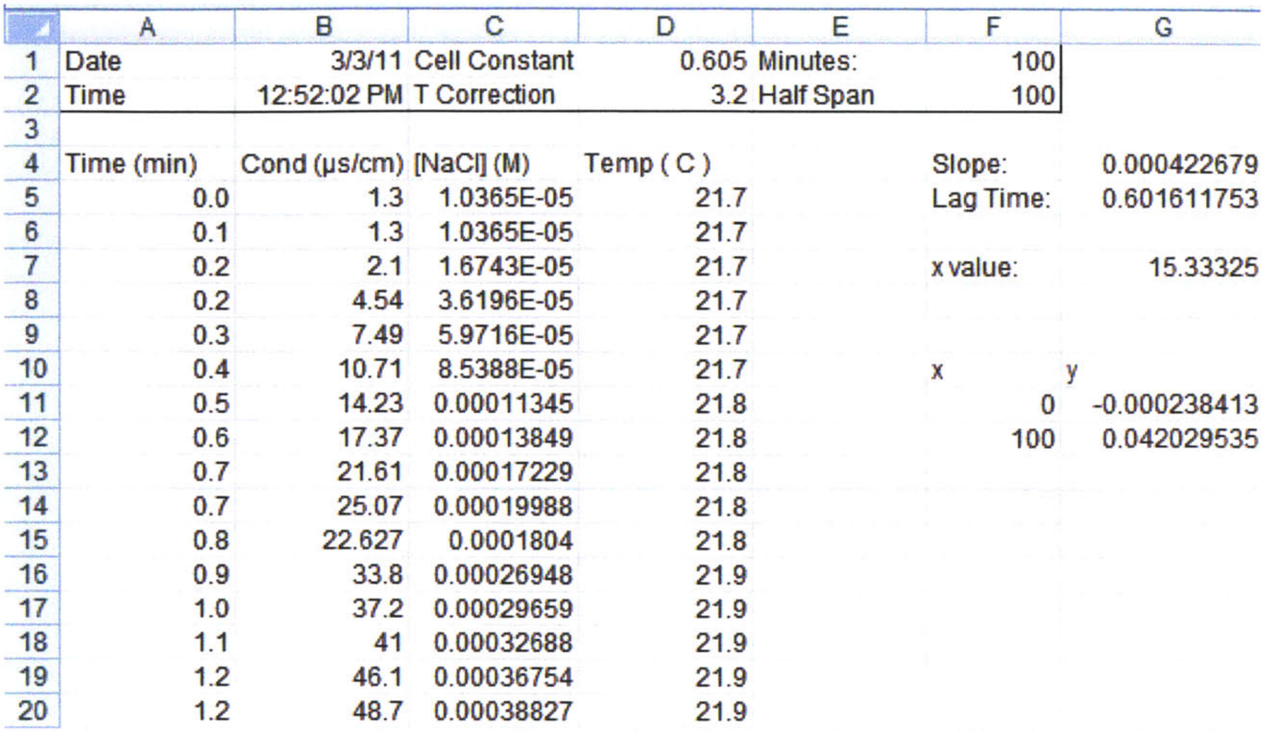

	A	B	C	D	E	F	G
1	Date	3/3/11	Cell Constant	0.605	Minutes:	100	
2	Time	12:52:02 PM	T Correction	3.2	Half Span	100	
3							
4	Time (min)	Cond (µs/cm)	[NaCl] (M)	Temp (C)		Slope:	0.000422679
5	0.0	1.3	1.0365E-05	21.7		Lag Time:	0.601611753
6	0.1	1.3	1.0365E-05	21.7			
7	0.2	2.1	1.6743E-05	21.7		x value:	15.33325
8	0.2	4.54	3.6196E-05	21.7			
9	0.3	7.49	5.9716E-05	21.7			
10	0.4	10.71	8.5388E-05	21.7		x	y
11	0.5	14.23	0.00011345	21.8		0	-0.000238413
12	0.6	17.37	0.00013849	21.8		100	0.042029535
13	0.7	21.61	0.00017229	21.8			
14	0.7	25.07	0.00019988	21.8			
15	0.8	22.627	0.0001804	21.8			
16	0.9	33.8	0.00026948	21.9			
17	1.0	37.2	0.00029659	21.9			
18	1.1	41	0.00032688	21.9			
19	1.2	46.1	0.00036754	21.9			
20	1.2	48.7	0.00038827	21.9			

Figure C-2 Example of the calculation worksheet into which raw data of Figure C-1 was imported ("Sheet2"). The top section is the header and includes two important adjustable parameters: the number of minutes worth of data to import and the span over which to run the best fit slope calculations. The right side contains calculations

```
Sub datacleanup()

Rem copy date, start time, conductivity cell constant, and temperature
correction coefficient to header in Sheet2
Worksheets("Sheet2").Cells(1, 2) = Worksheets("Sheet1").Cells(1, 5) - 0
Worksheets("Sheet2").Cells(2, 2) = Worksheets("Sheet1").Cells(1, 5) - 0
Worksheets("Sheet2").Cells(1, 4) = Worksheets("Sheet1").Cells(1, 16)
Worksheets("Sheet2").Cells(2, 4) = Worksheets("Sheet1").Cells(1, 12)

Rem loop of all data points to be copied (assumes a data point is taken every
5 s)
For x = 0 To 12 * Worksheets("Sheet2").Cells(1, 6)

Rem check for end of data file
If Worksheets("Sheet1").Cells(1 + x, 6) = 0 Then Exit For

Rem check units, if mS/cm multiply by 1000 to convert to uS/cm, if neither
copy -1 to flag bad data
If Worksheets("Sheet1").Cells(1 + x, 7) = "uS/cm" Then
Worksheets("Sheet2").Cells(5 + x, 2) = Worksheets("Sheet1").Cells(1 + x, 6)
Else
If Worksheets("Sheet1").Cells(1 + x, 7) = "mS/cm" Then
Worksheets("Sheet2").Cells(5 + x, 2) = Worksheets("Sheet1").Cells(1 + x, 6) *
1000
Else
Worksheets("Sheet2").Cells(5 + x, 2) = -1
End If
```

```
End If

Rem copy temperature and time since start to Sheet 2
Worksheets("Sheet2").Cells(5 + x, 4) = Worksheets("Sheet1").Cells(1 + x, 10)
Worksheets("Sheet2").Cells(5 + x, 1) = (Worksheets("Sheet1").Cells(1 + x, 5)
- Worksheets("Sheet1").Cells(1, 5)) * 24 * 60

Rem this deals with a quirk of the meter, sometimes it puts out no
conductivity data, but does give a conductance reading. Conductance is
converted to conductivity using the cell constant
If Worksheets("Sheet1").Cells(1 + x, 6) = "----" Then
Worksheets("Sheet2").Cells(5 + x, 4) = Worksheets("Sheet1").Cells(1 + x, 9)
If Worksheets("Sheet1").Cells(1 + x, 8) = "uS" Then
Worksheets("Sheet2").Cells(5 + x, 2) = Worksheets("Sheet1").Cells(1 + x, 7) *
Worksheets("Sheet1").Cells(1 + x, 15)
Else
If Worksheets("Sheet1").Cells(1 + x, 8) = "mS" Then
Worksheets("Sheet2").Cells(5 + x, 2) = Worksheets("Sheet1").Cells(1 + x, 7) *
Worksheets("Sheet1").Cells(1 + x, 15) * 1000
Else
Worksheets("Sheet2").Cells(5 + x, 2) = -1
End If
End If
End If

Next x
End Sub
```

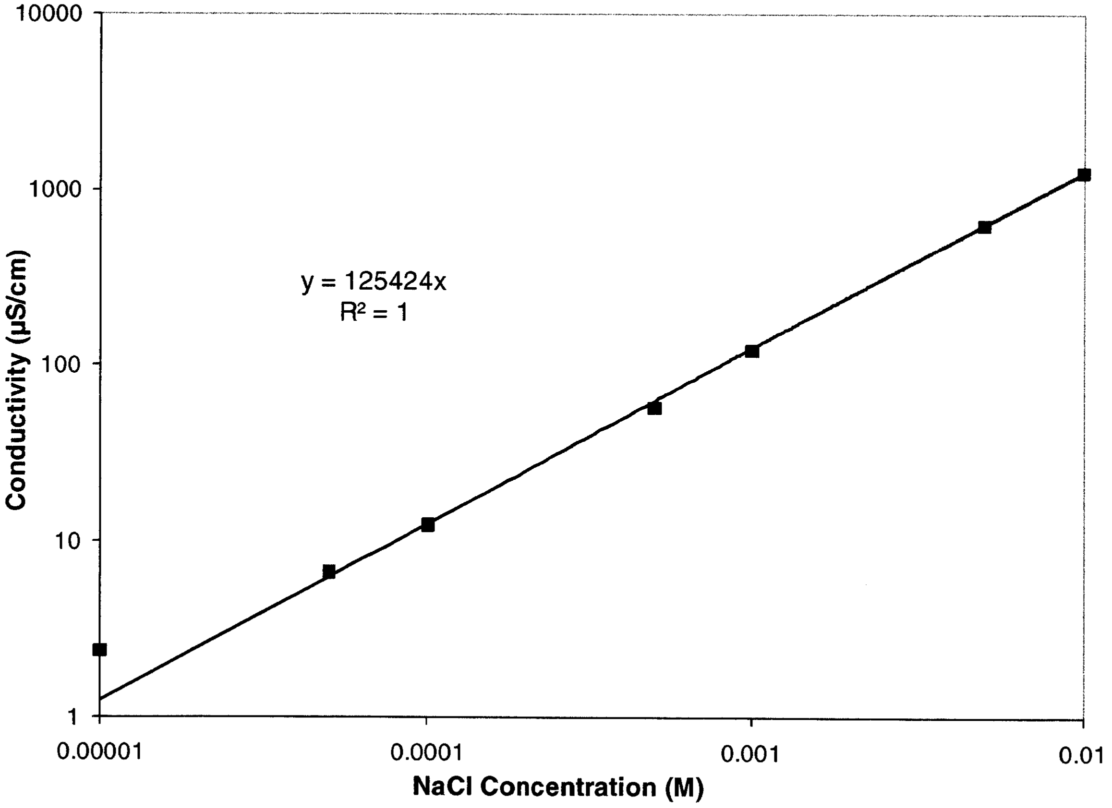

Figure C-3 Calibration curve used to convert electrical conductivity measurements to NaCl concentration.

To determine the ion permeance, the steady-state slope of the breakthrough curve must be measured as described by Equation (6.12) and shown in Figure 6-3. To find the true steady-state slope we recall that one of the assumptions made in deriving Equation (6.12) was that the experiment was short enough that the driving force across the membrane was constant at its initial value. The slope we want to capture therefore is the maximum slope, before the decreasing driving force becomes significant and lowers the slope of the breakthrough curve. Obviously to avoid the effect of noise on this calculation, we need to calculate the slope over a reasonably large number of data points. The macro below (findslope) steps along the curve calculating the slope over a range of data points specified by the user and searches for the highest slope which is then recorded in the worksheet. The slope is calculated via the following formula:

$$m = \frac{N\sum xy - \sum x \sum y}{N\sum x^2 - \left(\sum x\right)^2} \tag{C.1}$$

where m is the slope of the curve, N is the number of data points considered, and x and y are the time and corresponding concentration values in the data set respectively. See the following code for details of the algorithm.

```
Sub findslope()

Dim slope As Double
Dim bestslope As Double
bestslope = 0
Dim intercept As Double
Dim sumxy As Double
Dim sumx As Double
Dim sumy As Double
Dim sumx2 As Double

Rem x is the center of the region over which the linear best fit is taken.
Cells(2,6) is the half span, so we take that number of points either side of
x and run from within a half span of the beginning of the data set to within
a half span of the end of the data set
For x = Cells(2, 6) + 1 To 12 * Cells(1, 6) - Cells(2, 6)
```

```
Rem initialize sums
    sumxy = 0
    sumx = 0
    sumy = 0
    sumx2 = 0

Rem compute sum(x*y), sum(x), sum(y), sum(x^2)
    For i = 0 To 2 * Cells(2, 6)
        sumxy = sumxy + Cells(x + i - Cells(2, 6) + 4, 1) * Cells(x + i -
Cells(2, 6) + 4, 3)
        sumx = sumx + Cells(x + i - Cells(2, 6) + 4, 1)
        sumy = sumy + Cells(x + i - Cells(2, 6) + 4, 3)
        sumx2 = sumx2 + Cells(x + i - Cells(2, 6) + 4, 1) * Cells(x + i -
Cells(2, 6) + 4, 1)
    Next i

Rem check to ensure denominator is not 0, then compute best fit slope
    If sumx2 - sumx * sumx = 0 Then
    slope = 0
    Else
    slope = ((2 * Cells(2, 6) + 1) * sumxy - sumx * sumy) / ((2 * Cells(2, 6)
+ 1) * sumx2 - sumx * sumx)
    End If

Rem if slope is the largest measured keep it, compute the intercept, and
display the time which corresponds to x otherwise keep looking
    If slope > bestslope Then
    bestslope = slope
    intercept = sumy / (2 * Cells(2, 6) + 1) - slope * sumx / (2 * Cells(2,
6) + 1)
    Cells(7, 7) = Cells(x + 5, 1)
    End If

    Cells(4, 7) = bestslope

Next x

Rem compute x intercept (lag time)
Cells(5, 7) = -intercept / bestslope

Rem use slope and intercept to compute two points for display on chart
Cells(11, 7) = Cells(4, 7) * Cells(11, 6) + Cells(Cells(7, 7) * 12 + 5, 3) -
Cells(4, 7) * Cells(7, 7)
Cells(12, 7) = Cells(4, 7) * Cells(12, 6) + Cells(Cells(7, 7) * 12 + 5, 3) -
Cells(4, 7) * Cells(7, 7)
End Sub
```